

### EDITORIAL

Diagnostic errors in radiology:  
where are we? (p. 205-206)

### IN-DEPTH REVIEW

I see double!  
Searching for the abnormal cranial nerve in diplopia (p. 208-220)

### FULL RESEARCH ARTICLES

Mammography breast density assessment with  
Quantra artificial intelligence software:  
intra- and interobserver agreement with radiologists (p. 221-230)

Multimodality imaging of hematologic malignancies affecting the breast:  
a pictorial essay (p. 231-242)

The PROMISE-V2 PRIMARY score and SULmax [<sup>18</sup>F]PSMA-1007 PET/CT  
in primary staging of prostate cancer (p. 243-255)

US duplex findings of deep chronic venous insufficiency of the  
lower limbs in 700 Mexican patients (p. 256-267)

Abnormal Achilles tendon US findings in Mexican patients  
with type 2 diabetes (p. 268-274)

### CASE REPORT

Imaging characterization of pseudomyxoma peritonei:  
a case report (p. 275-279)

### IMAGES IN RADIOLOGY

MR imaging findings  
of neurosarcoidosis (p. 280-281)



PERMANER  
www.permayer.com

Official Journal of the



FEDERACIÓN MEXICANA DE RADIOLOGÍA E IMAGEN, A.C

# A simple step to digital radiography



*i550z*

## Digital Radiography Systems



+52 686-568-1904  
WhatsApp - +520686-606-4076  
www.laicoinfo.com  
Mexicali, BC Mexico

## The Synergy of Innovation and Health Imaging Solutions

Designed to help you see what matters most



**DDR**  
DYNAMIC DIGITAL RADIOGRAPHY

Dynamic Digital Radiology (DDR) enables clinicians to observe the dynamic motion of anatomical structures over time, enhancing diagnostic capabilities. **DDR provides a view of anatomy in motion, with a large field of view and low radiation dose.**

DDR is a promising platform for AI (Artificial Intelligence) applications. DDR is not fluoroscopy;

**DDR is X-ray that Moves!**



xraythatmoves.com

**exa**

Scalable and customizable to the exact requirements of your practice, our leading IT solutions manage medical imaging and patient data right across the healthcare spectrum, including PACS, RIS, specialty viewers and Billing.

Our Healthcare IT software solutions are packed with the all the speed, security and flexibility you need, anytime/anywhere viewing and a single integrated database across all modules.



**KONICA MINOLTA**

contact us: [kmhalatinoamerica@konicaminolta.com](mailto:kmhalatinoamerica@konicaminolta.com)

Learn more about our solutions with Workflow Solutions, Insights and Consulting



Visit <https://radiologia.bayer.com/es> or contact your sales advisor



Clear Direction From Diagnosis to Care

PP-WS-MX-0005-1

# MyLab™ OMEGAeXP

## Advanced Imaging in Motion



**esaote**  
esaote.com

**MedRent**  
medrent.mx

# Carestream

Meet the  
**NEW**  
member  
of the family

## DRX-Rise

It's amazing!



We have **EQUIPMENT** for all **YOUR NEEDS**



Right for **Today...** *Ready for Tomorrow.*



Scan the QR  
and visit  
the Virtual Hospital





## Journal of the Mexican Federation of Radiology and Imaging

*J Mex Fed Radiol Imaging*

Volume 3. Number 4, October-December 2024

ISSN: 2938-1215

eISSN: 2696-8444

The *Journal of the Mexican Federation of Radiology and Imaging* (JMEXFRI) is the official journal of the Federación Mexicana de Radiología e Imagen. The aim of the journal is to disseminate scientific knowledge and technological developments for innovation in diagnostic and therapeutic radiology with original articles on basic and clinical aspects of modern radiology in an international context with global impact. JMEXFRI is published in American English with 4 issues per year (print and online) and the first issue was published in the first quarter of 2022. Articles undergo a rigorous, double-blind peer-review process. Publication of articles in JMEXFRI is free of charge and all published articles are open access.

The journal publishes the following types of manuscripts: *Full Research Article, Pictorial Essay, Brief Research Article, Technical Note, In-Depth Review, Case Report, Images in Radiology, and Editorial.*

### EDITORIAL BOARD

#### EDITOR-IN-CHIEF

**Mauricio Figueroa-Sanchez, M.D.**

*Department of Radiology, Antiguo Hospital Civil de Guadalajara "Fray Antonio Alcalde", Guadalajara, Jal., Mexico*

#### ASSOCIATE EDITORS

**Gerardo E. Ornelas-Cortinas, M.D.**

*Centro Universitario de Imagen Diagnostica, Hospital Universitario "Dr. Jose E. Gonzalez", Monterrey, N.L., Mexico*

**Araceli Cue-Castro, M.D.**

*Department of Computed Tomography, Hospital General "Dr. Enrique Cabrera" SEDESA, Mexico City, Mexico*

**Oscar A. Chavez-Barba, M.D.**

*Department of Radiology, Antiguo Hospital Civil de Guadalajara "Fray Antonio Alcalde", Guadalajara, Jal., Mexico*

**Ana M. Contreras-Navarro, M.D., M.Sc., Ph.D.**

*Scientific Writing Workshop, JMEXFRI, Zapopan, Jal., Mexico*

**David Garza-Cruz, M.D.**

*Department of Radiology, Hospital Angeles, Torreon, Coah., Mexico*

**J. Mario Bernal-Ramirez, M.D.**

*Department of Medical Clinics, Centro Universitario de Ciencias de la Salud, Universidad de Guadalajara, Guadalajara, Jal., Mexico*

#### SCIENTIFIC TRANSLATOR EDITOR

**Sergio Lozano-Rodriguez, M.D.**

*Research Office of the Vice Dean, Hospital Universitario "Dr. Jose E. Gonzalez", Monterrey, N.L., Mexico*

#### BIOSTATISTICS ADVISER

**Cesar N. Cristancho-Rojas, M.D., M.Sc.**

*School of Public Health, Oregon Health & Science University, Portland, OR., USA*

#### DESIGN ADVISER

**Jorge Mendez-Palacios, B.Sc.**

*Design Area, JMEXFRI. Zapopan, Jal., Mexico*

## **NATIONAL EDITORIAL BOARD**

---

### **HEAD AND NECK RADIOLOGY**

Mario A. Campos-Coy, M.D.

*Centro Universitario de Imagen Diagnostica, Hospital Universitario "Dr. Jose E. Gonzalez", Monterrey, N.L., Mexico*

Eduardo D. Sarda-Inman, M.D.

*Diagnostico Especializado por Imagen, Zapopan, Jal., Mexico*

### **GASTROINTESTINAL RADIOLOGY**

Araceli Cue-Castro, M.D.

*Department of Computed Tomography, Hospital General "Dr. Enrique Cabrera" SEDESA, Mexico City, Mexico*

Adrian Negreros-Osuna, M.D., Ph.D.

*Departamento de Radiología, Hospital Regional ISSSTE Monterrey, Monterrey, N.L., Mexico*

Oscar A. Chavez-Barba, M.D.

*Department of Radiology, Antiguo Hospital Civil de Guadalajara "Fray Antonio Alcalde", Guadalajara, Jal., Mexico*

### **OBSTETRIC AND GYNECOLOGIC RADIOLOGY**

Dante R. Casale-Menier, M.D.

*Department of Radiology and Imaging, Hospital Angeles, Ciudad Juarez, Chih., Mexico*

Roberto J. Carrales-Cuellar, M.D.

*Department of Ecographic Diagnosis, Radiología Especializada, Guadalajara, Jal., Mexico*

### **BREAST RADIOLOGY**

David F. Perez-Montemayor, M.D.

*General Direction, Centro de Imagenología Integral IMAX, Tampico, Tamps., Mexico*

Beatriz Gonzalez-Ulloa, M.D.

*Department of Breast Imaging, Diagnostico Especializado por Imagen, Guadalajara, Jal., Mexico*

Margarita L. Garza-Montemayor, M.D.

*Departamento de Imagen Diagnostica, Centro de Cancer de Mama, Hospital Zambrano Hellion, Tec Salud, Monterrey, N.L., Mexico*

Karla M. Nuñez-Barragan, M.D.

*Women's Imaging Department, Doctors Hospital East Auna Monterrey, N. L., Mexico*

### **NUCLEAR AND MOLECULAR MEDICINE**

Hugo E. Solis-Lara, M.D.

*Centro de Imagen Molecular, Hospital Christus Muguerza Alta Especialidad, Monterrey, N.L., Mexico*

### **NEURORADIOLOGY**

Jorge Paz-Gutierrez, M.D.

*Department of Magnetic Resonance, Centro Medico Puerta de Hierro, Zapopan, Jal., Mexico*

Azalea Garza-Baez, M.D.

*Department of Radiology and Imaging, Hospital Zambrano Hellion, Tecnológico de Monterrey, Monterrey, N.L., Mexico*

Perla M. Salgado-Lujambio, M.D.

*Dirección de Enseñanza, Instituto Nacional de Neurología y Neurocirugía "Manuel Velasco Suarez" Mexico City, Mexico*

### **PEDIATRIC RADIOLOGY**

Aida Perez-Lara, M.D.

*Department of Radiology, Hospital Español, Mexico City, Mexico*

### **MUSCULOSKELETAL RADIOLOGY**

Oscar A. Chavez-Barba, M.D.

*Department of Radiology, Antiguo Hospital Civil de Guadalajara "Fray Antonio Alcalde", Guadalajara, Jal., Mexico*

J. Francisco Diaz-Fernandez, M.D.

*Department of Radiology, Hospital General "Agustin O'Horan", Merida, Yuc., Mexico*

### **CHEST AND CARDIOVASCULAR RADIOLOGY**

Sergio A. Criales-Vera, M.D.

*Department of Radiology and Imaging, Instituto Nacional de Cardiología "Ignacio Chavez", Mexico City, Mexico*

Harold Goerne, M.D.

*Department of Radiology, Hospital de Pediatría, Instituto Mexicano del Seguro Social, Guadalajara, Jal., Mexico*

Luis F. Alva-Lopez, M.D.

*Department of Radiology, Hospital Medica Sur, Mexico City, Mexico*

### **GENITOURINARY RADIOLOGY**

Sergio B. Peregrina-Gonzalez, M.D.

*Consultorio de Imagen, Guadalajara, Jal., Mexico*

Araceli Cue-Castro, M.D.

*Department of Computed Tomography, Hospital General "Dr. Enrique Cabrera" SEDESA, Mexico City, Mexico*

Adrian Negreros-Osuna, M.D.

*Departamento de Radiología, Hospital Regional ISSSTE Monterrey, Monterrey, N.L., Mexico*

Benjamin Conde-Castro, M.D.

*Faculty of Medicine, Universidad Nacional Autónoma de Mexico, Mexico City, Mexico*

### **ULTRASOUND**

Rosa M. Alanis-Salazar, M.D.

*Departamento de Radiología, UMF Guadalupe, ISSSTE, Monterrey, NL., Mexico*

Victor M. Rodriguez-Peralta, M.D.

*Department of Radiology, Fundacion de Cancer de Mama (FUCAM), Oaxaca, Oax., Mexico*

David Garza-Cruz, M.D.

*Department of Radiology, Hospital Angeles, Torreon, Coah., Mexico*

Manuel Hernandez-Cruz, M.D.

*Area de Ultrasonido, Unidad de Ultrasonido Diagnostico, Puebla, Pue. Mexico*

### **VASCULAR AND INTERVENTIONAL RADIOLOGY**

Guillermo Elizondo-Riojas, M.D., Ph.D.

*Centro Universitario de Imagen Diagnostica, Hospital Universitario "Dr. Jose E. Gonzalez", Monterrey, N.L., Mexico*

Raul A. De Luna-Vega. M.D.

*Centro Universitario de Imagen Diagnostica, Hospital Universitario "Dr. Jose E. Gonzalez", Monterrey, N.L., Mexico*

### **ARTIFICIAL INTELLIGENCE**

Guillermo Elizondo-Riojas, M.D., Ph.D.

*Centro Universitario de Imagen Diagnostica, Hospital Universitario "Dr. Jose E. Gonzalez", Monterrey, N.L., Mexico*

Adrian Negreros-Osuna, M.D.

*Departamento de Radiología, Hospital Regional ISSSTE Monterrey, Monterrey, N.L., Mexico*

J. Mario Bernal-Ramirez, M.D.

*Department of Medical Clinics, Centro Universitario de Ciencias de la Salud, Universidad de Guadalajara, Guadalajara, Jal., Mexico*

Benjamin Conde-Castro, M.D.

*Faculty of Medicine, Universidad Nacional Autónoma de México, Mexico City, Mexico*

## **JUNIOR EDITORIAL BOARD**

---

J. Mario Bernal-Ramirez, M.D.

*Department of Medical Clinics, Centro Universitario de Ciencias de la Salud, Universidad de Guadalajara, Guadalajara, Jal., Mexico*

Ana K. Luna-Marroquin, M.D.

*Centro Universitario de Imagen Diagnostica, Hospital Universitario "Dr. Jose E. Gonzalez", Monterrey, N.L., Mexico*

M. Lourdes Garcia-Colmenero, M.D.

*Departamento de Radiología, CID Centro de Imagen y Diagnostico Guadalajara, Jal., Mexico*

Xavier A. Gonzalez-Ballesteros, M.D.

*Departamento de Radiología, Hospital San Angel Inn Universidad, Ciudad de Mexico, Mexico*

Adriana Parada-Gallardo, M.D.

*Department of Radiology, Hospital General de Zapopan, Zapopan, Jal., Mexico*

## **INTERNATIONAL EDITORIAL BOARD**

---

### **HEAD AND NECK RADIOLOGY**

Richard H. Wiggins, M.D.

*Department of Radiology and Imaging Sciences, School of Medicine, University of Utah, Salt Lake City, UT., USA*

Amy Juliano, M.D.

*Department of Radiology, Massachusetts Eye and Ear, Harvard Medical School, Boston, MA., USA*

### **GASTROINTESTINAL RADIOLOGY**

Jorge A. Soto, M.D.

*Department of Radiology, Boston Medical Center, Boston, MA., USA*

Jorge Elias Jr. Ph.D.

*Departamento de Imagenes Medicas, Oncologia e Hematologia, Faculdade de Medicina Ribeirao Preto, Universidade Sao Paulo Ribeirao Preto, Sao Paulo, Brazil*

Valdair F. Muglia, M.D.

*Faculdade de Medicina de Ribeirão Preto, Universidade de São Paulo, Ribeirão Preto, Sao Paulo, Brazil*

Carlo Catalano, M.D.

*Department of Diagnostic Radiology La Sapienza University of Rome Rome, Italy*

## OBSTETRIC AND GYNECOLOGIC RADIOLOGY

Luciana Pardini Chamie, M.D., Ph.D.

*Centro de Diagnostico Ultrasonografico  
Especializado en Imagen de la Mujer,  
Sao Paulo, Brazil*

## BREAST RADIOLOGY

Javier Romero-Enciso, M.D.

*Department of Radiology,  
Fundacion Santa Fe,  
Bogota, Colombia*

## NUCLEAR AND MOLECULAR MEDICINE

Begoña Martinez-Sanchis, M.D.

*Department of Nuclear Medicine,  
Hospital Universitario y Politecnico La Fe,  
Valencia, Spain*

Cesar N. Cristancho-Rojas, M.D., M.Sc.

*School of Public Health,  
Oregon Health & Science University,  
Portland, OR., USA*

## NEURORADIOLOGY

Roy F. Riascos-Castaneda, M.D.

*Department of Radiology and Neurosurgery,  
Memorial Hermann Hospital System,  
Houston, TX., USA*

Rafael Rojas-Jasso, M.D.

*Department of Radiology, Beth Israel,  
Deaconess Medical Center,  
Boston, MA., USA*

Henrique Carrete Jr., M.D., Ph.D.

*Department of Diagnostic Imaging,  
Universidade de Sao Paulo,  
Sao Paulo, Brazil*

Carlos Torres, M.D.

*Department of Diagnostic Imaging,  
The Ottawa Hospital,  
Ottawa, Canada*

## MUSCULOSKELETAL RADIOLOGY

Javier Fernandez-Jara, M.D.

*Department of Radiology,  
Hospital Universitario Sanitas La Zarzuela,  
Madrid, Spain*

Jose Luis del Cura, M.D.

*Radiodiagnosis Service,  
Hospital Universitario Donostia,  
San Sebastian-Donostia, Spain*

Diego F. Lemos, M.D.

*Department of Radiology,  
University of Vermont Medical Center,  
Burlington, VT, USA*

## PEDIATRIC RADIOLOGY

George Bisset, M.D.

*Department of Radiology, Children's Hospital  
Pennsylvania, PA., USA*

Sara Reis Teixeira, M.D., Ph.D.

*Department of Radiology, Children's Hospital  
Pennsylvania, PA. USA*

## CHEST AND CARDIOVASCULAR RADIOLOGY

Fernando R. Gutierrez, M.D.

*Department of Radiology and Cardiothoracic Imaging,  
The Mallinckrodt Institute of Radiology,  
St. Louis, MO., USA*

Jorge Carrillo-Bayona, M.D.

*Department of Radiology,  
Hospital Universitario Mayor,  
Bogota, Colombia*

Carlos S. Restrepo, M.D.

*Department of Cardiothoracic Radiology,  
Texas University,  
San Antonio, TX., USA*

Sebastian Rossini, M.D.

*Department of Radiology,  
Instituto Radiologico Mater Dei,  
Buenos Aires, Argentina*

Santiago Martinez-Jimenez, M.D.

*Department of Radiology,  
Saint Luke's Hospital of Kansas City,  
Kansas City, KS., USA*

L. Antonio Sosa-Lozano, M.D.

*Department of Cardiothoracic Radiology,  
Medical College of Wisconsin,  
Milwaukee, WI., USA*

## GENITOURINARY RADIOLOGY

Daniela Stoisa, M.D.

*Department of Radiology, Diagnostico Medico Oroño,  
Rosario, Santa Fe, Argentina*

Valdair F. Muglia, M.D.

*Faculdade de Medicina de Ribeirao Preto,  
Universidade de Sao Paulo Ribeirao Preto,  
Sao Paulo, Brazil*

## ULTRASOUND

Edward G. Grant, M.D.

*Department of Radiology, USC Norris Cancer Center,  
Los Angeles, CA., USA*

Juan P. Niedmann-Espinosa, M.D.

*Department of Ecotomography,  
Clinica Alemana de Santiago,  
Santiago de Chile, Chile*

## VASCULAR AND INTERVENTIONAL RADIOLOGY

Manuel Cifrian-Perez, M.D., Ph.D.

*Imaging Clinic Department,  
Hospital Universitario y Politecnico La Fe,  
Valencia, Spain*

## ARTIFICIAL INTELLIGENCE

Leonor Cerda-Alberich, Ph.D

*Imaging Clinic Department,  
Hospital Universitario y Politecnico La Fe,  
Valencia, Spain*

Felipe Campos Kitamura, M.D., Ph.D.

*Dasalnova, Dasa,  
Sao Paulo, Brazil*

## GRAPHICAL ABSTRACTS COMMITTEE

Oscar A. Chavez-Barba, M.D.

*Department of Radiology,  
Antiguo Hospital Civil de Guadalajara  
"Fray Antonio Alcalde",  
Guadalajara, Jal., Mexico*

Adriana Parada-Gallardo, M.D.

*Department of Radiology,  
Hospital General de Zapopan,  
Zapopan, Jal., Mexico*

J.M. Ignacio Lopez-Mendez, M.D.

*Department of Radiology and Imaging,  
Hospital de Especialidades, CMNO  
Instituto Mexicano del Seguro Social,  
Guadalajara, Jal., Mexico.*

Juan Pablo Lopez-Gutierrez, M.D.

*Department of Radiology and Imaging,  
Hospital General de Zona 3,  
Instituto Mexicano del Seguro Social  
Aguascalientes, Ags., Mexico*

Gerardo Llamas-Linares, M.D.

*Centro Universitario de Imagen Diagnostica,  
Hospital Universitario "Dr. Jose E. Gonzalez",  
Monterrey, N.L., Mexico*

Alejandra I. Castillo-Cervantes, M.D.

*Centro Universitario de Imagen Diagnostica,  
Hospital Universitario "Dr. Jose E. Gonzalez",  
Monterrey, N.L., Mexico*

A. Sofia Sanchez-Gomez, M.D.

*Department of Radiology,  
Grupo RIO Centro Integral de Diagnostico Medico.  
Guadalajara, Jal., Mexico*

## SOCIAL MEDIA COMMITTEE

Guillermo Elizondo-Riojas, M.D., Ph.D.

*Centro Universitario de Imagen Diagnostica,  
Hospital Universitario "Dr. Jose E. Gonzalez",  
Monterrey, N.L., Mexico*

Oscar A. Chavez-Barba, M.D.

*Department of Radiology,  
Antiguo Hospital Civil de Guadalajara  
"Fray Antonio Alcalde",  
Guadalajara, Jal., Mexico*

J. Mario Bernal-Ramirez, M.D.

*Department of Medical Clinics,  
Centro Universitario de Ciencias de la Salud,  
Universidad de Guadalajara,  
Guadalajara, Jal., Mexico*

Adriana Parada-Gallardo, M.D.

*Department of Radiology,  
Hospital General de Zapopan,  
Zapopan, Jal., Mexico*

## RADIOLOGICAL AND CLINICAL CORRELATION BOARD

### GASTROENTEROLOGY

Linda E. Muñoz-Espinosa, M.D., Ph.D.

*Liver Unit, Hospital Universitario  
"Dr. Jose E. Gonzalez",  
Monterrey, N.L., Mexico*

David Marti-Aguado, M.D., Ph.D.

*Servicio Medicina Digestiva,  
Hospital Clinico Universitario,  
Valencia, Spain*

### GASTROINTESTINAL AND GENERAL SURGERY

Carlos Nuño-Guzman, M.D., M.Sc.

*Department of Surgery,  
Antiguo Hospital Civil de Guadalajara  
"Fray Antonio Alcalde",  
Guadalajara, Jal., Mexico*

### OBSTETRICS AND GINECOLOGY

Sergio Fajardo-Dueñas, M.D., M.Sc.

*Division of Obstetrics and Gynecology,  
Nuevo Hospital Civil de Guadalajara,  
Guadalajara, Jal., Mexico*

### NEUROLOGY

Jose L. Ruiz-Sandoval, M.D., M.Sc.

*Department of Neurology,  
Antiguo Hospital Civil de Guadalajara  
"Fray Antonio Alcalde",  
Guadalajara, Jal., Mexico*

### RHEUMATOLOGY

Monica Vazquez del Mercado-Espinosa,  
M.D., Ph.D.

*Division of Medicine,  
Nuevo Hospital Civil de Guadalajara,  
Guadalajara, Jal., Mexico.*

### CARDIOLOGY-PNEUMOLOGY

Jose M. Hernandez, M.D.

*Department of Eocardiography, Doctors Hospital,  
Monterrey, N.L., Mexico*

### PATHOLOGICAL ANATOMY

Marco A. Ponce-Camacho, M.D., Ph.D.

*Department of Cytopathology, Doctors Hospital,  
Monterrey, N.L., Mexico*

### ENDOCRINOLOGY

Jesus Zacarias Villarreal-Perez, M.D.  
Department of Endocrinology,  
Hospital Universitario "Dr. Jose E. Gonzalez",  
Monterrey, N.L., Mexico

### HEMATOLOGY

Carlos R. Best-Aguilera, M.D.  
Department of Hematology,  
Hospital General de Occidente. Secretaria de Salud  
Zapopan, Jal., Mexico

### PEDIATRIC NEUROLOGY

Daniel Perez-Rulfo Ibarra, M.D., Ph.D.  
Departamento de Pediatría,  
Antiguo Hospital Civil de Guadalajara  
"Fray Antonio Alcalde",  
Guadalajara, Jal., Mexico

### GYNECOLOGICAL UROLOGY

Patricia I. Velazquez-Castellanos, M.D., M.Sc.  
Department of Gynecology and Obstetrics,  
Antiguo Hospital Civil de Guadalajara  
"Fray Antonio Alcalde",  
Guadalajara. Jal., Mexico

## Follow us



<https://linkedin.com/company/jmexfri>



<https://instagram.com/jmexfri>



<https://facebook.com/jmexfri>



<https://youtube.com/@jmexfri>



<https://x.com/jmexfri>



Original papers should be deposited in their electronic version through the following URL:

<https://publisher.jmexfri.permanyer.com>



**PERMANYER**  
[www.permanyer.com](http://www.permanyer.com)

#### Permanyer Mexico

Temistocles, 315  
Col. Polanco, Del. Miguel Hidalgo  
11560 Ciudad de Mexico  
[mexico@permnyer.com](mailto:mexico@permnyer.com)

#### Permanyer

Mallorca, 310 – Barcelona (Cataluña), España  
[permnyer@permnyer.com](mailto:permnyer@permnyer.com)

ISSN: 2696-8444

Ref.: 10130AMEX244

#### Reproductions for commercial purposes:

Without the prior written consent of the publisher, no part of this publication may be reproduced, stored in a retrievable medium or transmitted, in any form or by any means, electronic, mechanical, photocopying, recording or otherwise, for commercial purposes.

Journal of the Mexican Federation of Radiology and Imaging is an open access publication with the Creative Commons license CC BY-NC-ND (<http://creativecommons.org/licenses/by-nc-nd/4.0/>).

The opinions, findings, and conclusions are those of the authors. The editors and publisher are not responsible and shall not be liable for the contents published in the journal.

© 2024 Federacion Mexicana de Radiologia e Imagen, AC. Published by Permanyer.



[www.permanyer.com](http://www.permanyer.com)

## Diagnostic errors in radiology: where are we?

Gerardo E. Ornelas-Cortinas<sup>1,2\*</sup> and Ana K. Luna-Marroquin<sup>2</sup>

<sup>1</sup>Radiology and Imaging Department, Doctors Hospital AUNA; <sup>2</sup>Centro Universitario de Imagen Diagnostica, Hospital Universitario "Dr. Jose Eleuterio Gonzalez," Facultad de Medicina, Universidad Autonoma de Nuevo Leon. Monterrey, Nuevo Leon, Mexico.

Errors are the propensity for mistakes and an inherent human characteristic. They are considered the root of our cognitive limitations and the demands we encounter in our work environment. They cannot be avoided, but we must minimize them through appropriate systems<sup>1,2</sup>. In the medical field, the Committee on Quality of Health Care in America of the Institute of Medicine revealed in 1998 that 98,000 people die each year due to medical errors in hospitals, considering that more people die from hospital medication than from work accidents<sup>3</sup>.

Radiology is not exempt from errors. Several articles on the study of diagnostic error refer to the work of Dr. Leo H. Garland, a pioneer radiologist in the study of error in diagnostic imaging. He published that there were 30% of diagnostic errors in studies interpreted by experienced radiologists<sup>4</sup>. This statistic has not decreased over the years in later studies using imaging examinations with abnormal findings. However, in accordance with the daily practice of radiologists who see normal and abnormal studies, 3-5% of diagnostic errors have been found. Estimating that 1 billion radiological studies are performed worldwide, 30 to 50 million errors occur per diagnosis in radiology<sup>5</sup>.

Various types of errors have been reported, but the error classification of Kim and Mansfield is the most comprehensive<sup>6</sup>. Among the errors, the perception

error, in which the radiologist fails to perceive a finding that can be seen in retrospect, represents 60-80%. Other errors include under-reading, search satisfaction, location, technical situation, and complication. In this classification, under-reading, search satisfaction, and erroneous reasoning account for almost 75%<sup>6,7</sup>. Cognitive errors represent 20-40%, errors due to erroneous reasoning account for 9%, followed by errors due to report satisfaction, a lack of knowledge, clinical history, and over-reading. In addition, there are errors due to communication failure. Although these represent the lowest percentage, they significantly impact patients<sup>7</sup>.

Strategies have been proposed to mitigate diagnostic errors, among which perception errors and avoiding distractions are considered the most important. Who, in their daily practice, has not interpreted multiple MRI or CT images? Also, the phone does not stop ringing because your assistant has doubts about how a study is going to be registered, or the technician comes in saying that the patient is not cooperating to take an image or study with contrast medium, or doctors come to consult on a study, which is not the one you are reviewing and there is no one else in the interpretation area because colleagues are either doing other procedures or attending other doctors. After dealing with these

### \*Corresponding author:

Gerardo E. Ornelas-Cortinas

E-mail: ornelasge@yahoo.com.mx

2696-8444 / © 2024 Federación Mexicana de Radiología e Imagen, A.C. Published by Permanyer. This is an open access article under the CC BY-NC-ND (<https://creativecommons.org/licenses/by-nc-nd/4.0/>).

Received for publication: 21-09-2024

Accepted for publication: 24-09-2024

DOI: 10.24875/JMEXFRI.M2400085

Available online: 20-12-2024

J Mex Fed Radiol Imaging. 2024;3(4):205-207

[www.JMeXFRI.com](http://www.JMeXFRI.com)



distractions, the radiologist restarts interpreting the study where he left off or where he remembers when he was interrupted. What if the case that the radiologist was reviewing had a lesion in what is known as the corner of the image, and due to the distraction, attention was not paid to that first or last section of the study, and a finding was omitted? And in the next 5 minutes, while still immersed in the same study, a personal or hospital call comes in, and they ask to perform another procedure, and the interruption is repeated. Considering this, the interpretation process is constantly interrupted and prone to errors; thus, there is a thin line between making a mistake and making a correct diagnosis. This situation, which we consider to be a daily occurrence, is one of the main predicaments to which a radiologist is exposed that can generate interpretation errors.

Radiologists are not multitaskers. They should not feel that way; the people they interact with should know that. Do they call a surgeon during a procedure to ask about another patient? Is their process more important than that of a radiologist? Of course not! They work with human beings, and since the consultation on imaging methods is an important part of the diagnosis and treatment of patients, errors have a great impact because radiology reports influence diagnosis and treatment.

Erroneous reasoning errors are considered the third most frequent<sup>7</sup>, occurring in several ways. How many of us have made a diagnosis based on the first image that can explain the patient's diagnosis, as in the case of a patient with abdominal distension and pain in the upper right quadrant? A CT scan with contrast is requested, detecting a liver mass, and we stop looking at other areas because we prematurely close the case or fall into anchoring bias in that this is our diagnosis, and we do not allow ourselves to continue looking in other areas. Incidentally, in the case I mentioned, the patient's liver biopsy turned out to be a metastatic colon adenocarcinoma. In the retrospective CT study, the lesion was identified at the rectal level.

How many of us have overdiagnosed a possible pneumothorax due to a fold of soft tissue because, in the past, we forgot to describe one? It remains in our memory as a case of error, and we prefer to make a mistake by over-reading. How many times do we carry out or interpret a study quickly because we have some family or friend commitment in mind or we want to go back to watching a soccer match on our computer, and we decide to finish as soon as possible, with the risk of omitting some relevant finding? The question is, how many of us reflect at the end of the day on whether the

interpretations made during the workday were prone to bias that could lead to an error?

Among the strategies to mitigate errors, the review of cases by our peers has been mentioned. Some RIS and PACS systems have it integrated, considering that this tool can be beneficial, especially if, when we find an error, the person who made it is informed as feedback, making the error known. This strategy is considered an educational benefit and could help reduce interpretation errors, benefiting patients<sup>8</sup>. How many of your colleagues in hospitals in your community perform this practice in the recommended manner?

Will artificial intelligence prevent diagnostic errors? While it is true that there is great progress in artificial intelligence algorithms to detect lesions, it has been seen that the deep learning of these systems is still in process, and it is believed that it is not yet time to leave all the responsibility to artificial intelligence; however, this is a reality. We must face it, learn to use it, and use it for a second review of each study<sup>9</sup>. Should we fear AI? Definitely not. We should fear not accepting it and not learning to use it for our patient's benefit. We can maintain and coexist with technology to the extent that radiologists maintain efficient quality standards to mitigate diagnostic errors. It will depend on us not to be displaced. We must leave our comfort zone, learn, and be aware of this reality.

Although the recommendations to try to mitigate diagnostic errors in radiology are indeed well founded and knowing them and developing strategies to carry them out is an important part of the care processes in radiology departments, we believe that the fundamental purpose is to make radiologists aware of the fact that we are prone to errors daily. We should be aware of and avoid them. Radiologists in training who are immersed in new technology daily and viewing high-resolution monitors must be involved. Therefore, those who work in teaching centers are committed to teaching them that errors are inevitable but can be reduced with responsibility and commitment and without neglecting continuing medical education. It is even more important to convey to those dedicated to viewing images to make diagnoses that we must remember that behind an image, there is a human being who deserves all our professionalism, empathy, and responsibility as a fundamental part of mitigating errors in diagnostic imaging.

### **Funding**

Not applicable.

### **Conflicts of interest**

The author discloses no potential conflicts of interest.

### **REFERENCES**

1. Reason J: Human Error. First Ed. Cambridge University Press. New York, NY. USA. 1990.
2. Dekker S. The Field Guide to Understanding Human Error. 1a ed. Ashgate Publishing Limited. London, England. 2006.
3. Institute of Medicine (US) Committee on Quality of Health Care in America. To Err is Human: Building a Safer Health System. Kohn LT, Corrigan JM, Donaldson MS, editors. National Academies Press (US). Washington, DC. USA. 2000.
4. Garland LH. On the scientific evaluation of diagnostic procedures. *Radiology*. 1949. 52(3): 309–328.
5. Zhang L, Wen X, Li JW, Jiang X, Yang XF, Li M. Diagnostic error and bias in the department of radiology: a pictorial essay. *Insights Imaging*. 2023;14(1):163. doi: 10.1186/s13244-023-01521-7.
6. Kim YW, Mansfield LT. Fool me twice: delayed diagnoses in radiology with emphasis on perpetuated errors. *AJR Am J Roentgenol* 2014;202(3): 465–447. doi:10.2214/AJR.13.11493.
7. Bruno MA, Walker EA, Abujudeh HH. Understanding and Confronting Our Mistakes: The Epidemiology of Error in Radiology and Strategies for Error Reduction. *RadioGraphics*. 2015; 35 (6):1668-1676. doi: 10.1148/rg.2015.150023.
8. Itri JN, Tappouni RR, McEachern RO, Pesch AJ, Patel SH. Fundamental of diagnostic error in imaging. *RadioGraphics* 2018; 38 (6):1845–1865. doi: 10.1148/rg.2018180021. PMID: 30303801.
9. Lenskjold A, Nybing JU, Trampedach C, Galsgaard A, Brejnebøl MW, Raaschou H, et al. Should artificial intelligence have lower acceptable error rates than humans? *BJR Open*. 2023;5(1):20220053. doi: 10.1259/bjro.2022.0053.

# I see double! Searching for the abnormal cranial nerve in diplopia

Angela Guarnizo<sup>1\*</sup>  and Carlos Torres<sup>2,3</sup> 

<sup>1</sup>Department of Radiology, Division of Neuroradiology, Hospital Universitario Fundacion Santa Fe de Bogota, Bogota, Colombia; <sup>2</sup>Department of Medical Imaging, The Ottawa Hospital; Civic Campus, Ottawa, Ontario, Canada; <sup>3</sup>Department of Radiology, Radiation Oncology and Medical Physics, University of Ottawa, Ottawa, Ontario, Canada

## ABSTRACT

Diplopia or double vision is a common symptom that can be caused by various neurological or ophthalmologic pathologies. Diplopia can be monocular or binocular. In monocular diplopia, the patient sees double with only one eye open. In binocular diplopia, the patient sees double with both eyes open with subsequent resolution of the symptom when one of the eyes is closed. Binocular diplopia is the main manifestation caused by involvement of cranial nerves III, IV and VI. Infections, inflammatory, vascular, degenerative, traumatic, iatrogenic and malignant pathologies can cause diplopia. The combination of medical history, physical examination and imaging is crucial for an accurate diagnosis. Magnetic resonance imaging (MRI) of the brain and orbits with contrast is the modality of choice for the evaluation of patients with diplopia. Computed tomography (CT) of the head without contrast is useful to rule out lesions of the bones and skull base. Imaging of the brain and orbits allows assessment of the normal anatomy of cranial nerves III, IV and VI, and is useful to identify and characterize the various pathologies causing diplopia.

**Keywords:** Diplopia. Cranial nerve palsy. Cranial nerves III, IV and VI. Computed tomography. Magnetic resonance imaging.

## INTRODUCTION

Diplopia or double vision is a common symptom that can be caused by various neurological or ophthalmologic pathologies. The clinical history and physical examination are important to make an accurate diagnosis and plan treatment. Imaging is a key component of the diagnostic algorithm as it helps to assess the anatomy of the orbits and cranial nerves. Herein we review the normal anatomy and the most common lesions that can affect cranial nerves III, IV and VI, that are often responsible for patient's diplopia.

## TYPES OF DIPLOPIA

Diplopia can be monocular or binocular. In monocular diplopia, the patient sees double with only one eye open, usually due to intraocular pathologies such as

refractive problems, dry eyes, bad lenses, cataracts and uveitis, among other causes. In these cases, imaging is not required, and a detailed ophthalmologic examination should be performed<sup>1-3</sup>. In binocular diplopia, the patient sees double with both eyes open with subsequent resolution of the symptom when one of the eyes is closed<sup>3,4</sup>. This type of diplopia is caused by misalignment of the visual axes and requires an imaging examination to rule out possible underlying pathologies, some of them life-threatening<sup>1,2</sup>.

## NORMAL ANATOMY

Cranial nerves III, IV and VI control eye muscle movements. It is important to be familiar with the anatomy of these cranial nerves and their course from the brainstem to the orbit along the subarachnoid space, cavernous sinus and superior orbital fissure (Figure 1)<sup>1,5</sup>.

### \*Corresponding author:

Angela Guarnizo  
E-mail: [angela.guarnizo@fsfb.org.co](mailto:angela.guarnizo@fsfb.org.co)

Received for publication: 21-08-2024

Accepted for publication: 30-08-2024

DOI: 10.24875/JMEXFRI.M24000084

Available online: 20-12-2024

J Mex Fed Radiol Imaging. 2024;3(4):208-220

[www.JMeXFRI.com](http://www.JMeXFRI.com)

2696-8444 / © 2024 Federación Mexicana de Radiología e Imagen, A.C. Published by Permanyer. This is an open access article under the CC BY-NC-ND (<https://creativecommons.org/licenses/by-nc-nd/4.0/>).

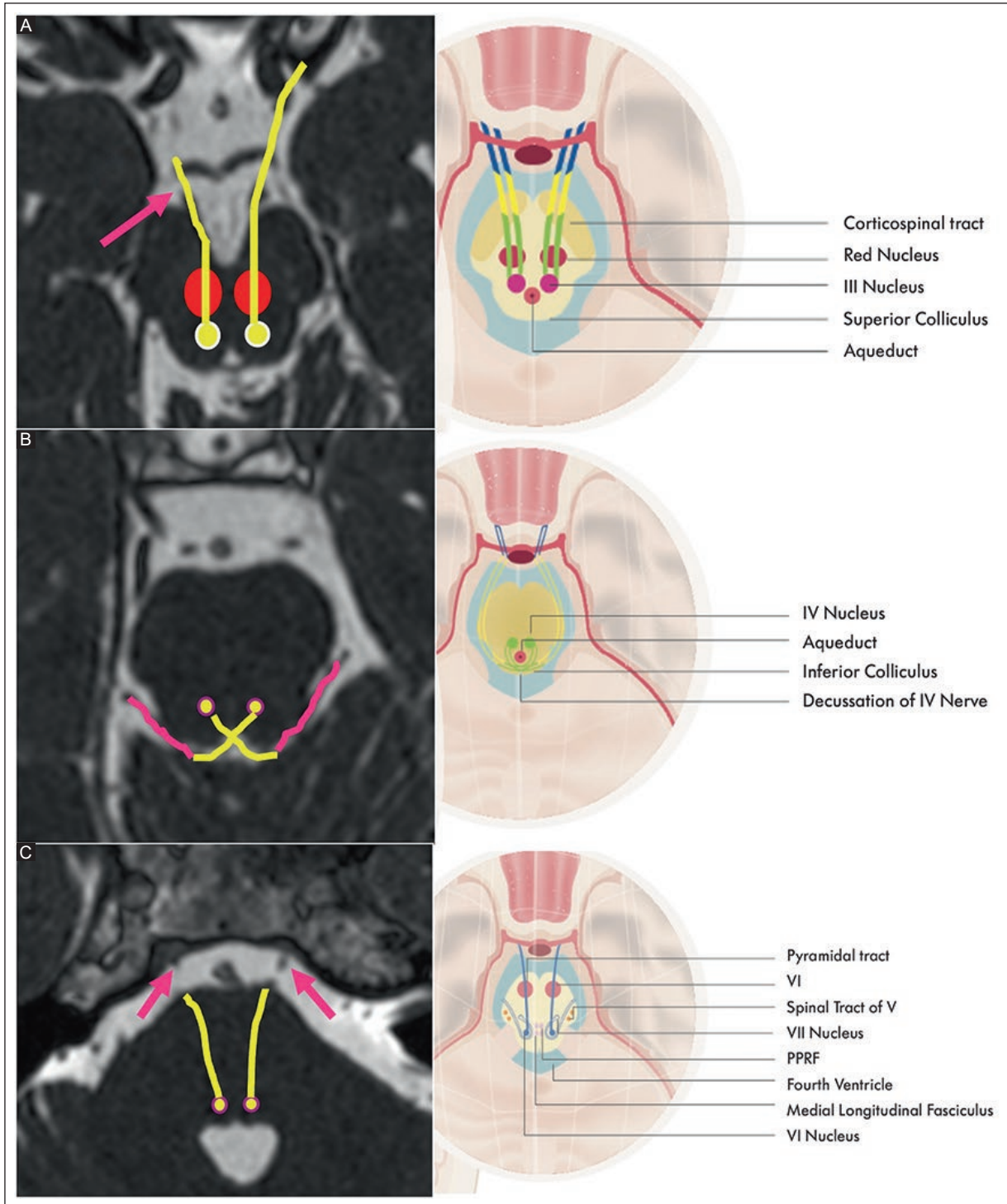


**Figure 1.** MRI and illustrations of the normal anatomy of the cranial nerves III, IV and VI. **A:** T2W axial view shows the course of cranial nerve III from its nucleus (yellow circles and lines) to the interpeduncular cistern, below the P1 segment of the PCA (arrows). **B:** T2W axial view shows the nucleus of cranial nerve IV along the dorsal side of the pons at the level of the inferior colliculus (yellow circles). The cranial nerve IV decussates and exits dorsally (yellow and pink lines). **C:** T2W axial view of the pons at the level of the fourth ventricle shows the course of the cranial nerve VI from the nucleus (yellow circles and lines) and along the cisternal segments within the preontine cistern (arrows).

MRI: magnetic resonance imaging; PCA: posterior cerebral artery.

### **Cranial nerve III**

The oculomotor nerve or cranial nerve III is a somatic motor nerve with efferent fibers that innervates the superior, medial and inferior recti muscles, as well as the inferior oblique and levator palpebrae muscles. It also has a parasympathetic function supplying the ciliary and pupillary sphincter muscles through the Edinger-Westphal nucleus<sup>6,7</sup>. Cranial nerve III nuclei are located in the midbrain, at the level of the superior colliculi, bound inferiorly and laterally by the medial longitudinal fasciculus (MLF), anterior to the cerebral aqueduct<sup>1,5,7</sup>. The Edinger-Westphal nuclei are situated dorsally in the periaqueductal gray matter<sup>7</sup>. The fibers run anteriorly through the midbrain tegmentum and red nucleus and exit the midbrain along the medial aspect of the interpeduncular cistern, between the posterior cerebral artery (PCA) and superior cerebellar artery (SCA) and continue anteriorly below the posterior communicating artery (P-comm)<sup>1,7,8</sup>. The parasympathetic fibers run peripherally along the nerve<sup>7</sup>. Cranial nerve III then enters the dura and runs along the superior lateral wall of the cavernous sinus, above the trochlear nerve<sup>1</sup>. Subsequently, the nerve enters the orbit through the superior orbital fissure and passes through the annulus of Zinn, where it divides into its superior and inferior branches. The superior branch provides innervation to the superior rectus and the levator palpebrae muscles, while the inferior branch innervates the inferior rectus, the medial rectus and the inferior oblique muscles. The preganglionic parasympathetic fibers of the nerve synapse in the ciliary ganglion. Postganglionic parasympathetic fibers continue as short ciliary nerves that join with sympathetic fibers from the internal carotid artery (ICA) that enter the eyeball and control the pupillary sphincter and ciliary muscle<sup>1,8,9</sup>.

### **Cranial nerve IV**

The trochlear nerve is the cranial nerve with the longest intracranial course. It is a somatic motor nerve that gives innervation to the superior oblique muscle. The nucleus is at the level of the inferior colliculus in the midbrain, ventral to the aqueduct<sup>5</sup>. The fibers run posteriorly and inferiorly around the cerebral aqueduct, where they decussate before exiting the midbrain<sup>7</sup>. It is the only cranial nerve exiting from the dorsal brainstem and crossing to the opposite side<sup>1</sup>; each superior oblique muscle is therefore innervated by the contralateral cranial nerve IV. The cisternal segment runs along the ambient cistern, inferior and lateral to cranial nerve III,

between the posterior cerebral artery and the superior cerebellar artery<sup>7</sup>. In the cavernous segment, cranial nerve IV runs along the lateral wall of the cavernous sinus, below the oculomotor nerve, then passes through the superior orbital fissure above the annulus of Zinn, and innervates the superior oblique muscle<sup>7,8</sup>.

### **Cranial nerve VI**

The abducens nerve or cranial nerve VI is a motor nerve that innervates the lateral rectus muscle. The nuclei are located within the pontine tegmentum, near the midline. The axons of the facial nerves loop around the cranial nerve VI nuclei at the facial colliculus, causing a bulge in the floor of the fourth ventricle. The fibers of cranial nerve VI run anteriorly and leave the pons at the bulbo-pontine sulcus<sup>1,8</sup>. The nerve then runs anteriorly through the prepontine cistern, pierces the dura, and then goes into Dorello's canal, also known as the intradural segment. After passing through the basilar venous plexus, the nerve turns over the petrous apex and enters the cavernous sinus<sup>7,8</sup>. It is the only cranial nerve that runs within the venous sinusoids of the cavernous sinus<sup>7</sup> (Figure 2). It then enters the orbit through the superior orbital fissure, goes through the annulus of Zinn and innervates the lateral rectus muscle<sup>7,8</sup>.

## **OCULAR MOTOR MUSCLES**

There are six ocular motor muscles: lateral, superior, medial and inferior recti muscles and two oblique muscles (superior and inferior oblique muscles). The recti muscles and superior levator palpebrae muscle are inserted into the ring of Zinn around the optic nerve at the orbital apex. They follow an anterior course, pass through Tenon's capsule and insert into the sclera. The oblique muscles insert into the posterior and lateral section of the eyeball. As long as tonic innervation is maintained, the medial rectus muscle, the strongest of the extraocular muscles, helps to reduce spontaneous diversion of the eyeballs<sup>10</sup>.

## **IMAGING APPROACH**

Magnetic resonance imaging (MRI) of the brain and orbits with contrast is the modality of choice for the assessment of patients with diplopia. Due to its excellent spatial and contrast resolution, it allows adequate identification of the oculomotor cranial nerves throughout their course. It is also the best examination for the detection of pathology in the posterior fossa, including

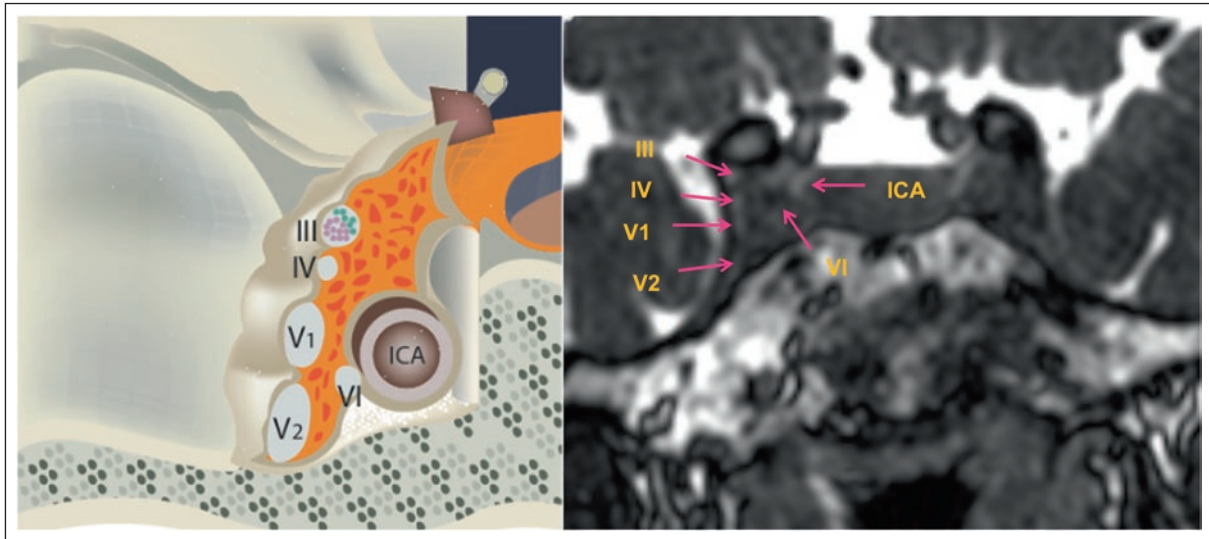


**Figure 2.** Illustration and MRI T2W coronal view through the cavernous sinus showing the cranial nerves as black dots in the cavernous sinus (arrows).

ICA: internal carotid artery; MRI: magnetic resonance imaging.

small infarcts<sup>10</sup>. In the assessment of cisternal segment of the oculomotor cranial nerves, T2-weighted sequences can be used, either fast gradient echo (FGE) or fast spin echo (FSE) techniques<sup>11</sup>.

Head computed tomography (CT) without contrast is useful to rule out bone and skull base lesions. Moreover, head CT is useful when MRI is contraindicated, in the context of trauma or if a rapid acquisition is needed<sup>10</sup>. CT or magnetic resonance angiography (MRA) must be performed if there is suspicion of non-ruptured aneurysm, especially in the clinical context of third cranial nerve palsy<sup>10</sup>.

## EVALUATION OF PATIENTS WITH BINOCULAR DIPLOPIA

Binocular diplopia is the main symptom resulting from involvement of cranial nerves III, IV and VI. Therefore, a thorough understanding of the anatomy and the common pathologies that can affect these cranial nerves is critical when performing imaging studies, to adequately find and interpret the potential underlying cause.

In patients with cranial nerve palsy, it is important to know if it is an isolated cranial nerve palsy or if multiple cranial nerves are involved, and whether other neurological symptoms are present<sup>12</sup>. Isolated ocular nerve palsy is usually due to a central lesion. In case of third cranial nerve palsy patients, present with ptosis, fixed pupillary dilation and the affected eye in a “down and out” position. Ptosis may be absent due to lack of

involvement of the single subnucleus controlling the levator palpebrae muscle. Similarly, one or both pupils may be involved because of the rostral location of the paired Edinger Westphal nuclei<sup>12</sup>. Moreover, fourth cranial nerve palsy is rare and occurs with contralateral palsy due to its decussation. It is the most common cause of vertical diplopia, while horizontal diplopia is usually caused by sixth cranial nerve palsy<sup>2</sup>.

When patients develop multiple cranial nerve palsies, several possibilities must be considered, including cerebrospinal fluid-based process affecting the cranial nerves in the subarachnoid space, a neuromuscular junction process, especially if the patient complains of tiredness at rest and diplopia<sup>1</sup> and an inflammatory cranial neuropathy<sup>12</sup>. If there is pathologic involvement of the cavernous sinus, the third, fourth and sixth cranial nerves as well as the first and second divisions of the trigeminal nerve may be involved.

Microvascular ischemia is one of the leading causes of acquired ocular motor cranial nerve palsy, often occurs in patients older than 50 years, and is associated with diabetes, arterial systemic hypertension, smoking and atherosclerosis<sup>13</sup>. In these cases, approximately 86% of patients achieve complete resolution and about 14% will have incomplete recovery<sup>14</sup>. In 13%-35% of cases, the cause remains undetermined. Idiopathic sixth cranial nerve palsy has been described in approximately 26% of cases, with usual recovery in 3 to 6 months, in some cases, however recurrence may occur or persist beyond this time<sup>15</sup> (Figure 3).

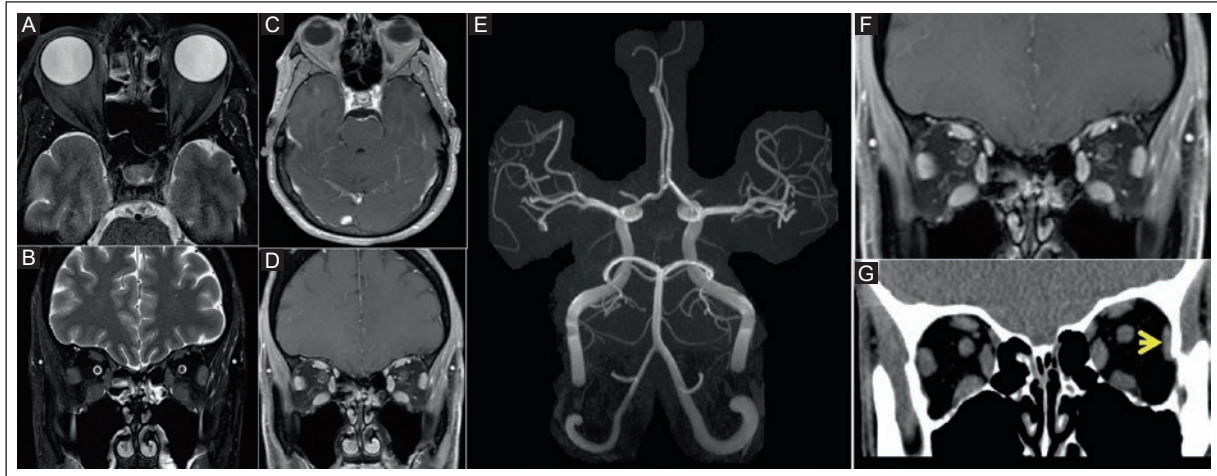


**Figure 3.** 46-year-old man with diplopia and isolated left sixth cranial nerve palsy. **A-B:** MRI T2W axial and coronal views with fat sat show normal size and signal of extraocular muscles. **C-D:** MRI T1W axial and coronal views with Gad show no mass or abnormal enhancement. **E:** 3D TOF MRA shows no concerning vascular abnormality. **F:** coronal MRI T1W view with Gad at the time of symptoms shows normal appearance of extraocular muscles. **G:** CT coronal view 1 month later shows a reduction in the size of the left lateral rectus muscle due to denervation atrophy (arrow). The definitive diagnosis from neuroophthalmology was idiopathic sixth cranial nerve palsy. The patient completely recovered from the symptoms 6 months later.

CT: computed tomography; Gad: gadolinium; MRA: magnetic resonance angiography; MRI: magnetic resonance imaging; TOF: Time of Flight.

### Nuclear segment

Diplopia secondary to brainstem lesions is usually associated with other neurological symptoms including hemiparesis, abnormal movements and cerebellar signs<sup>2</sup>. For example, strokes are often associated with contralateral hemiplegia due to the involvement of corticospinal tract fibers. If the stroke extends to the red nucleus, patients present with ipsilateral ophthalmoplegia and intentional tremor<sup>1</sup>. Fascicular lesions of the third cranial nerve may be associated with hemiparesis, ataxia or tremor from involvement of the adjacent corticospinal tracts, red nucleus, brachium conjunctivum and cerebellar peduncles. Fourth cranial nerve palsy may be associated with ipsilateral internuclear ophthalmoplegia, Horner's syndrome or contralateral afferent pupillary defect from involvement of the medial longitudinal fasciculus, descending oculosympathetic fibers or pupillary axons in the brachium of the superior colliculus. In addition, sixth cranial nerve nuclear lesions can affect the adjacent medial longitudinal fasciculus and present with one-and-a-half syndrome<sup>12</sup>.

The facial colliculus is the area formed by the sixth cranial nerve nucleus and the surrounding fibers of the facial nerve<sup>16</sup>. Facial colliculus syndrome results from a lesion in the pontine tegmentum along the floor of the fourth ventricle, causing sixth cranial nerve palsy and impairment of the genu fibers of the facial nerve and medial longitudinal fasciculus<sup>17</sup> (Figure 4). It is important

to assess the basilar artery for potential thrombus or increased attenuation of the vessel on CT or lack of flow on MRI, MRA or computed tomography angiography (CTA), which can cause stroke in the midbrain or pons<sup>1</sup>. Lesions along the medial longitudinal fasciculus can present with lateral gaze problems and nystagmus due to involvement of the vestibular oculomotor fibers<sup>1</sup>.

Other pathologies involving the nuclear segment include multiple sclerosis (MS), infection, vascular lesions and tumors. In fact, central nervous system (CNS) neoplasms correspond to 1%-15% of cases presenting with ocular cranial nerve palsy<sup>14</sup>. About 38% of patients with MS have diplopia. Although it is unusual to find isolated paralysis of the third, fourth and sixth cranial nerves, approximately 10%-24% of the patients with MS develop sixth cranial nerve palsy<sup>18</sup> (Figure 5). Metabolic causes include Wernicke's encephalopathy caused by thiamine deficiency and characterized by ophthalmoplegia, ataxia and encephalopathy<sup>19</sup>. Imaging findings include bilateral symmetric T2-weighted and FLAIR hyperintensities in the medial thalami, mammillary bodies, periaqueductal gray matter, and putamina; 50% of cases show enhancement and restricted diffusion in these areas<sup>20</sup>.

Listeria meningoenzephalitis is a common cause of CNS infection in immunocompromised patients, usually presenting as rhombencephalitis. Patients present with headache, vomiting and fever, followed by cranial nerve palsy, cerebellar and long tract motor and sensory

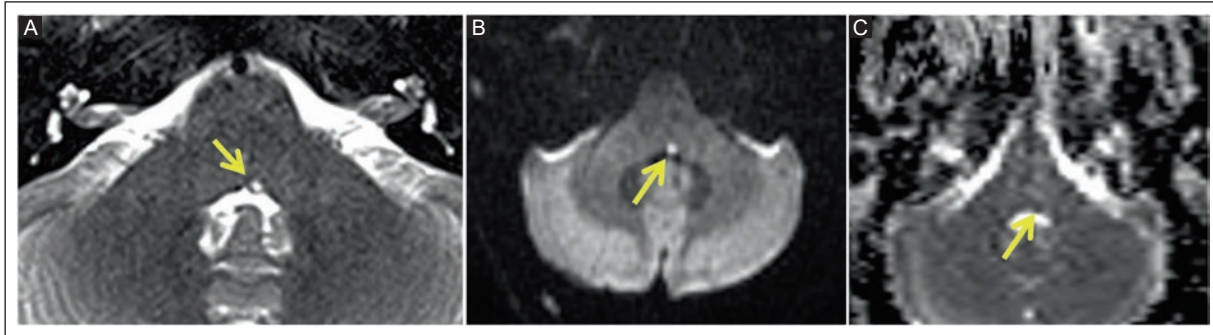


**Figure 4.** MRI in a 42-year-old woman with sudden onset of diplopia. **A:** T2W axial. **B:** DWI axial. **C:** ADC map show a focus of restricted diffusion and high T2W signal at the level of the left facial colliculus consisting with an acute infarct involving the nucleus of left cranial nerve VI (arrows) and the adjacent fibers of left cranial nerve VII (facial colliculus syndrome).

ADC: apparent diffusion weighted; DWI: diffusion weighted imaging; MRI: magnetic resonance imaging.

deficits. Brain MRI shows areas of high T2 signal involving the pons and medulla, as well as ring enhanced lesions when microabscesses are present<sup>21,22</sup>.

### Cisternal segment

In patients presenting with diplopia, ptosis and poorly reacting pupil, it is important to rule out an aneurysm. Extrinsic compression of the cranial nerves by an aneurysm can lead to denervation atrophy of the extraocular muscles causing diplopia<sup>1</sup>. In approximately 9% to 36% of cases, diplopia is caused by an intracranial aneurysm, and P-comm aneurysms present with third cranial nerve palsy in 30%-60% of cases<sup>23</sup>. Therefore, in cases of isolated third cranial nerve palsy with new ptosis, a P-comm aneurysm must be excluded (Figure 6).

Other vascular pathologies that can compress the cisternal segment of the cranial nerves and lead to diplopia include vascular malformations, vasculitis and dissection. In patients with Horner's syndrome presenting with binocular diplopia, mydriasis, ptosis and anhidrosis, carotid dissection should be suspected. CTA or MRA must be performed to assess the vessel lumen and the arterial wall and to rule out the presence of intramural hematoma<sup>23</sup>.

Increased intracranial pressure is another possible cause of diplopia, particularly due to paralysis of cranial nerves IV or VI secondary to their compression along the petrous temporal ridge. Patients with uncal herniation can present with third cranial nerve palsy and blown pupil<sup>1,13</sup>. In cases of trauma, avulsion of the nerve trunk, especially the fourth cranial nerve due to its longer course, and shearing while crossing the petroclinoid ligament should be considered<sup>13</sup>. Idiopathic intracranial hypertension is a cause of sixth cranial nerve palsy due to the downward

displacement of the brainstem and subsequent stretching of cranial nerve VI in Dorello's canal<sup>13,24</sup>.

Infections, inflammatory processes and neoplasms, such as meningeal carcinomatosis or lymphoma can also affect the cisternal segment of the cranial nerves. Miller-Fisher syndrome, one of the non-classical forms of Guillain Barré syndrome, presents with partial or complete ophthalmoplegia, sensory ataxia and areflexia; brain MRI of these patients may show cranial nerve enhancement<sup>19</sup>. Inflammatory diseases of the meninges such as sarcoidosis, IgG4, Granulomatosis with polyangiitis (GPA) among others may also affect the cisternal segment of the oculomotor cranial nerves. Imaging findings include nodular thickening and enhancement of the meninges, predominantly in the perimesencephalic cisterns<sup>6</sup> (Figure 7). Superficial siderosis, as a result of prior subarachnoid hemorrhage, may also cause oculomotor cranial nerve dysfunction<sup>25</sup>.

Neoplasms such as schwannomas, meningiomas, carcinomatosis or lymphomas can affect the course of cranial nerves III, IV and VI (Figure 8). Clival lesions like metastases, meningiomas, chordomas or chondrosarcomas affect the sixth cranial nerve in about 45% of cases<sup>1,6</sup>.

Infection can also affect the cisternal segment of cranial nerves III, IV and VI. Lyme neuroborreliosis, one of the most common vector-borne diseases in North America and Europe, often presents with cranial nerve deficits, including facial, trigeminal and oculomotor nerve palsies, with predominant involvement of cranial nerve III. Imaging findings are nonspecific and include abnormal white matter foci of high T2 signal, predominantly in the frontal lobes, potentially mimicking demyelinating disease. Smooth enhancement along the course of the cranial nerves is also a typical feature. Although imaging findings are not specific, attention should be paid to



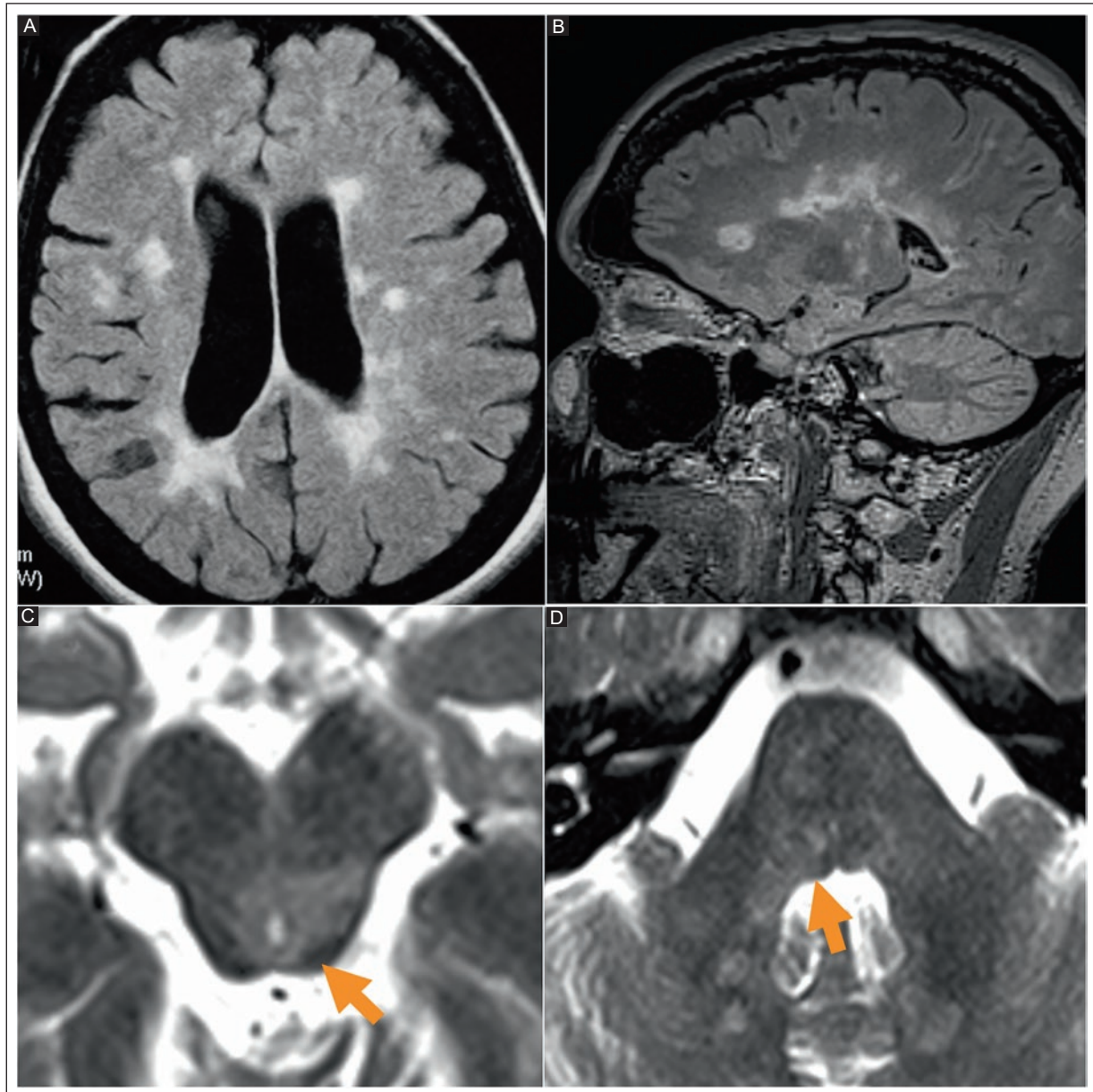


**Figure 5. A-B:** MRI axial and sagittal FLAIR views show multiple foci of high signal in the subcortical and periventricular white matter. **C:** T2W axial view at the level of the midbrain and **D:** at the level of the pons respectively showing foci of high signal involving the nucleus of cranial nerves III and VI (arrows) in a patient with MS and diplopia.

MRI: magnetic resonance imaging; MS: multiple sclerosis.

patients with a history of travel to endemic areas, presenting with flu-like symptoms and cranial neuropathies, with white matter hyperintensities and enhancement of multiple cranial nerves on MRI<sup>26-28</sup>.

### ***Intradural segment or Dorello's canal***

The sixth cranial nerve has an intradural segment from the posterior aspect of the clivus to the petrous apex, enclosed in a fibrous sheath known as Dorello's canal.

This segment of the sixth cranial nerve is susceptible to skull base fractures and perineural spread from adjacent tumors. Gradenigo syndrome, characterized by the triad of petrous apicitis, sixth cranial nerve palsy and facial pain, can also affect this segment<sup>13</sup>.

### ***Cavernous segment***

The cavernous segment of cranial nerves III, IV and VI may be affected by mass effect from tumors arising

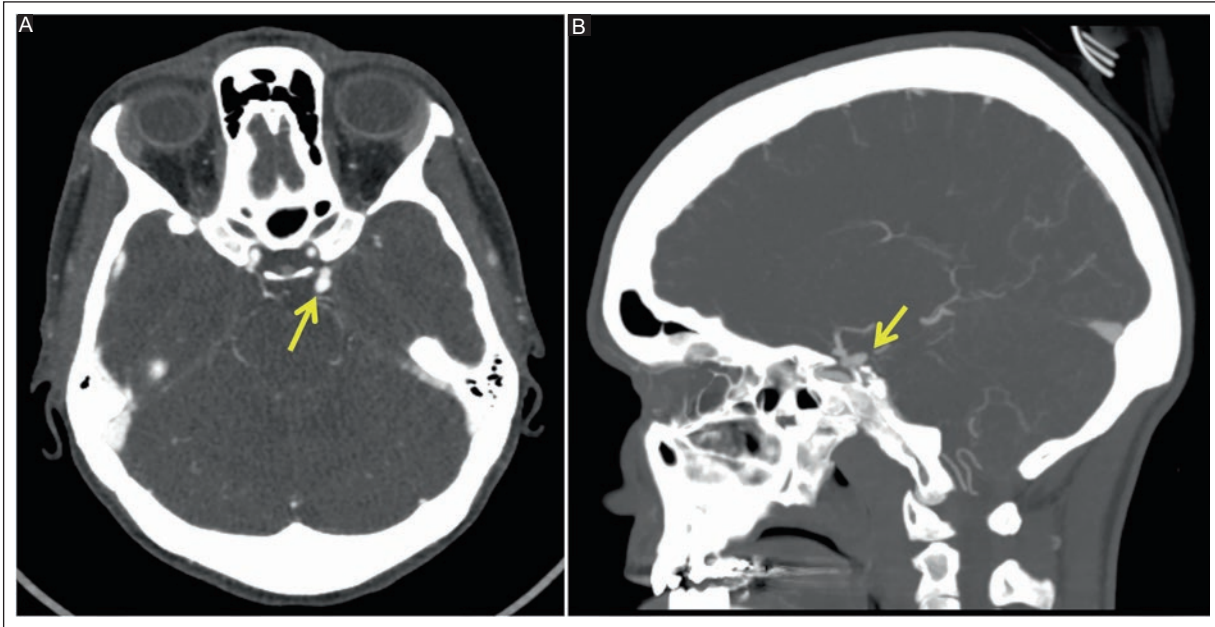


**Figure 6.** **A:** axial and **B:** sagittal CTA images showing a left P-comm aneurysm in a patient with left third cranial nerve palsy and headache.

CTA: computed tomography angiography; P-comm: posterior communicating artery.

from the sellar and parasellar regions, the skull base, the paranasal sinuses or from the cavernous sinus itself<sup>6</sup>. Cavernous sinus lesions can cause third cranial nerve palsy in combination with fourth, fifth (V1 and V2) and/or sixth cranial nerve palsies. In cases of unilateral Horner's syndrome and sixth cranial nerve palsy, a cavernous sinus lesion should be excluded<sup>12</sup>.

Meningioma is the most common mass that can cause oculomotor nerve palsy with about 15% of meningiomas arising from the parasellar region. In these cases, the nerve dysfunction is usually due to direct invasion of the cavernous sinus<sup>6</sup>. Oculomotor nerve dysfunction due to a pituitary tumor is less common, with isolated third cranial nerve palsy being the most common symptom. The mechanism of third cranial nerve palsy is related to its horizontal position in the same plane as the pituitary gland. Pressure from the lateral growth of pituitary tumors leads to compression of the cavernous sinus, a pressure that is transmitted to the third cranial nerve. Due to the increased pressure, the third cranial nerve is compressed between the tumor and the interclinoid ligament, leading to palsy<sup>29</sup> (Figure 9).

Cavernous sinus thrombosis is a potential complication of paranasal sinus and midface infection. *Staphylococcus aureus* accounts for 70% of cases, while *Streptococcus*

*pneumoniae*, gram-negative bacilli, anaerobes and fungi are less common. 80% to 100% of cases present with acute onset of fever, proptosis, chemosis, ptosis and paralysis of cranial nerves III, IV and VI; 50% to 80% develop periorbital edema, headache, altered sensorium, optic nerve edema and venous congestion. CT and MRI show cavernous sinus enlargement with irregular filling defects, proptosis, dilatation of the superior ophthalmic vein and orbital fat stranding<sup>6,2</sup>.

Carotid cavernous fistula (CCF) is an acquired vascular malformation consistent with an abnormal connection between the cavernous sinus and the carotid artery. They can be classified as direct or indirect. The direct type corresponds to a direct communication between the carotid artery and the cavernous sinus. It is usually associated with trauma, rupture of ICA aneurysm or iatrogenic carotid injury, and typically it is a high flow vascular malformation. The indirect type is usually due to an abnormal communication between the branches of the ICA and the cavernous sinus. It is thought to be due to primary thrombosis of the cavernous sinus outflow which causes an abnormal flow of the blood through the venous system and the subsequent development of an arteriovenous fistula. This type of CCF may develop in the setting of hypertension, fibromuscular dysplasia or Ehlers-Danlos<sup>30</sup>.

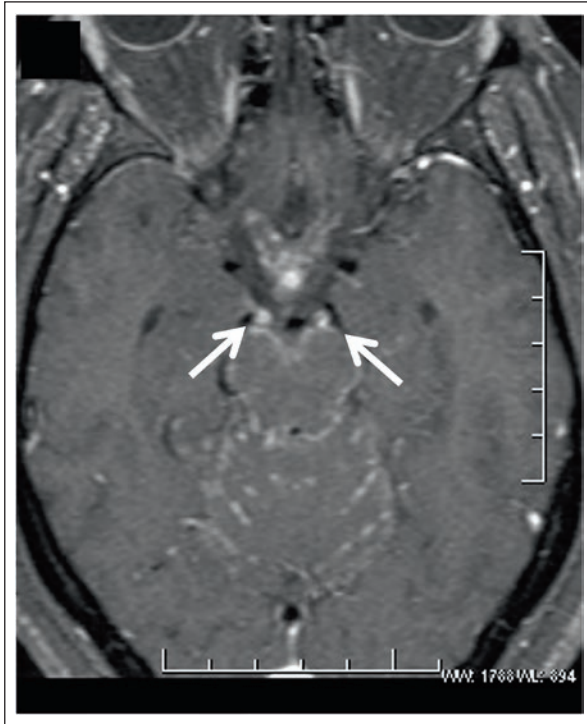


**Figure 7.** MRI of a 40-year-old woman with cranial nerve abnormalities and headache. T1W axial view with Gad shows nodular leptomeningeal enhancement along the surface of the midbrain and involving the cisternal segment of cranial nerves II and III (arrows) in a patient with sarcoidosis.

Gad: gadolinium; MRI: magnetic resonance imaging.

Clinical signs and symptoms result from arterialization of the orbital venous flow and include proptosis, chemosis, orbital bruits, headache and diplopia. In these cases, diplopia results from cranial nerve involvement in the cavernous sinus, with cranial nerve VI being the most commonly affected due to its proximity to ICA<sup>30</sup>. On head CT imaging, findings suspicious of CCF include dilatation of the cavernous sinus and superior ophthalmic vein with associated proptosis and enlargement of the extraocular muscles. MRI shows flow-related enhancement of the cavernous sinus with flow voids within the superior ophthalmic vein and petrosal veins. On dynamic subtraction angiography, abnormal arterial shunting from the ICA or dural arteries to the cavernous sinus confirms the diagnosis<sup>6</sup> (Figure 10).

Some pathologies that affect the cavernous sinus may also extend to the apex of the orbit including metastases, lymphoma, leukemia, Tolosa – Hunt syndrome, and dural arteriovenous fistulas (dAVF). In these cases, T1-weighted images with contrast and fat suppression are helpful in detecting subtle pathologic involvement of the orbital apex and superior orbital fissure<sup>25</sup>.

## Orbital segment

Trauma, neoplasms, infections and inflammatory processes are the most common causes of oculomotor nerve dysfunction in this segment<sup>13</sup>. Patients usually present with a combination of paralysis of cranial nerves III, IV and VI, proptosis and pain.

Schwannomas usually arise from the V1 branch of the trigeminal nerve, although schwannomas of cranial nerves III and IV have also been described<sup>6</sup>. Primary tumors of the head and neck and tumors from the paranasal sinuses may also extend to the orbit and present with diplopia due to external compression or invasion. Metastases must be included in the differential, often secondary to breast, lung and kidney cancer as well as melanoma<sup>6</sup> (Figure 11). Extraocular muscle enlargement can also be observed in vascular malformations such as carotid cavernous fistula or dAVF<sup>13</sup>.

In cases of infection or inflammation, motor ocular nerve palsy is often the result of direct involvement of the extraocular muscles<sup>6</sup>. Thyroid eye disease, a lymphocytic inflammatory infiltration of the orbital tissue is the most common inflammatory cause and occurs in approximately 50% of patients with Graves' disease and in some with Hashimoto's thyroiditis. Smoking, family history and female gender are risk factors<sup>4</sup>. Differential diagnoses include idiopathic orbital inflammation or orbital pseudotumor, sarcoid, rheumatoid arthritis, vasculitis, or immunoglobulin IgG4-related eye disease<sup>4,13</sup>. Proptosis, periorbital edema, retrobulbar resistance, and eyelid retraction are some of the ocular symptoms seen in patients with thyroid eye disease. In cases of retrobulbar resistance, in which there is limitation in the degree of backward movement of the eyeball when gently pushed on with two fingers during eye closure, a retroorbital mass or thyroid eye disease should be ruled out<sup>4</sup>.

Penetrating trauma and fractures are the most common cause of diplopia. In the context of traumatic injury, diplopia occurs when there is disturbance in ocular motility secondary to intraorbital tissue edema or due to entrapment of the extraocular muscles, orbital fat, or both, within the fracture defect. It may also be the consequence of direct damage to the extraocular muscles<sup>31</sup>. Silent sinus syndrome, which presents with maxillary sinus atelectasis and subsequent inferior displacement of the orbital floor is associated with enophthalmos and hypoglobus of the eye, which can lead to vertical diplopia<sup>4</sup>. Metabolic diseases causing muscle atrophy as in Kearns-Sayre syndrome or muscle junction abnormality due to myasthenia gravis should be included in the differential diagnosis<sup>13</sup>.

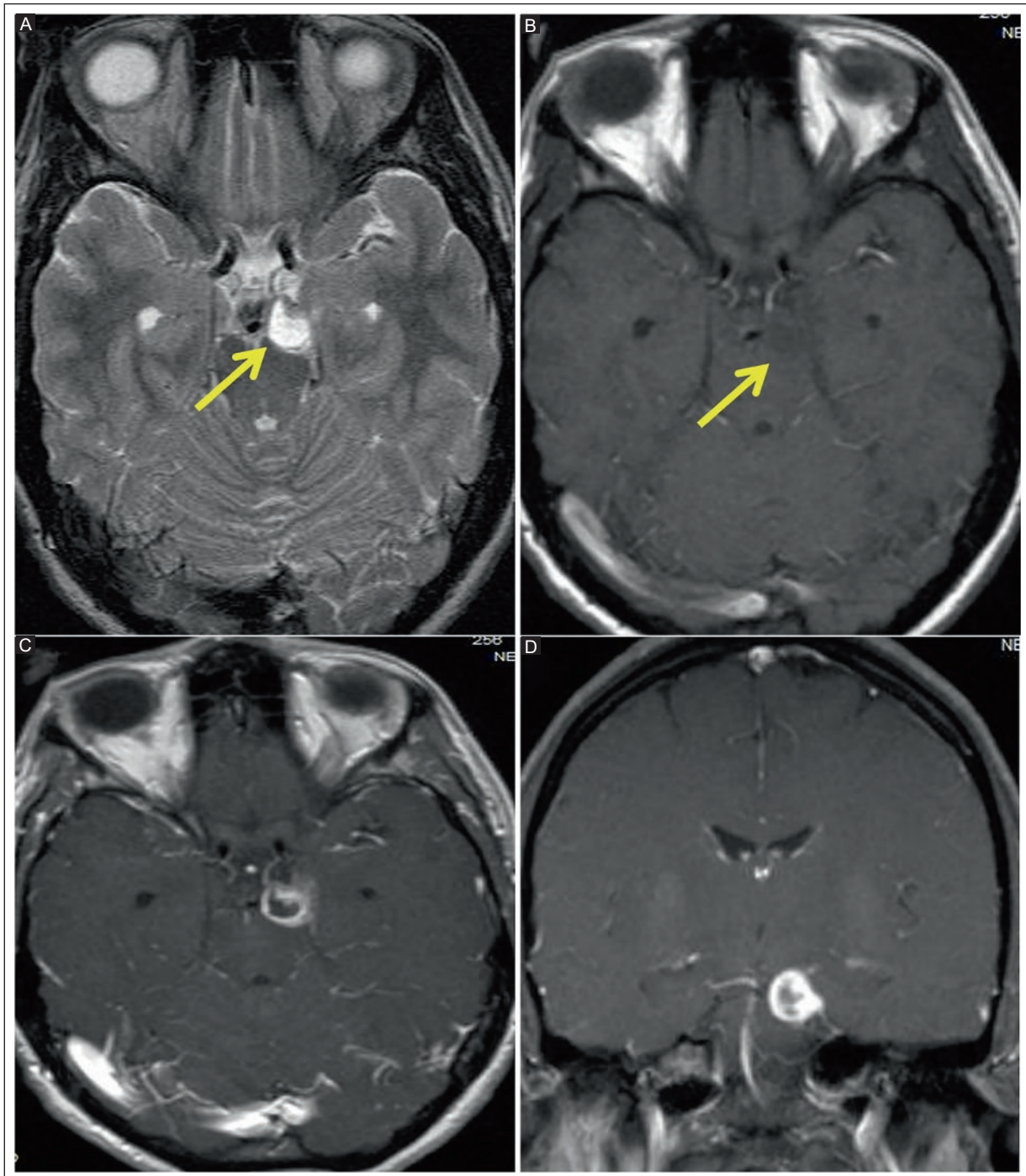


**Figure 8.** Trochlear schwannoma in a 36-year-old man with new onset left fourth cranial nerve palsy. **A:** MRI T2W axial. **B:** T1W axial views showing an extraaxial mass anterior to the left cerebral peduncle (arrows). **C-D:** MRI T1W axial and coronal views with Gad show heterogeneous peripheral enhancement of the mass.

Gad: gadolinium; MRI: magnetic resonance imaging.

### ***Congenital diplopia***

Congenital pathologies, usually associated with restrictive movement of the ocular motor muscles, show agenesis of the motor neurons in the brainstem.

Congenital fibrosis type 1, an autosomal dominant pathology which presents with ptosis and bilateral external ophthalmoplegia, is caused by agenesis of the superior division of the third cranial nerve. In most cases, the diagnosis is made clinically, with patients

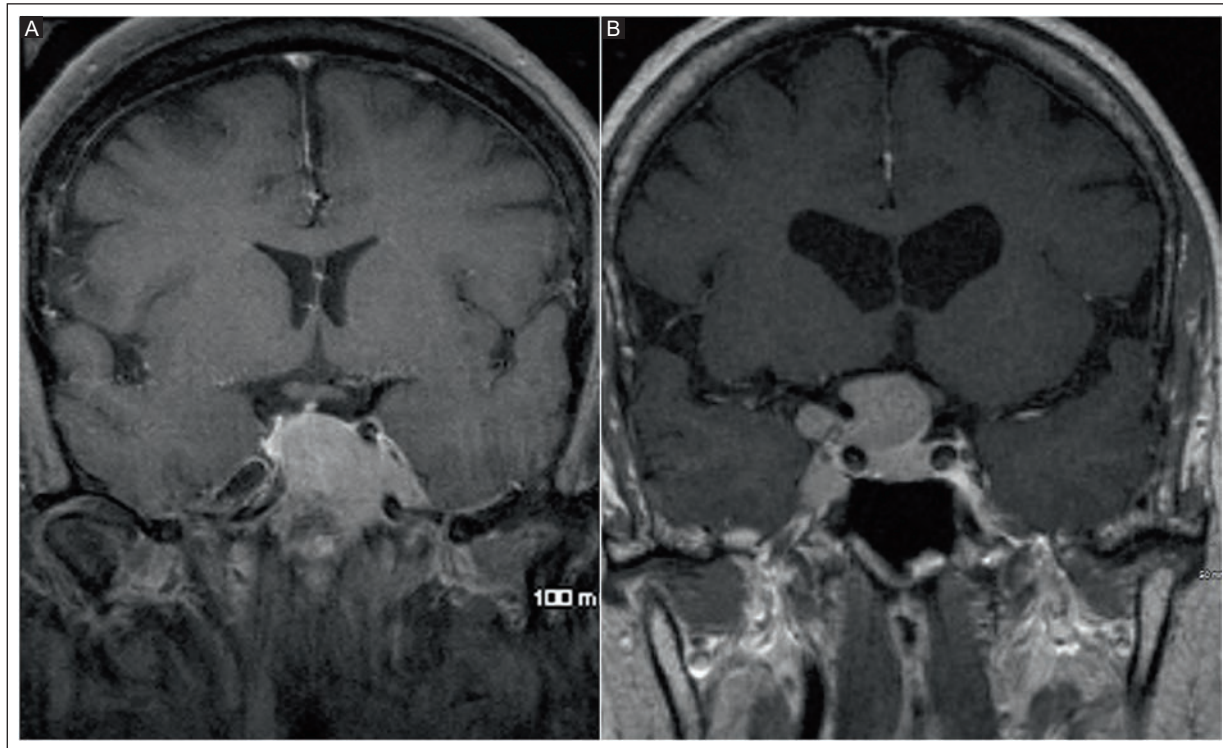


**Figure 9. A:** MRI T1W coronal post Gad view shows a large pituitary enhancing mass extending into the left cavernous sinus, consistent with a pituitary adenoma. **B:** MRI T1W post Gad coronal view of a different patient shows a sellar and suprasellar mass compressing the optic chiasm and extending into the right cavernous sinus, consistent with a meningioma.

MRI: magnetic resonance imaging; Gad: gadolinium.

showing a characteristic head tilt. Defects in the development of cranial nerve VI and its nucleus are known as Duane syndrome. In this syndrome, a branch of abnormal origin innervates the lateral rectus muscle, because it originates from the third cranial nerve. This abnormal innervation causes abnormal contractions of the lateral recti muscles<sup>10</sup>. Mobius syndrome corresponds to bilateral facial nerve palsy, often associated with sixth cranial nerve palsy. Several cranial nerve nuclei are either hypoplastic or absent in this syndrome. Craniofacial and limb deformities may also occur<sup>32</sup>.

### ***Iatrogenic diplopia***

Trauma to the extraocular muscles after cataract, retinal, orbital or sinus surgery can lead to diplopia. Approximately 0.17% to 0.85% of patients have diplopia after cataract extraction due to muscle restriction or paresis caused by trauma to the muscle cone during retroorbital anesthesia. Patients may present with hypotropia (54%) or hypertropia (44%) of the affected

eye. Other possible causes include unmasking of congenital phoria with resumption of binocular vision (34%), a prismatic effect by the implanted lens (4%) or concurrent presence of systemic disease (5%)<sup>4</sup>.

### ***Mimics***

Patients with strabismus or congenital ocular misalignment may present with exotropia, which can be misdiagnosed as cranial neuropathy. History and physical examination can help to differentiate between these two pathologies.

A history of eye correction, eye exercises in childhood or wearing glasses only in childhood are features that suggest a long-standing problem. Patients with strabismus usually develop suppression at a young age and do not show diplopia despite obvious eye misalignment<sup>12</sup>.

### **CONCLUSION**

The combination of clinical history, physical examination and imaging is crucial for an accurate diagnosis in

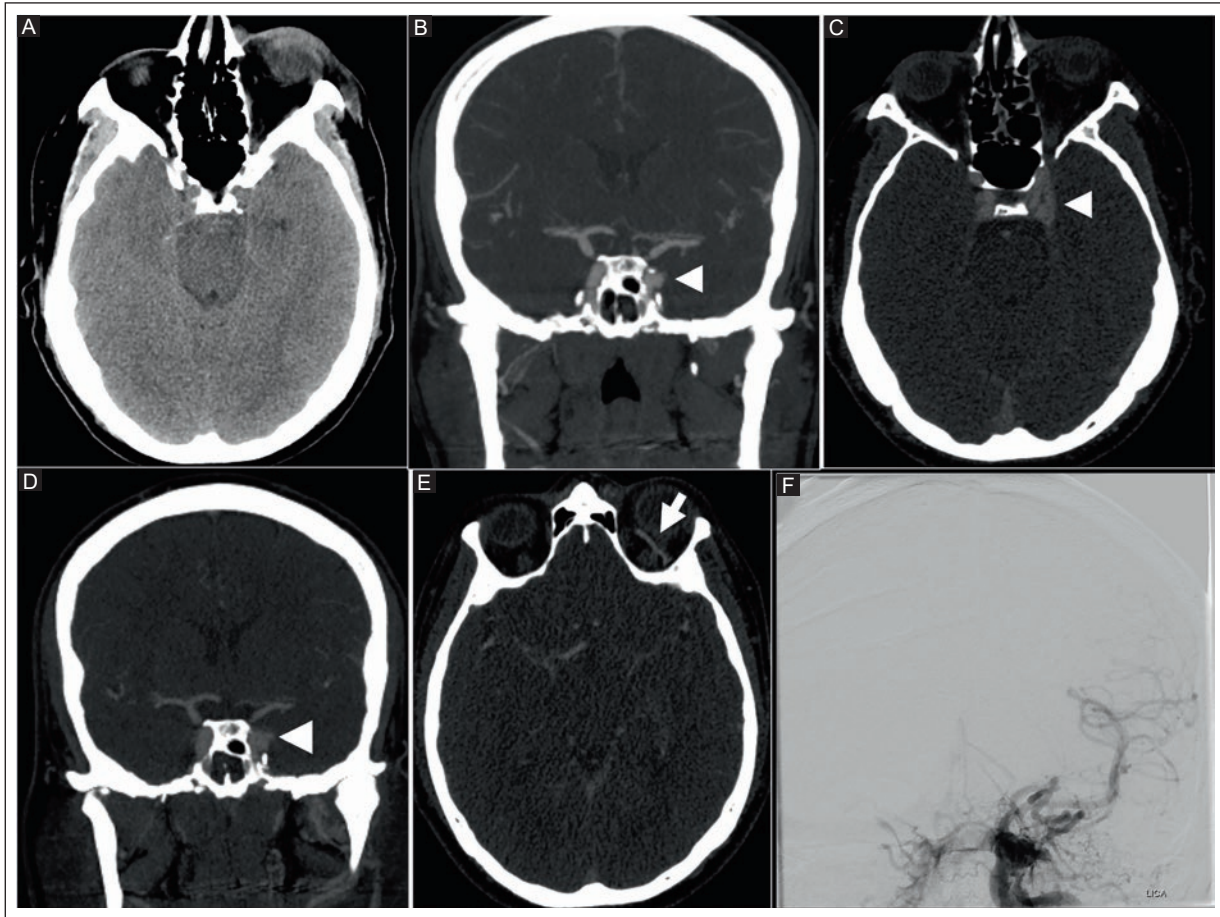


**Figure 10.** Carotid cavernous fistula in a 46-year-old woman with trauma to the left eye and diplopia. **A:** head CT axial view shows left-sided proptosis. **B:** CTA coronal view shows focal outpouching from the cavernous segment of the left ICA (arrowhead). **C-D:** CTA axial and coronal views, 3 days later show asymmetric opacification of the left cavernous sinus (arrowhead in C) and enlargement of the left ICA outpouching (arrowhead in D). **E:** associated enlargement of the superior ophthalmic vein (arrow). **F:** cerebral angiography shows venous shunting with early filling of the dilated left cavernous sinus through the fistula.

CT: computed tomography; CTA: computed tomography angiography; ICA: internal carotid artery.

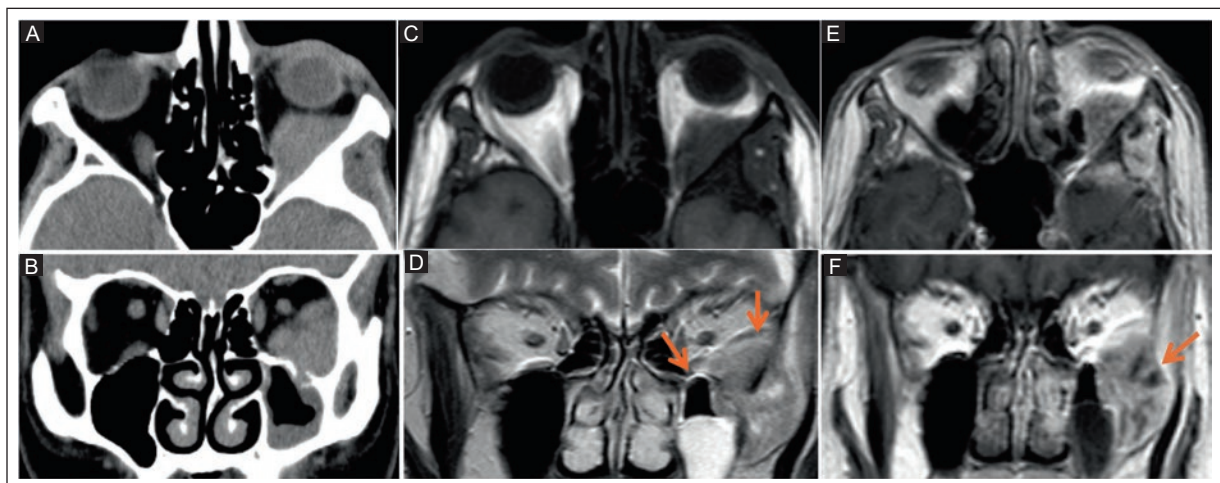


**Figure 11.** 68-year-old man with a history of bladder cancer and diplopia. **A-B:** CT axial and coronal views of the orbits show a soft tissue mass in the extraconal space of the left orbit. **C:** MRI T1W axial. **D:** MRI T2W coronal views show compression of the lateral and inferior recti muscles by the mass (arrows). **E-F:** The mass shows heterogeneous enhancement on axial and coronal T1W images post-Gad. Note the extension of the mass beyond the orbital wall and into the adjacent suprazygomatic masticator space (arrow).

CT: computed tomography; Gad: gadolinium; MRI: magnetic resonance imaging.

patients with binocular diplopia. Imaging of the brain and orbits allows assessment of the normal anatomy of cranial nerves III, IV and VI and is helpful in identifying and characterizing the various pathologies that may cause diplopia.

### Funding

Not applicable

### Conflicts of interest

The authors have no conflicts of interest to disclose.

### Ethical disclosures

**Protection of human and animal subjects.** The authors declare that no experiments were performed on humans or animals for this study.

**Confidentiality of data.** The authors declare that no patient data appear in this article. Furthermore, they have acknowledged and followed the recommendations as per the SAGER guidelines depending on the type and nature of the study.

**Right to privacy and informed consent.** The authors declare that no patient data appear in this article.

**Use of artificial intelligence.** The authors declare that they have not used any type of generative artificial intelligence for the writing of this manuscript, nor for the creation of images or their corresponding captions.

### REFERENCES

- Kirsch CFE, Black K. Diplopia: What to Double Check in Radiographic Imaging of Double Vision. *Radiol Clin North Am*. 2017;55 (1): 69-81. doi:10.1016/j.rcl.2016.08.008.
- Danchaivijitr C, Kennard C. Diplopia and eye movement disorders. *J Neurol Neurosurg Psychiatry*. 2004;75 Suppl 4(Suppl 4): iv24-31. doi: 10.1136/jnnp.2004.053413.
- Jain S. Diplopia: Diagnosis and management. *Clin Med (Lond)*. 2022;22 (2):104-106. doi:10.7861/clinmed.2022-0045.
- Dinkin M. Diagnostic approach to diplopia. *Continuum (Minneapolis)*. 2014;20(4):942-965. doi: 10.1212/01.CON.0000453310.52390.58.
- Kim JH, Kim M, Bae YJ. Magnetic Resonance Imaging in Diplopia: Neural Pathway, Imaging, and Clinical Correlation. *Korean J Radiol*. 2022;23(6):649-663. doi:10.3348/kjr.2022.0101.
- Adams ME, Linn J, Yousry I. Pathology of the Ocular Motor Nerves III, IV, and VI. *Neuroimaging Clin N Am*. 2008;18 (2):261-282. doi: 10.1016/j.nic.2007.11.001.
- Stalcup ST, Tuan AS, Hesselink JR. Intracranial causes of ophthalmoplegia: The visual reflex pathways. *Radiographics*. 2013;33 (5): E153-169. doi:10.1148/rg.335125142.
- Casselmann J, Mermuys K, Delanote J, Ghekiere J, Coenegrachts K. MRI of the Cranial Nerves—More than Meets the Eye: Technical Considerations and Advanced Anatomy. *Neuroimaging Clin N Am*. 2008;18 (2):197-231. doi: 10.1016/j.nic.2008.02.002.
- Smoker WRK, Reede DL. Denervation Atrophy of Motor Cranial Nerves. *Neuroimaging Clin N Am*. 2008;18 (2):387-411. doi: 10.1016/j.nic.2007.12.011.
- Koskas P, Héran F. Towards understanding ocular motility: III, IV and VI. *Diagn Interv Imaging* 2013;94 (10):1017-1031. doi: 10.1016/j.diii.2013.08.008.
- Touska P, Connor SEJ. New and Advanced Magnetic Resonance Imaging Diagnostic Imaging Techniques in the Evaluation of Cranial Nerves and the Skull Base. *Neuroimaging Clin N Am*. 2021;31 (4): 665-684. doi: 10.1016/j.nic.2021.06.006.
- Comblath WT. Diplopia due to ocular motor cranial neuropathies. *Continuum (Minneapolis)*. 2014;20(4):966-980. doi:10.1212/01.CON.0000453309.44766.b4.
- Maciag EJ, Martín-Noguerol T, Ortiz-Pérez S, Torres C, Luna A. Understanding Visual Disorders through Correlation of Clinical and Radiologic Findings. *Radiographics*. 2024;44(2): e230081. doi: 10.1148/rg.230081.
- Park KA, Min JH, Oh SY, Kim BJ. Idiopathic third and sixth cranial nerve neuritis. *Jpn J Ophthalmol*. 2019;63 (4):337-343. doi:10.1007/s10384-019-00666-7.
- Hsu CS, Closmann JJ, Baus MR. Idiopathic Unilateral Cranial Nerve VI Palsy: A Case Report and Review of the Literature. *J Oral Maxillofac Surg*. 2008;66(6):1282-1286. doi: 10.1016/j.joms.2007.04.035.
- Bodur M, Toker RT, Özmen AH, Okan MS. Facial colliculus syndrome due to a herpes simplex virus infection following herpes labialis. *Turk J Pediatr*. 2021;63(4):727-730. doi: 10.24953/turkped.2021.04.023.
- Sciaccia S, Lynch J, Davagnanam I, Barker R. Midbrain, pons, and medulla: Anatomy and syndromes. *Radiographics* 2019;39(4):1110-1125. doi: 10.1148/rg.2019180126.
- Alcubierre R, Sánchez-Dalmau BF, Muñoz S. Multiple sclerosis in ophthalmology: beyond optic neuritis. *Med Clin (Barc)*. 2020;155(2):70-76. English, Spanish. doi: 10.1016/j.medcli.2020.02.009.
- Jorquera Moya M, Merino Menéndez S, Porta Etessam J, Escibano Vera J, Yus Fuertes M. Cranial nerve disorders: clinical manifestations and topography. *Radiologia (Engl Ed)*. 2019;61(2):99-123. English, Spanish. doi: 10.1016/j.rx.2018.09.005.
- de Oliveira AM, Paulino MV, Vieira APF, McKinney AM, da Rocha AJ, Dos Santos GT, et al. Imaging patterns of toxic and metabolic brain disorders. *Radiographics*. 2019;39 (6):1672-1695. doi:10.1148/rg.2019190016.
- Medina-Flores R, Germanwala A, Molina JT, Meltzer CC, Wiley C a. October 2003: a 59-year-old woman with sudden onset of diplopia. Listerial rhombencephalitis. *Brain Pathol*. 2004;14(2):225-226. doi: 10.1111/j.1750-3639.2004.tb00100.x.
- Campos LG, Trindade RAR, Faistauer Â, Pérez JA, Vedolin LM, Duarte JÁ. Rhombencephalitis: pictorial essay. *Radiol Bras*. 2016; 49(5):329-336. doi: 10.1590/0100-3984.2015.0189.
- Lemos J, Eggenberger E. Neuro-Ophthalmological Emergencies. *Neurohospitalist*. 2015;5 (4):223-233. doi: 10.1177/1941874415583117.
- Palmieri GR, Sansone M, de Simone R, Moccia M. Monocular Diplopia in Idiopathic Intracranial Hypertension: A Case Report and Literature Review. *Eur J Case Rep Intern Med*. 2021;8(5):002509. doi: 10.12890/2021\_002509.
- Mark AS. Oculomotor motion disorders: Current imaging of cranial nerves 3, 4, and 6. *Semin Ultrasound CT MR*. 1998;19(3):240-256. doi: 10.1016/s0887-2171(98)90010-5.
- Douglas VP, Douglas KAA, Reinshagen KL, Chwalisz BK. Case 292: Lyme neuroborreliosis. *Radiology*. 2021; 300(2):484-488. doi: 10.1148/radiol.2021201715.
- Valand HA, Goyal A, Melendez DA, Matharu SS, Mangat HS, Tu RK. Lyme disease: What the neuroradiologist needs to know. *AJNR Am J Neuroradiol*. 2019;40(12):1998-2000. doi: 10.3174/ajnr.A6301.
- Hildenbrand P, Craven DE, Jones R, Nemeskal P. Lyme neuroborreliosis: Manifestations of a rapidly emerging zoonosis. *AJNR Am J Neuroradiol*. 2009;30(6):1079-1087. doi: 10.3174/ajnr.A1579.
- Kim SH, Lee KC, Kim SH. Cranial nerve palsies accompanying pituitary tumour. *J Clin Neurosci*. 2007;14(12):1158-1162. doi: 10.1016/j.jocn.2006.07.016.
- Peng TJ, Stretz C, Mageid R, Mac Grory B, Yaghi S, Matouk C, et al. Carotid-Cavernous Fistula Presenting with Bilateral Abducens Palsy. *Stroke*. 2020. 51(6):e107-e110. doi: 10.1161/STROKEAHA.120.029306.
- Boffano P, Roccia F, Gallesio C, Karagozoglu KH, Forouzanfar T. Diplopia and orbital wall fractures. *J Craniofac Surg*. 2014;25(2): e183-5. doi: 10.1097/SCS.0000000000000437.
- Eisenkraft B, Ortiz AO. Imaging evaluation of cranial nerves 3, 4, and 6. *Semin Ultrasound CT MR*. 2001;22(6):488-501. doi: 10.1016/s0887-2171(01)90003-4.

# Mammography breast density assessment with Quantra artificial intelligence software: intra- and interobserver agreement with radiologists

Beatriz E. Gonzalez-Ulloa\*<sup>1</sup>, Claudia B. Corona-Gonzalez<sup>2</sup>, Rosa L. Molina-Gutierrez<sup>3</sup>, and Sofia Salas-Aguirre<sup>4</sup>

Breast Imaging Department, Specialized Diagnostic Imaging Center, Zapopan, Jalisco, Mexico

## ABSTRACT

**Introduction.** A new version of Quantra v.2.2.2 artificial intelligence (AI) software is used for mammography breast density (MBD) assessment. This study aimed to determine the intraobserver agreement of radiologists (human readers, HRs) and the interobserver agreement between AI Quantra and HRs in MBD assessment. **Material and methods:** This prospective cohort study was conducted in two phases. HRs and AI Quantra version 2.2.2 assessed MBD in 2D mammograms and tomosynthesis in women over 35 years based on the BI-RADS 5th Edition. HRs had training in breast imaging with different levels of experience. MBD assessment between the first (phase 1) and second reading (phase 2) of the HRs was compared using four (a, b, c, d) and two MBD categories (a+b, non-dense, and c+d, dense). Intraobserver and interobserver agreement was assessed with light Kappa and Cohen's Kappa. **Results:** Four HRs with 2 to 32 years of experience interpreting breast images participated. They evaluated 685 mammograms in each phase. Intraobserver agreement between the two phases was moderate to substantial for the four MBD categories and substantial to near perfect for the two MBD categories. The interobserver agreement between AI Quantra and the four HRs varied from slight to moderate for the four MBD categories and moderate to substantial for the two categories. The interobserver agreement between AI and the four HRs improved in phase 2. **Conclusion:** Intraobserver agreement between radiologists and interobserver agreement between AI Quantra and HRs increased when assessing non-dense and dense MBD categories. Many factors can influence the visual assessment of MBD by radiologists, making AI a tool that can provide radiologists with additional information when assessing MBD.

**Keywords:** Mammography breast density. Artificial intelligence. Human readers. BI-RADS. Quantra software.

## INTRODUCTION

Increased breast density is a risk factor for breast cancer and reduces the sensitivity of mammography<sup>1-5</sup>. The diagnostic performance of mammography is limited with high breast density<sup>6-8</sup>. Mammography sensitivity decreases in breast cancer screening in dense breasts; therefore, complementary examinations such as ultrasound are indicated to reduce false-negative results<sup>4</sup>. Several visual methods based on the subjective perception of radiologists are used to assess

mammography breast density (MBD). The most common is BI-RADS, which has four categories (a, b, c, d). Categories a and b are classified as non-dense, and c and d as dense MBD<sup>9-14</sup>.

Artificial intelligence (AI) has been compared with radiologists (human readers) in assessing MBD,<sup>7,11,13,15-19</sup> and various AI software have been approved by the Food and Drug Administration (FDA)<sup>4</sup>. Several factors can influence the visual assessment of MBD. One of these is the reading of mammograms during a normal

### \*Corresponding author:

Beatriz E. Gonzalez-Ulloa  
E-mail: betyglez@yahoo.com

Received for publication: 06-09-2024

Accepted for publication: 27-09-2024

DOI: 10.24875/JMEXFRI.M24000088

Available online: 20-12-2024

J Mex Fed Radiol Imaging. 2024;3(4):221-230

www.JMeXFRI.com

2696-8444 / © 2024 Federación Mexicana de Radiología e Imagen, A.C. Published by Permanyer. This is an open access article under the CC BY-NC-ND (<https://creativecommons.org/licenses/by-nc-nd/4.0/>).



shift or at a time different from usual working hours, differences in the experience and age of radiologists, with young radiologists being more able to adapt to new technologies<sup>15</sup>. These factors require a standardized categorization of AI for MBD assessment.

AI Quantra™ is approved software evaluated in several clinical studies in two versions (v2.0 and v2.2.2)<sup>7,10,12-14,20</sup>. Quantra v.2.0 classifies the percentage of dense breast tissue observed on mammograms according to the BI-RADS 4th edition, while the current version (Quantra v.2.2.2)<sup>21</sup> quantifies the densest area based on BI-RADS 5th edition<sup>22,23</sup>. Few clinical studies have reported intra- and interobserver agreement of Quantra 2.2.2<sup>7,10,13</sup>. This study aimed to determine the intraobserver agreement of human readers (HRs) and the interobserver agreement between AI Quantra v2.2.2 and HRs in MBD assessment using BI-RADS 5th edition.

## **MATERIAL AND METHODS**

This prospective cohort study was conducted from May 2 to June 30, 2022, in the Breast Imaging Department of the Centro de Diagnostico Especializado por Imagen in Zapopan, Jalisco, Mexico. A convenience sample of radiologists with current certification by the Mexican Council of Radiology and Imaging and training in breast imaging were included. Informed consent was obtained from the participating radiologists.

### ***Study development and variables***

The sex and age of the radiologists and years of experience as radiologists performing breast imaging examinations were recorded. Screening or diagnostic mammograms of women aged 35 years or older were evaluated. Four MBD categories (a, b, c, d) and two MBD categories, a+b (non-dense) and c+d (dense), were assessed in all age groups and by age group, <40, 41 to 59, and 60 or older.

### ***Procedure for assessing intraobserver agreement***

MBD assessment between the first (phase 1) and second reading (phase 2) of the HRs was compared. MBD from both phases was also compared to a single Quantra AI assessment.

Two weeks after phase 1, each participant repeated this activity with the same images in a randomized order that differed from the first assessment. In the phase 2 assessment, the radiologists examined the

images individually and independently at times different from their normal work hours without knowing the results of their first assessment and the AI Quantra assessment. In the first phase, the HRs assessed breast density during normal working hours (morning or afternoon); in the second phase, the assessment was performed at a time (afternoon or morning) outside their working hours.

### ***Procedure for assessing interobserver agreement***

Interobserver agreement between AI Quantra and the four HRs was assessed independently in phase 1 and phase 2. Four and two MBD categories were evaluated.

### ***Protocol for image acquisition and analysis***

#### ***Digital mammography and digital breast tomosynthesis***

Images were acquired using Selenia Dimensions equipment (Hologic, Bedford, MA, USA) with automatic acquisition parameters. Images were stored and reviewed in the PACS system (SecureView, Diagnostic Workstation Bedford, MA, USA). Conventional projections were acquired: two craniocaudal (CC) and two lateral-medial-oblique (LMO) of both breasts. In patients with breast implants, images with breast displacements were evaluated. MBD was classified according to the 5th edition<sup>13</sup> of BI-RADS based on the densest area of fibroglandular tissue: category a, almost entirely fat; category b, scattered fibroglandular tissue; category c, heterogeneously dense; and category d, extremely dense<sup>22,23</sup>.

#### ***AI Quantra software***

Mammography images were analyzed with AI Quantra version 2.2.2 (Hologic Inc., Bedford, MA, USA). AI Quantra is based on the distribution and texture of the fibroglandular tissue pattern with an estimate of breast composition based on the distribution of dense tissue by choosing the densest category classified according to BI-RADS 5th edition<sup>22,23</sup>.

#### ***Statistical analysis***

Numerical variables are described with measures of central tendency and dispersion (standard deviation,

**Table 1.** Characteristics of radiologists (HRs) and number of mammograms assessed in phases 1 and 2

Reader	Sex	Years as certified radiologist	Years reading mammograms	Mammograms read per week	Hours reading per week	Mammograms Phase 1	Mammograms Phase 2
HR1	Woman	32	32	70-90	40-50	685	685
HR2	Woman	31	24	35-50	20-26	685	685
HR3	Woman	3	2	30-45	20-26	685	685
HR4	Woman	3	2	30-45	20-26	685	685

HRs: human readers.

SD), and categorical variables as absolute numbers and percentages. The agreement of a dichotomous categorical variable between 4 HRs observers was assessed with Cohen's kappa coefficient. The agreement of an ordinal variable between the 4 HRs was assessed with weighted kappa. Kappa agreement scores were interpreted using the following scale: slight = 0.00-0.20; fair = 0.21-0.40; moderate = 0.41-0.60; substantial = 0.61-0.80; almost perfect = 0.81-1.00. A  $p < 0.05$  was considered significant. The analysis was performed in SPSS version 28 (IBM Corp., Armonk, NY, USA).

## RESULTS

The characteristics of the four radiologists who participated in the study are shown in table 1. Years of experience interpreting breast images ranged from 2 to 32. The radiologists interpreted 30 to 90 mammograms per week and spent 20 to 50 hours performing various breast examinations and procedures (including mammography, ultrasound, magnetic resonance imaging, biopsies, and breast marking). A total of 685 mammograms were analyzed in each phase.

### *Comparison of the four MBD categories of AI Quantra and four HRs by age group in phase 1*

Figure 1A shows the classification of MBD into four categories in women of all age groups ( $n = 678$ ) by AI Quantra and four HRs. AI Quantra reported a higher number of mammograms in category a than the four HRs: AI ( $n = 59$ ) HR1 ( $n = 49$ ), HR2 ( $n = 35$ ), HR3 ( $n = 52$ ) and HR4 ( $n = 28$ ). AI ranked category b in a lower number of studies ( $n = 121$ ), while the range of four HRs varied (238 to 306 mammograms). Better agreement was observed in category c between AI ( $n = 298$ ) and the four HRs (range 299 to 335), while AI reported a higher number of mammograms ( $n = 200$ )

in category d than the four HRs (range 23 to 88). Figure 1B, the highest concordance between AI and four HRs was observed in categories a and c in women younger than 40 years ( $n = 24$ ). Only HR1 agreed with AI (10 and 12, respectively) in category d. HRs 2, 3, and 4 showed a variable range between 3 and 7 cases. Figure 1C, here was higher agreement between AI ( $n = 215$ ) and four HRs (range 235 to 262 mammograms) in category c in women aged 41 to 59 years ( $n = 477$ ). AI classified a larger number of studies ( $n = 28$  and  $n = 156$ , respectively) in categories a and d than the four HRs (range 12 to 21 in category a, and 20 to 70 in category d). Figure 1D, AI classified more mammograms in the two-categories ( $n = 73$  in category c, and  $n = 32$  in category d) in women 60 years or older ( $n = 177$ ) than the four HRs, who classified more women in category b (range 60 to 109).

Category d was more common than the other categories and the other age groups in women under 40. The number of women under 40 years with category b was low and gradually increased with age. In the group of women aged 60 and older, category a increased and category d decreased. Category c was prevalent in all 4 groups and showed the highest agreement between AI Quantra and the four HRs. The lowest agreement between AI Quantra and the four HRs was in the group of women aged 60 and older.

### *Comparison of the four-MBD categories by AI Quantra™ and the four HRs by age group in phase 2*

Figure 2A shows the classification of the four MBD categories by AI Quantra and four HRs in women of all age groups ( $n = 678$ ). Only HR3 showed agreement with AI ( $n = 61$  and  $n = 59$ , respectively) in category a. AI showed a lower number of mammograms ( $n = 121$ ) compared to four HRs (range 194 to 261) in category b. The highest agreement, similar to the first phase, was

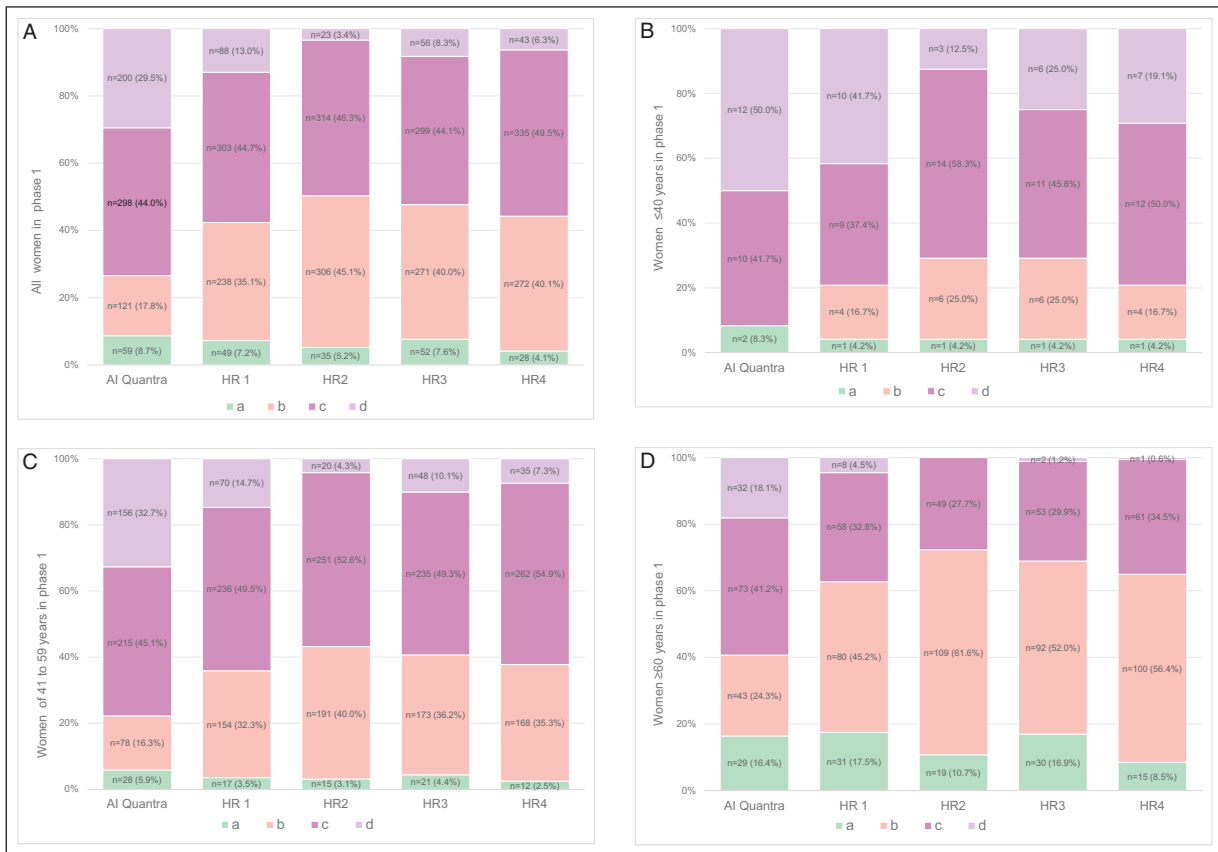


**Figure 1.** Comparison of the four MBD categories between AI Quantra and four HRs using BI-RADS 5th edition in phase 1. **A:** all women. **B:** women younger than 40 years. **C:** women between 41 and 59 years. **D:** women 60 years and older. Breast density was higher in the group of women younger than 40 years than in the other categories and the mean of all age groups. Category c was predominant in all groups and showed the highest agreement between AI Quantra and four HRs, while the lowest agreement between AI Quantra and four HRs was observed in women aged 60 years or older.

AI: artificial intelligence; BI-RADS: Breast Imaging Reporting and Data System; HRs: human readers; MBD: mammography breast density.

in category c, AI (n = 298) and the four HRs (range, 297 to 345). AI had a higher number of mammograms (n = 200) than the HRs (n = 59 to 125) in category d. Figure 2B, in women younger than 40 (n = 24), AI showed moderate agreement with the HRs in all four MBD categories. Figure 2C, among women aged 41 to 59 years (n = 477), there was agreement in category c between AI (n = 215) and four HRs (n = 229 to 255). AI classified a higher number of category a and d mammograms (28 and 156, respectively) than the HRs (category a from 13 to 24 and category d from 52 to 105). AI reported a lower number of mammograms than the HRs in category b. Figure 2D, for women aged 60 or older (n = 177), agreement was lower in the four MBD categories. AI scored 29 mammograms in category a and in HRs, they ranged from 11 to 36. AI scored 43 in category b and in HRs it ranged from 75 to 94. AI

classified 73 in category c and HRs 55 to 75. AI scored 32 in category d and HRs 0 to 11 mammograms.

In phase 2, the results were comparable to phase 1. The highest concordance between AI Quantra and four HRs was observed in category c in all age groups. In women younger than 40, breast density was higher than in the other categories than the mean of all age groups. Category c was predominant in all patients. Category b was low in patients under 40 and increased with increasing age. In the group of women aged 60 or older, category a increased and category d decreased. At this stage, the lowest agreement between AI Quantra and four HRs was observed in women aged 60 or older. Figure 3 shows images of agreement between AI Quantra and the four HRs of the four MBD categories, while figure 4 shows no agreement between AI Quantra and the four HRs in the four MBD categories.

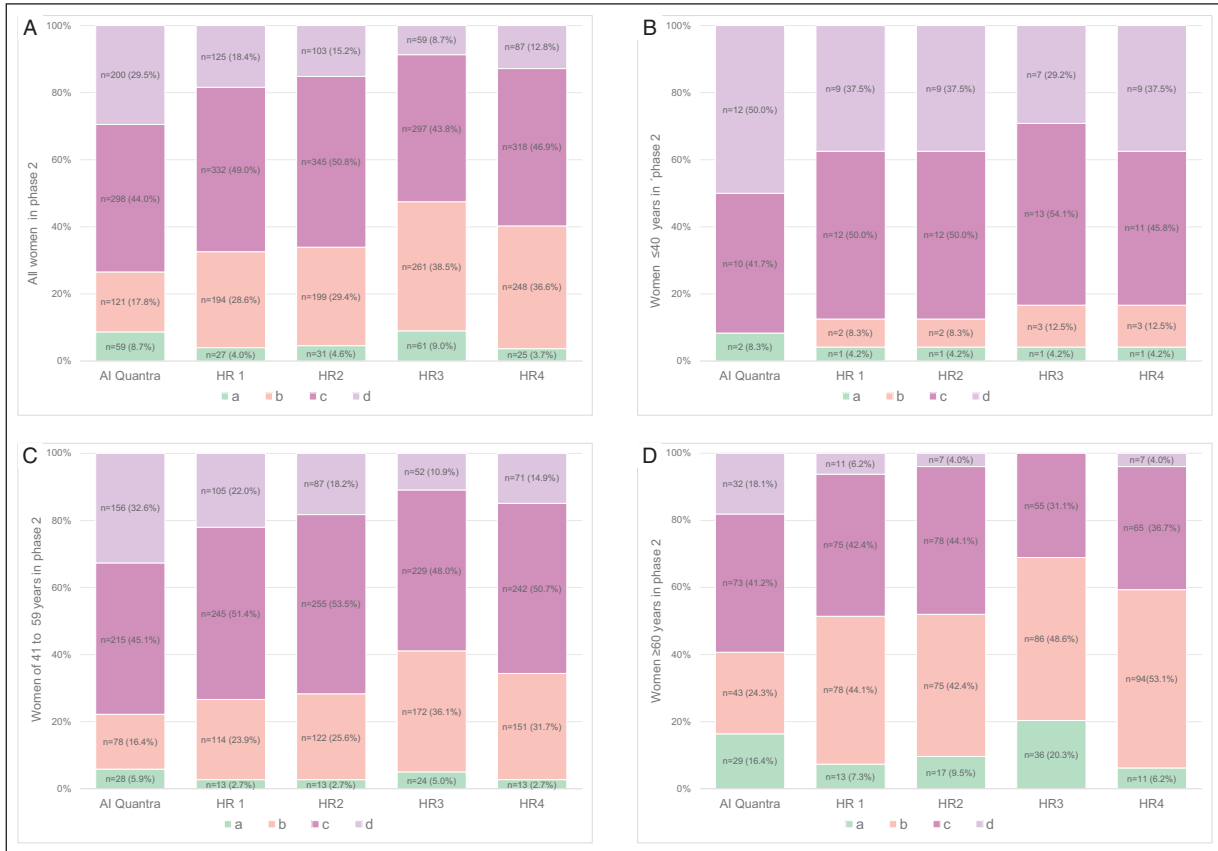


**Figure 2.** Comparison of the four-MBD categories between AI Quantra and four HRs using BI-RADS 5th edition in phase 2. **A:** all women. **B:** women under 40 years. **C:** women between 41 and 59 years. **D:** women 60 years and older. These results are comparable to those of phase 1. The highest agreement between AI Quantra and four HRs was observed in category c in all age groups.

AI: artificial intelligence; BI-RADS: Breast Imaging Reporting and Data System; HRs: human readers; MBD: mammography breast density.

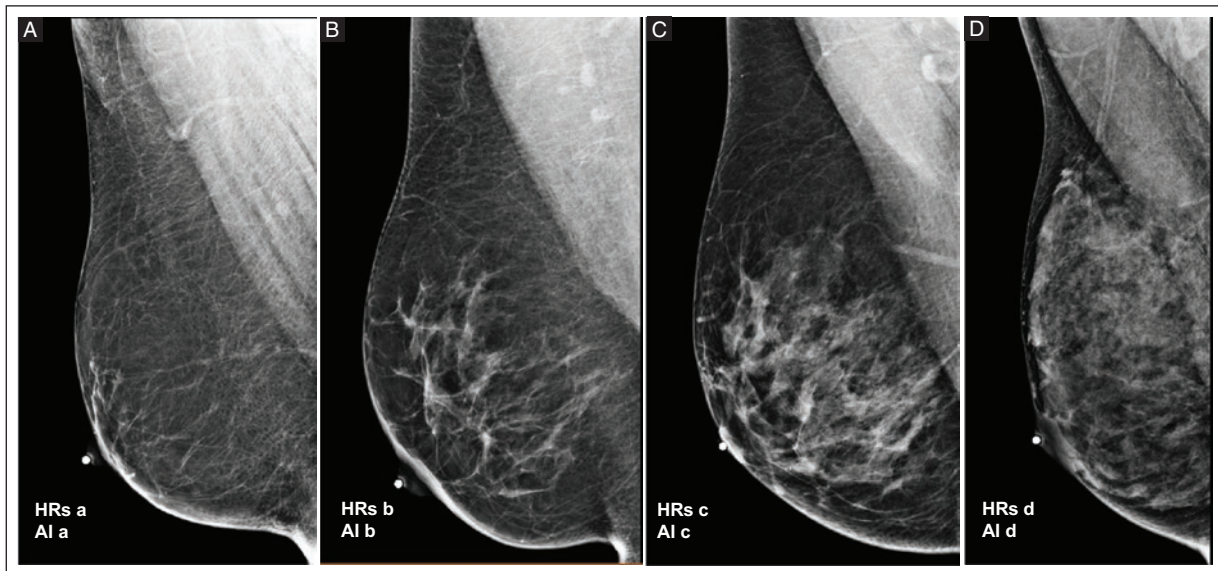


**Figure 3.** Mammography shows MBD classification between HRs and AI Quantra using 5th edition. **A, B, C,** and **D:** MLO views of the right breast, four HRs and AI agreed on four MBD categories.

AI: artificial intelligence; BI-RADS: Breast Imaging Reporting and Data System; MBD: mammography breast density; HRs: human readers; MLO: mediolateral oblique.

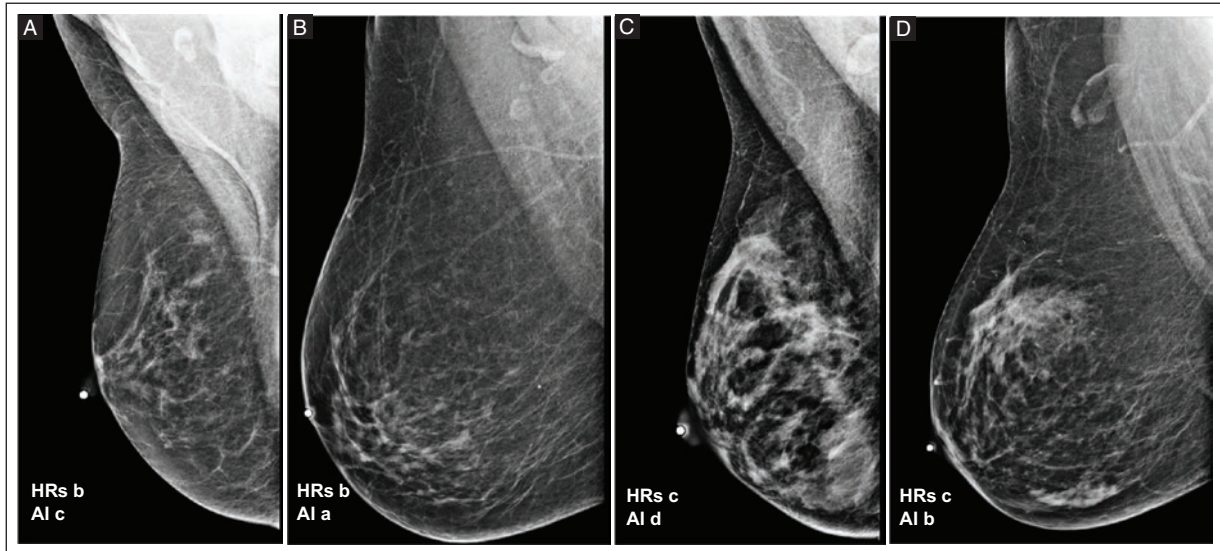


**Figure 4.** Comparison of MBD categories assessment between AI Quantra and HRs using BI-RADS 5th edition. **A, B, C, and D:** the MLO views show that AI Quantra and HRs MBD categories assessment do not match for the four MBD categories.

AI: artificial intelligence; BI-RADS: Breast Imaging Reporting and Data System; HRs: human readers; MBD: mammography breast density; MLO: mediolateral oblique.

### ***Intraobserver agreement of radiologists in the assessment of four and two MBD categories***

Agreement was substantial for HR1, HR3, and HR4 in the four MBD categories, while HR2 showed moderate agreement (Table 2). In the two MBD categories (non-dense and dense), agreement was almost perfect for HR4 and substantial for the other 3 HRs. For the four HRs, agreement was better for two-categories (non-dense and dense) with a significant difference ( $p < 0.001$ ).

### ***Interobserver agreement between AI Quantra and four HRs for the four MBD categories in phase 1 and phase 2***

In phase 1, HR1, with 32 years of breast imaging experience, showed the best agreement with AI Quantra, which was moderate in categories a, b, and d, and fair in category c (Table 3). HR3 and HR4 agreement was fair to moderate (fewer years of experience), while HR2 was slight to moderate (31 years).

Table 4 describes the interobserver agreement between Quantra AI and the four HRs in phase 2. HR2 agreement with AI was moderate in categories a, b, and d; category c was fair. The agreement of HRs 1 and 3 was fair and moderate (HRs with more and less experience), while it was slight for HR4. In phase 2, the interobserver agreement of HR2, HR3, and HR4

improved compared to phase 1, while HR1 decreased slightly. Interobserver agreement varied in both phases and ranged from slight to moderate, improving in three HRs in the second phase.

### ***Interobserver agreement between AI Quantra™ and four HRs comparing four MBD categories and two MBD categories***

In phase 1, the highest agreement between AI Quantra and HRs was for HR1 in four and two MBD categories ( $k = 0.50$  and  $0.56$ , respectively) (Table 5). HR3 and HR4 had the same agreement for four categories ( $k = 0.39$ ) and similar agreement for two MBD categories, while HR2 had the lowest agreement ( $k = 0.33$  and  $k = 0.45$ , respectively).

Phase 2 is shown in table 6. The highest agreement was between AI Quantra and HR1 and HR2 in the four MBD categories ( $k = 0.52$ ) and the two MBD categories for HR2 ( $k = 0.62$ ) followed by HR1 ( $k = 0.59$ ). The lowest agreement was for HR3 ( $k = 0.41$  and  $k = 0.47$ , respectively).

Agreement between AI and four HRs increased in phase 2 but was more marked with HR2. Interobserver agreement varied in both study phases, ranging from fair to moderate in four-MBD categories and moderate in the two MBD categories. Agreement was better in the two MBD categories (non-dense and dense) with a significant difference ( $p < 0.001$ ).

**Table 2.** Intraobserver agreement of radiologists in four and two MBD categories between phases 1 and 2

Reader	Four-MBD categories <sup>a</sup>		Two-MBD categories <sup>b</sup>	
	Weighted kappa (95% CI)	p	Light kappa (95% CI)	p
HR1	0.73 (0.69-0.77)	< 0.001	0.77 (0.72-0.82)	< 0.001
HR2	0.57 (0.53-0.62)	< 0.001	0.63 (0.58-0.69)	< 0.001
HR3	0.76 (0.72-0.80)	< 0.001	0.78 (0.73-0.83)	< 0.001
HR4	0.79 (0.75-0.82)	< 0.001	0.85 (0.81-0.89)	< 0.001

<sup>a</sup>Four MBD categories refer to a, b, c, d; <sup>b</sup>Two MBD categories refers to a+b and c+d (non-dense and dense, respectively).

HR: human reader; MBD: mammographic breast density.

**Table 3.** Interobserver agreement between AI Quantra and four HRs in phase 1 for four MBD categories<sup>a</sup>

	HR1 a	HR2 a	HR3 a	HR4 a
AI Quantra <b>a</b> , kappa	0.58	0.48	0.42	0.35
(95% CI)	(0.46-0.69)	(0.35-0.60)	(0.30-0.54)	(0.22-0.49)
Agreement	Moderate	Moderate	Moderate	Fair
	HR1 b	HR2 b	HR3 b	HR4 b
AI Quantra <b>b</b> , kappa	0.43	0.34	0.34	0.36
95% CI	-0 (0.36-0.50)	(0.28-0.40)	(0.28-0.41)	(0.30-0.43)
Agreement	Moderate	Fair	Fair	Fair
	HR1 c	HR2 c	HR3 c	HR4 c
AI Quantra <b>c</b> , kappa	0.35	0.11	0.24	0.26
95% CI	(0.28-0.42)	(0.04-0.19)	(0.16-0.31)	(0.19-0.33)
Agreement	Fair	Slight	Fair	Fair
	HR1 d	HR2 d	HR3 d	HR4 d
AI Quantra <b>d</b> , kappa	0.41	0.10	0.27	0.21
95% CI	(0.34-0.49)	(0.05-0.15)	(0.20-0.34)	(0.15-0.28)
Agreement	Moderate	Slight	Fair	Fair

HRs: human readers; AI: artificial intelligence; BI-RADS: Breast Imaging Reporting and Data System; CI: confidence interval; MBD: mammographic breast density; <sup>a</sup>MBD categories: category a, almost entirely fat; category b, scattered fibroglandular tissue; category c, heterogeneously dense; and category d, extremely dense. All values are p < 0.001.

## DISCUSSION

In our study, intraobserver agreement between the four HRs was moderate to substantial in the four MBD categories and substantial to almost perfect in the two-MBD categories (non-dense and dense). The interobserver agreement between AI Quantra and four HRs varied from slight to moderate in the four MBD

categories, while it was moderate to substantial in the two MBD categories (non-dense and dense). We believe that AI Quantra can add value to MBD interpretation by improving the qualitative assessment of HRs.

Substantial intraobserver agreement has been reported for the four MBD categories and almost perfect agreement for the two MBD categories with BI-RADS 4th edition<sup>24,20</sup>. In the study by Epko et al.<sup>10</sup>

**Table 4.** Interobserver agreement between AI Quantra and four HRs in phase 2 for four-MBD categories<sup>a</sup>

	HR1 a	HR2 a	HR3 a	HR4 a
AI Quantra <b>a</b> , <i>kappa</i>	0.38	0.43	0.54	0.32
(95% CI)	0.25-0.52	0.30-0.56	0.43-0.65	0.19-0.46
Agreement	Fair	Moderate	Moderate	Fair
	HR1 b	HR2 b	HR3 b	HR4 b
AI Quantra <b>b</b> , <i>kappa</i>	0.39	0.45	0.34	0.38
95% CI	0.32-0.47	0.37-0.52	0.28-0.41	0.31-0.45
Agreement	Fair	Moderate	Moderate	Fair
	HR1 c	HR2 c	HR3 c	HR4 c
AI Quantra <b>c</b> , <i>kappa</i>	0.41	0.40	0.26	0.38
95% CI	0.35-0.48	0.33-0.33	0.19-0.33	0.31-0.45
Agreement	Moderate	Fair	Fair	Fair
	HR1 d	HR2 d	HR3 d	HR4 d
AI Quantra <b>d</b> , <i>kappa</i>	0.49	0.43	0.27	0.41
95% CI	0.41-0.56	0.36-0.51	0.20-0.35	0.34-0.48
Agreement	Moderate	Moderate	Fair	Moderate

All values are  $p < 0.001$ . <sup>a</sup>MBD categories: Category a, almost entirely fat; Category b, scattered fibroglandular tissue; Category c, heterogeneously dense; Category d, extremely dense.

AI: artificial intelligence; BI-RADS: Breast Imaging Reporting and Data System; CI: confidence interval; MBD: mammographic breast density; HRs: human readers.

**Table 5.** Interobserver agreement between AI Quantra and four HRs with four and two MBD categories in phase 1

Description	Four-MBD categories <sup>a</sup>		Two-MBD categories <sup>b</sup>	
	Weighted kappa (95% CI)	p	Light kappa (95% CI)	p
AI Quantra vs. HR1	0.50 (0.46-0.55)	< 0.001	0.56 (0.50-0.62)	< 0.001
AI Quantra vs. HR2	0.33 (0.29-0.38)	< 0.001	0.45 (0.39-0.51)	< 0.001
AI Quantra vs. HR3	0.39 (0.34-0.44)	< 0.001	0.47 (0.41-0.53)	< 0.001
AI Quantra vs. HR4	0.39 (0.34-0.43)	< 0.001	0.52 (0.46-0.58)	< 0.001

<sup>a</sup>Four-MBD categories refer to a, b, c, d; <sup>b</sup>Two-MBD categories refer to a+b and c+d (non-dense and dense, respectively).

AI: artificial intelligence; BI-RADS: Breast Imaging Reporting and Data System; CI: Confidence Interval; HRs: human reader; MBD: mammographic breast density.

**Table 6.** Interobserver agreement between AI Quantra and four HRs with four or two MBD categories in phase 2

Description	Four categories <sup>a</sup>		Two categories <sup>b</sup>	
	Weighted kappa (95% CI)	p	Light kappa (95% CI)	p
AI Quantra vs. HR1	0.52 (0.47-0.57)	< 0.001	0.59 (0.53-0.66)	< 0.001
AI Quantra vs. HR2	0.52 (0.47-0.57)	< 0.001	0.62 (0.56-0.69)	< 0.001
AI Quantra vs. HR3	0.41 (0.36-0.46)	< 0.001	0.47 (0.41-0.53)	< 0.001
AI Quantra vs. HR4	0.47 (0.42-0.51)	< 0.001	0.55 (0.49-0.62)	< 0.001

<sup>a</sup>Four-MBD categories refer to a, b, c, d; <sup>b</sup>Two-MBD categories refer to a+b and c+d (non-dense and dense, respectively).

AI: artificial intelligence; BI-RADS: Breast Imaging Reporting and Data System; CI: Confidence Interval; HRs: human readers; MBD: mammographic breast density.

using an older version of Quantra (v.2.0) and BI-RADS 4th edition in two phases, intraobserver agreement was assessed by 6 breast radiologists with 3 to 25 years of experience. The researchers grouped mammogram reader data into four and two MBD categories. Phase 2 was conducted 5 months after phase 1, in which three radiologists participated. A majority report was generated with the consensus of 2 radiologists. There were 1314 cases in phase 1 and 292 cases in phase 2. There was substantial to almost perfect intraobserver agreement of individual radiologists and the majority report for four MBD categories ( $k = 0.80$  to  $k = 0.89$ ), and almost perfect agreement for two MBD categories ( $k = 0.82$  to  $k = 0.90$ ). This study had results comparable to ours in intraobserver agreement between radiologists. Intraobserver agreement in our study with BI-RADS 5th edition between HRs was moderate to substantial for the four MBD categories and improved for two MBD categories with substantial to almost perfect agreement. HR4, a young radiologist with less experience, had an almost perfect intraobserver agreement. Radiologists achieved better performance and intraobserver agreement when assessing two MBD categories (non-dense and dense) than four. This could be because the human eye can easily distinguish higher density from lower density.

Studies on interobserver agreement between AI Quantra and radiologists in MBD assessment using different versions of the software and BI-RADS 4th or 5th edition have reported different results<sup>7,11-14</sup>. Tari et al.<sup>13</sup> evaluated the interobserver agreement of three radiologists with 10 to 25 years of experience on 1314 mammograms with the current version of AI Quantra with a central projection image at tomosynthesis. Consensus was reached in cases with discrepancies. Interobserver agreement was moderate to almost perfect in the two MBD categories. These results are comparable to our study using the current version of Quantra (v.2.2.2)<sup>21</sup> and BI-RADS 5th edition. Interobserver agreement between AI Quantra and four HRs was moderate for four MBD categories and moderate to substantial for two MBD categories. There was greater agreement between AI and HR1, the radiologist with more years of experience. Epko et al.<sup>10</sup> found substantial interobserver agreement in four MBD categories and almost perfect agreement in two MBD categories in their two-phase study. AI Quantra was very good at reproducing the BI-RADS classification in the two MBD categories and can be recommended as a complement for MBD assessment in clinical practice.

The prospective design, sufficient sample size to determine intraobserver and interobserver agreement, and the participation of four radiologists with different levels of experience are the strengths of this study. On the other hand, there are some limitations. First, this is a single-institution study. Second, all mammograms were acquired by a single mammography unit. Third, only Quantra software was available at our institution, and fourth, it was performed by four radiologists in the same workplace.

## CONCLUSION

In our study, intraobserver agreement improved using two MBD categories (non-dense and dense). The Interobserver agreement of the MBD classification in our study between AI Quantra and four HRs varied from slight to moderate. AI is a diagnostic tool that complements the radiologist's MBD assessment regardless of their experience. More experienced radiologists can use AI to reduce reading time for interpretation and to decide who requires a complementary imaging examination to replace one of the readers in a double assessment, or to select mammograms from different risk groups and prioritize them. Less experienced radiologists can use AI as a comparative criterion to decide whether to perform an additional breast imaging examination. Prospective studies with a large population are needed to assess the accuracy of AI in MBD assessment.

## Acknowledgments

The authors thank Professor Ana M. Contreras-Navarro for her guidance in preparing and writing this scientific paper.

## Funding

This research received no external funding.

## Conflicts of interest

The authors declare that they have no conflicts of interest.

## Ethical disclosures

**Protection of individuals.** This study was conducted in compliance with the Declaration of Helsinki (1964) and its subsequent amendments.



**Confidentiality of data.** The authors declare they followed their center's protocol for sharing patient data.








**Right to privacy and informed consent.** Informed consent was not required for this observational study of information collected during routine clinical care.

**Use of artificial intelligence.** The authors did not use generative artificial intelligence to prepare this manuscript and/or create tables, figures, or figure legends.

## REFERENCES

- Carney PA, Miglioretti DL, Yankaskas BC, Kerlikowske K, Rosenberg R, Rutter CM, et al. Individual and combined effects of age, breast density, and hormone replacement therapy use on the accuracy of screening mammography. *Ann Intern Med.* 2003;138(3):168-175. doi: 10.7326/0003-4819-138-3-200302040-00008. Erratum in: *Ann Intern Med.* 2003;138(9):771.
- McCormack VA, dos Santos Silva I. Breast density and parenchymal patterns as markers of breast cancer risk: a meta-analysis. *Cancer Epidemiol Biomarkers Prev.* 2006;15(6):1159-1169. doi: 10.1158/1055-9965.
- Kim E, Lewin AA. Breast Density: Where Are We Now? *Radiol Clin North Am.* 2024;62(4):593-605. doi: 10.1016/j.rcl.2023.12.007.
- Taylor CR, Monga N, Johnson C, Hawley JR, Patel M. Artificial Intelligence Applications in Breast Imaging: Current Status and Future Directions. *Diagnostics (Basel).* 2023;13(12):2041. doi: 10.3390/diagnostics13122041.
- Edmonds CE, O'Brien SR, Conant EF. Mammographic Breast Density: Current Assessment Methods, Clinical Implications, and Future Directions. *Semin Ultrasound CT MR.* 2023;44(1):35-45. doi: 10.1053/j.sult.2022.11.001.
- Winkler NS, Raza S, Mackesy M, Birdwell RL. Breast density: clinical implications and assessment methods. *Radiographics.* 2015;35(2):316-324. doi: 10.1148/rg.352140134.
- Rahmat K, Ab Mumin N, Ramli Hamid MT, Fadzli F, Ng WL, Muhammad Gowdh NF. Evaluation of automated volumetric breast density software in comparison with visual assessments in an Asian population: A retrospective observational study. *Medicine (Baltimore).* 2020;99(39):e22405. doi: 10.1097/MD.00000000000022405.
- Lehman CD, Yala A, Schuster T, Dontchos B, Bahl M, Swanson K, et al. Mammographic Breast Density Assessment Using Deep Learning: Clinical Implementation. *Radiology.* 2019;290(1):52-58. doi: 10.1148/radiol.2018180694.
- Damases CN, Hogg P, McEntee MF. Intercountry analysis of breast density classification using visual grading. *Br J Radiol.* 2017;90(1076):20170064. doi:10.1259/bjr.20170064.
- Ekpo EU, McEntee MF, Rickard M, Brennan PC, Kunduri J, Demchig D, et al. Quantra™ should be considered a tool for two-grade scale mammographic breast density classification. *Br J Radiol.* 2016;89(1060):20151057. doi: 10.1259/bjr.20151057.
- Ciatto S, Houssami N, Apruzzese A, Bassetti E, Brancato B, Carozzi F, et al. Categorizing breast mammographic density: intra- and interobserver reproducibility of BI-RADS density categories. *Breast.* 2005;14(4):269-275. doi: 10.1016/j.breast.2004.12.004.
- Morrish OW, Tucker L, Black R, Willsher P, Duffy SW, Gilbert FJ. Mammographic breast density: comparison of methods for quantitative evaluation. *Radiology.* 2015;275(2):356-365. doi: 10.1148/radiol.14141508.
- Tari DU, Santonastaso R, De Lucia DR, Santarsiere M, Pinto F. Breast Density Evaluation According to BI-RADS 5th Edition on Digital Breast Tomosynthesis: AI Automated Assessment Versus Human Visual Assessment. *J Pers Med.* 2023;13(4):609. doi: 10.3390/jpm13040609.
- Yeo I, Akwo J, Ekpo E. Automated mammographic density measurement using Quantra™: comparison with the Royal Australian and New Zealand College of Radiology synoptic scale. *J Med Imaging (Bellingham).* 2020;7(3):035501. doi: 10.1117/1.JMI.7.3.035501.
- Delsol-Perez C, Reyes-Mosqueda A, Rios-Rodriguez T, Perez-Montemayor D. Interobserver agreement between radiologists and artificial intelligence in mammographic breast density classification. *J Mex Fed Radiol Imaging.* 2024;3(2):122-127. doi: 10.24875/JMEXFRI.M24000074.
- Sartor H, Lång K, Rosso A, Borgquist S, Zackrisson S, Timberg P. Measuring mammographic density: comparing a fully automated volumetric assessment versus European radiologists' qualitative classification. *Eur Radiol.* 2016;26(12):4354-4360. doi: 10.1007/s00330-016-4309-3.
- Kusumaningtyas N, Supit N, Murtala B, Muis M, Chandra M, Sanjaya E, et al. A systematic review and meta-analysis of correlation of automated breast density measurement. *Radiography (Lond).* 2024;30(5):1455-1467. doi: 10.1016/j.radi.2024.08.003.
- Larsen M, Aglen CF, Lee CI, Hoff SR, Lund-Hanssen H, Lång K, et al. Artificial Intelligence Evaluation of 122 969 Mammography Examinations from a Population-based Screening Program. *Radiology.* 2022;303(3):502-511. doi: 10.1148/radiol.212381.
- Larsen M, Olstad CF, Lee CI, Hovda T, Hoff S, Marinussen M. Performance of an AI System for Breast Cancer Detection on Screening Mammograms from Breast Screen Norway. *Radiology: Artif Intell.* 2024;6(3):e230375. doi:10.1148/rya.230375.
- Ciatto S, Bernardi D, Calabrese M, Durando M, Gentilini MA, Mariscotti G, et al. A first evaluation of breast radiological density assessment by QUANTRA software as compared to visual classification. *Breast.* 2012;21(4):503-506. doi: 10.1016/j.breast.2012.01.005.
- Hologic Inc. Understanding quantra 2.2 user guide for cenova 3.0.1 English Man 05503-302 rev 002. Hologic; Bedford, MA, USA: 2019. <https://www.hologic.com>.
- D'Orsi C, Sickles EA, Mendelson EB, Morris EA. Breast Imaging Reporting and Data System: ACR BI-RADS breast imaging atlas. 5th Edition. Reston: American College of Radiology. 2013.
- American College of Radiology. ACR BI-RADS Atlas: Breast Imaging Reporting and Data System. 5th. Reston, VA: American College of Radiology; 2013. ACR BI-RADS® - Mammography.
- Redondo A, Comas M, Macià F, Ferrer F, Murta-Nascimento C, Maristany MT, et al. Inter- and intraradiologist variability in the BI-RADS assessment and breast density categories for screening mammograms. *Br J Radiol.* 2012;85(1019):1465-1470. doi: 10.1259/bjr/21256379.
- Lee SE, Yoon JH, Son NH, Han K, Moon HJ. Screening in Patients with Dense Breasts: Comparison of Mammography, Artificial Intelligence, and Supplementary Ultrasound. *AJR Am J Roentgenol.* 2024;222(1):1-12. doi:10.2214/AJR.23.29655.

# Multimodality imaging of hematologic malignancies affecting the breast: a pictorial essay

Natalia Guerrero-Fajardo<sup>1</sup>, Mane M. Ayala-Duran<sup>1</sup>, Yesika Davila-Zablah<sup>1\*</sup>,  
Nancy L. Garza-Garcia<sup>1</sup>, Gabriela S. Gomez-Macias<sup>2</sup>, Daniel F. Lopez-Altamirano<sup>2</sup>,  
and Margarita L. Garza-Montemayor<sup>1</sup>

<sup>1</sup>Diagnostic Breast Imaging Center, Hospital Zambrano Hellion, Tec Salud; <sup>2</sup>Pathology Department, Hospital San Jose, Tec Salud. Monterrey, Nuevo Leon, Mexico

## ABSTRACT

Hematologic malignancies affecting the breast are a heterogeneous group that includes lymphomas, leukemias, and multiple myeloma. Secondary infiltration by lymphoma is the most common hematologic malignancy of the breast. This pictorial essay presents clinical cases of mammography, ultrasound, and magnetic resonance imaging (MRI) findings of lymphoma, leukemia, and multiple myeloma, with histopathologic confirmation. The most common imaging findings were mass(es), non-mass lesions, or architectural distortion, and less commonly, diffusely increased breast density. There are no specific criteria for image diagnosis of hematologic malignancies affecting the breast; therefore, it is essential to know the medical history. Although a biopsy is always necessary, knowledge of the imaging findings gives the radiologist the necessary tools to diagnose correctly.

**Keywords:** Ultrasound. Mammography. Magnetic resonance imaging. Breast. Hematologic malignancies.

## INTRODUCTION

Hematologic malignancies affecting the breast are a heterogeneous group that includes different types of lymphomas, leukemias, and multiple myeloma. They comprise approximately 0.04-0.5% of all breast malignancies<sup>1</sup>. The manifestations in the breast are variable and may mimic a primary breast tumor. A history of hematologic malignancy should raise suspicion of a secondary breast lesion<sup>2</sup>. There are no specific diagnostic imaging features. Diagnosis should always be made with a pathologic examination of the suspicious lesion. This pictorial essay describes the main

ultrasound, mammography, and magnetic resonance imaging (MRI) features of hematologic malignancies with infiltration of the breast and provides diagnostic pearls that should be considered in the differential diagnosis in the appropriate clinical context.

## LYMPHOMAS

Lymphoma can affect the breast as a primary tumor or an extranodal manifestation<sup>2,3</sup>. Secondary infiltration by lymphoma is the most common hematologic malignancy of the breast<sup>1-3</sup>. Unilateral primary breast lymphomas affect older women and often have

### \*Corresponding author:

Yesika J. Davila-Zablah  
E-mail: yesikadavila@gmail.com

Received for publication: 11-09-2024

Accepted for publication: 30-09-2024

DOI: 10.24875/JMEXFRI.M24000087

Available online: 20-12-2024

J Mex Fed Radiol Imaging. 2024;3(4):231-242

www.JMeXFRI.com

2696-8444 / © 2024 Federación Mexicana de Radiología e Imagen, A.C. Published by Permanyer. This is an open access article under the CC BY-NC-ND (<https://creativecommons.org/licenses/by-nc-nd/4.0/>).

B-cell histology, whereas bilateral primary lymphomas usually affect young women and are associated with Burkitt lymphoma.

Primary breast lymphomas represent 0.85-2.2% of lymphomas and 0.1-0.5% of all primary breast neoplasms<sup>2,3</sup>. This low percentage is due to the small amount of intramammary lymphoid tissue. Lymphoma is considered primary if no extramammary lymphoma or disseminated disease has been previously diagnosed<sup>4</sup>.

Secondary breast lymphoma is the most common metastatic lesion affecting the breast, with a mean age at diagnosis of 55-65 years<sup>2</sup> and a variable prevalence of 0.07% to 17%. Secondary disease has earlier signs of nodal disease and most commonly affects the breast in patients with diffuse non-Hodgkin lymphoma<sup>5</sup>. The presence of unilateral or bilateral breast masses, and trabecular or cutaneous thickening, with or without axillary adenopathy, suggests a secondary breast lymphoma in a patient with a known diagnosis of lymphoma<sup>4-6</sup>.

The most common clinical manifestation is a palpable, painless mass (61%) in the upper outer quadrant, with palpable lymph nodes (40%) and pain (25%). There may be nipple retraction, telorrrhea, and local signs of inflammation such as diffuse skin thickening and edema<sup>3,4</sup>. In some cases, it may be an incidental finding (12%) in asymptomatic patients<sup>7</sup>. B-symptoms (fever, sweating, and weight loss) are rare in primary breast lymphomas but common in secondary forms. No specific features or signs on breast imaging accurately differentiate primary and secondary lymphoma. A solitary mass with or without axillary adenopathy and a larger size can lead to the diagnosis of primary lymphoma<sup>6</sup>.

### **Mammography**

Lymphoma most commonly manifests as a mass (76%)<sup>4</sup>, asymmetry, or architectural distortion of the breast. Masses may be oval, round, irregular, hyper, or isodense, with circumscribed or indistinct margins. Asymmetries occur in 20% of cases, and architectural distortion in 9%. Cutaneous edema (lymphedema) is observed in 8%. Calcifications are rare and abnormal lymph nodes can be observed in up to 28% of cases<sup>2,4,8</sup>.

### **Ultrasound**

The most common finding is a solid mass. Its shape is variable, with circumscribed or indistinct margins, hypoechoic or mixed echogenicity, usually with increased

vascularity and a peripheral echogenic halo<sup>4</sup>. In both cases, axillary adenopathies may be observed in primary or secondary lymphoma. Palpable abnormal lymph nodes as an initial finding may suggest a diagnosis of secondary lymphoma<sup>3</sup>.

### **MRI**

As with mammography and ultrasound, the most common manifestation is an enhanced oval, or round, isointense mass in T1 with variable intensity in T2. Enhancement is variable, homogeneous, or heterogeneous. Diffuse infiltration of the breast has also been documented. Axillary and occasionally mediastinal adenopathy can be observed<sup>4,6</sup>.

### **Case 1. Hodgkin lymphoma**

A 63-year-old woman presented palpable abnormal lymph nodes in the right axilla. Mammography showed increased diffuse density of the right breast (global asymmetry) (Figure 1). Hyperdense round lymph nodes were identified in the right axilla. There were no masses, calcifications, or visible distortion.

Ultrasound showed multiple non-mass lesions in different quadrants without distortion or associated vascularity. The largest lesion was in the upper inner quadrant (UIQ). There were several abnormal lymph nodes in the right axilla with a thick and markedly hypoechoic cortex and some lymph nodes with loss of fatty hilum. BI-RADS Category 4C. Ultrasound-guided percutaneous biopsies (12G core needle) of the dominant non-mass lesion of the right breast and abnormal lymph nodes were performed. The histopathologic diagnosis was diffuse large B-cell non-Hodgkin's lymphoma, non-germinal center type, in the mass and the lymph node (Figure 2).

After the breast biopsy, a contrast MRI with gadolinium showed multiple non-mass enhancement with diffuse distribution in all quadrants, homogeneous and ascending contrast uptake (type I curve), increased volume and abnormal enhancement of the right nipple was also observed. Both findings presented restriction in the diffusion sequence and a low apparent diffusion coefficient (ADC) value. Abnormal axillary lymph nodes were observed in Berg levels I and II.

### **Case 2. Non-Hodgkin lymphoma**

A 39-year-old woman with non-Hodgkin lymphoma diagnosed 2 years before in the right axilla and currently in remission presented with a lump in her right

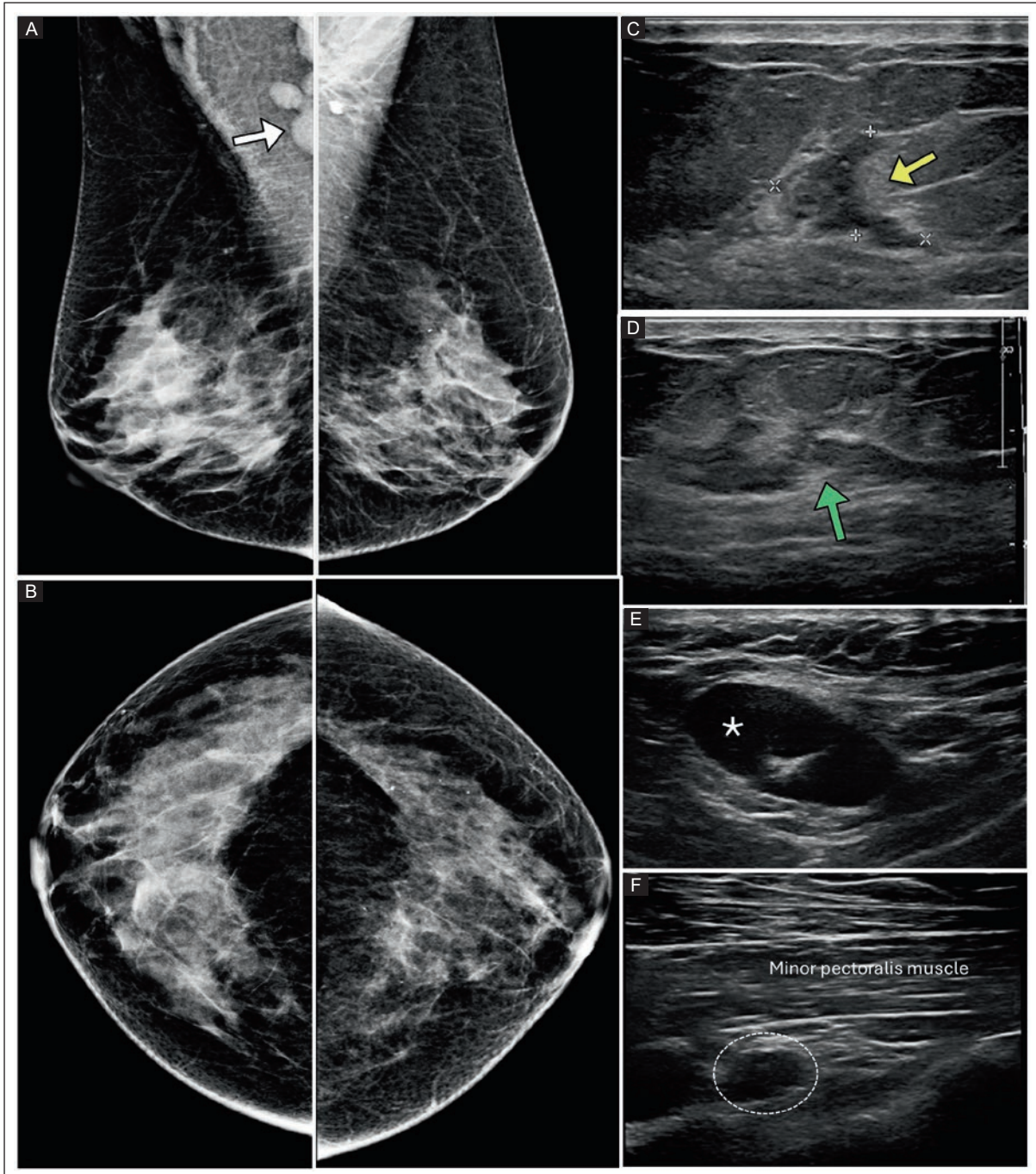


**Figure 1.** Case 1. A 63-year-old woman with palpable abnormal lymph nodes in the right axillary region. **A-B:** digital mammography in MLO and CC view shows global asymmetry with increased diffuse density in the right breast and no masses or architectural distortion. The right axilla has round and hyperdense lymph nodes (white arrow). **C-D:** US grayscale shows multiple non-mass lesions (yellow arrow) in different quadrants; the largest in the UIQ measures 3.2 cm (green arrow). **E-F:** there are five abnormal lymph nodes in the axilla at level I (asterisk) and two lymph nodes at level II (dotted circle), with a thick and clear hypoechoic cortex. BI-RADS Category 4C.

BI-RADS: Breast Imaging Reporting and Data System; CC: craniocaudal; MLO: mediolateral oblique; UIQ: upper inner quadrant; US: ultrasound.

breast. A mammogram showed an oval, hyperdense mass with an obscured margin at the junction of the upper quadrants (Figure 3). Another irregular, hyperdense mass was identified in the upper inner quadrant (UIQ).

Ultrasound confirmed a solid, isoechoic oval mass with a circumscribed margin and internal vascularity. Two hypoechoic irregular masses were identified in the UIQ (one was not seen on the mammogram) with spiculated margins and avascular. Abnormal lymph nodes

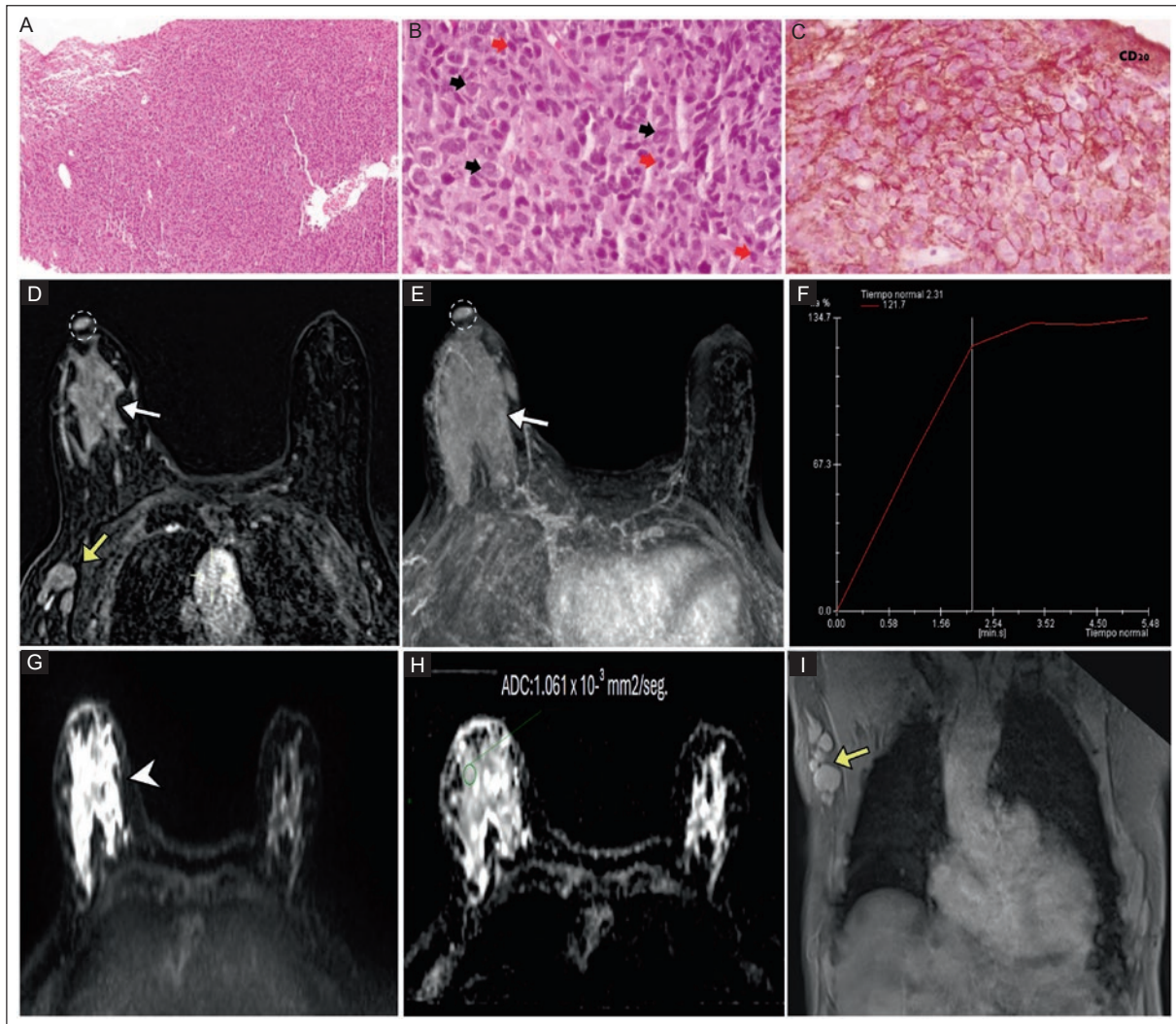


**Figure 2.** Case 1. A 63-year-old woman with palpable abnormal lymph nodes in the right axilla. Core biopsies of the dominant non-mass lesion in the right breast and right axilla node were performed. **A:** H&E 10x. Lymph node with loss of normal histologic architecture due to diffuse infiltration of atypical neoplastic lymphoid cells. **B:** H&E 40x. Large lymphoid cells with marked atypia, increased nucleus-cytoplasmic ratio, scant cytoplasm, vesicular chromatin, and sometimes macronucleoli (black arrows) on a polymorphic background composed of mature lymphocytes and neutrophils (red arrows). **C:** H&E 40x. IHC staining was diffusely positive for CD20 confirming B-lineage. The morphology and immunophenotype confirmed the histopathologic diagnosis of diffuse large B cell non-Hodgkin lymphoma, non-germinal center type, in the non-mass lesion and lymph node. **D-E:** T1-weighted dynamic contrast-enhanced MRI, MIP. Several areas of non-mass enhancement and diffuse distribution are seen in all quadrants (white arrows) in the right breast. Abnormal lymph nodes (yellow arrow). Increased volume and abnormal enhancement of the right nipple (dotted circles). **F:** homogeneous and ascending contrast uptake (type I curve). **G-H:** DWI and ADC. Both findings show a restriction in the diffusion sequence (white arrowhead) and an ADC value of  $1.06 \times 10^{-3} \text{ mm}^2/\text{sec}$ . **I:** T2 MRI coronal view shows round, hyperintense axillary lymph nodes with a thick cortex and obliteration of the fatty hilum at the I (yellow arrows) and II Berg levels. ADC: apparent diffusion coefficient; DWI: diffusion-weighted imaging; H&E: hematoxylin and eosin; IHC: immunohistochemistry; MIP: maximum intensity projection; MRI: magnetic resonance imaging.

were identified in the right axilla at Berg levels I and II. BI-RADS Category 5.

A percutaneous biopsy of the palpable mass was performed under US guidance (12G core needle) (Figure 4). The histologic diagnosis was a grade I follicular B-cell non-Hodgkin lymphoma. A biopsy of the

two spiculated masses was performed at UIQ (1 o'clock). The histopathologic diagnosis was triple-negative invasive carcinoma of no special type.

After the biopsy, contrast enhanced MRI with gadolinium was performed. A dominant 3.5 cm mass with an irregular margin and heterogeneous contrast uptake

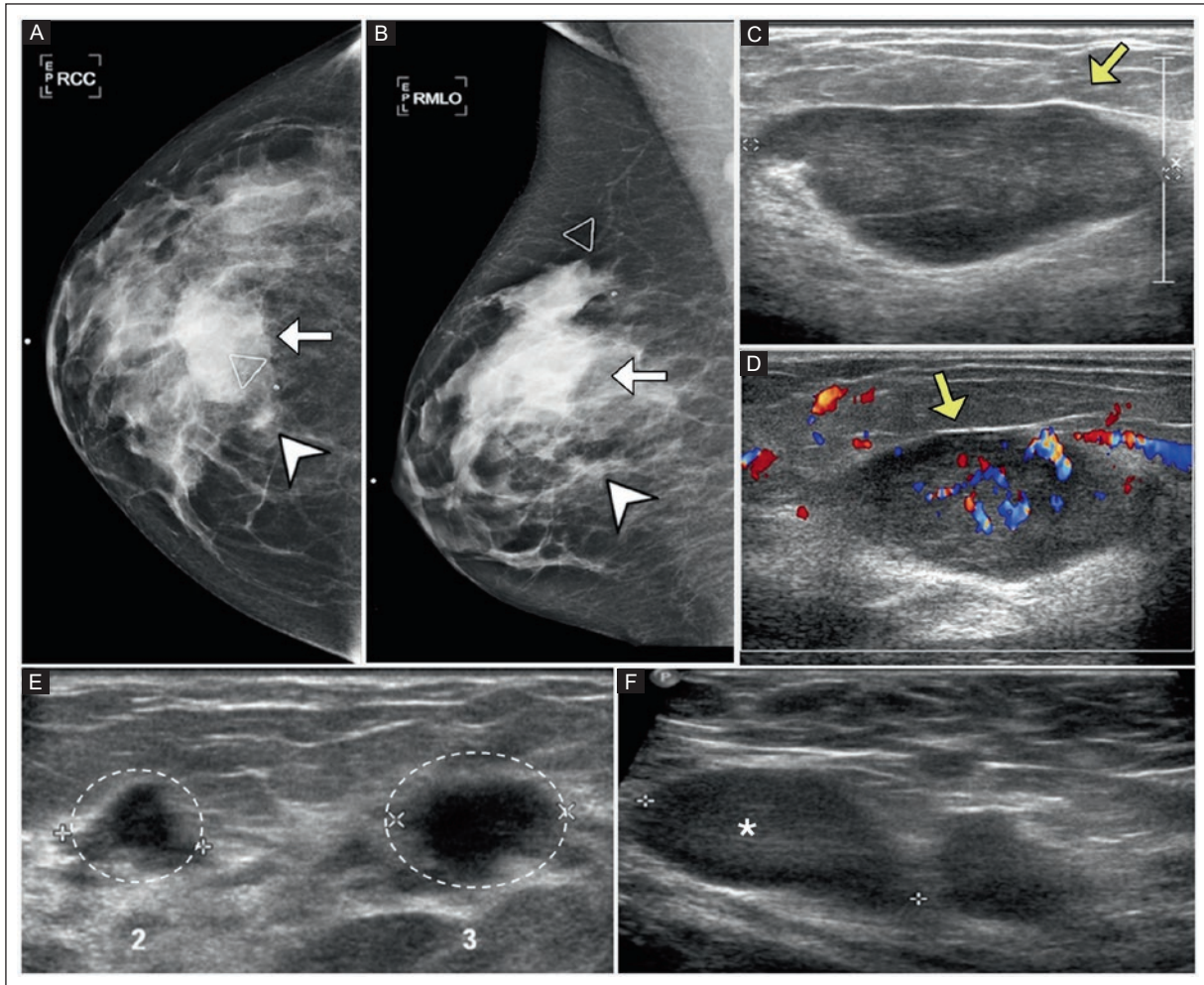


**Figure 3.** Case 2. A 39-year-old woman with non-Hodgkin lymphoma diagnosed 2 years earlier in the right axilla and currently in remission presented with a lump in the right breast. **A-B:** mammogram, CC, and MLO views show an oval, hyperdense mass with an obscured margin at the junction of the upper quadrants, 12 o'clock, and middle third (arrows) of the right breast. An irregular, hyperdense mass in the UIQ without associated calcifications (white arrowheads). **C-D:** grayscale and color Doppler US show a 3.8 cm solid, isoechoic, oval mass with a circumscribed margin and internal vascularity with color Doppler at 12 o'clock, 4 cm from the nipple in the right breast (yellow arrows). **E:** in the same breast, two irregular, markedly hypoechoic, avascular masses with spiculated margin (dotted circles), located at UIQ, 1 o'clock, 5 cm from the nipple. **F:** abnormal lymph nodes in the right axilla, the largest with cortical thickening up to 7 mm (asterisk) at I and II Berg levels. BI-RADS Category 5.

CC: craniocaudal; MLO: mediolateral oblique; UIQ: upper inner quadrant; US: ultrasound.

was found in the right breast. Two irregular enhanced masses in the UIQ with spiculated margins were confirmed. Multiple abnormal lymph nodes were found. The patient was treated with neoadjuvant chemotherapy and radiotherapy. MRI follow-up after treatment showed a complete absence of the dominant mass (lymphoma) and the two spiculated masses (triple-negative, no special type cancer) related to complete treatment response. Half of the abnormal lymph nodes described in the axilla disappeared, corresponding to a partial treatment response.

## LEUKEMIA

Secondary infiltration of the breast by leukemia is rare. The most common subtype (60 %) is acute myeloid leukemia<sup>2,9</sup>, while chronic leukemia infiltration is uncommon<sup>2,9</sup>. Premenopausal women<sup>10</sup> with a median age of 33 years<sup>2,9</sup> are usually affected. There are three clinical scenarios: the first is prior infiltration of the bone marrow, historically known as granulocytic sarcoma, in which systemic disease develops within two years; the second is during or after the diagnosis

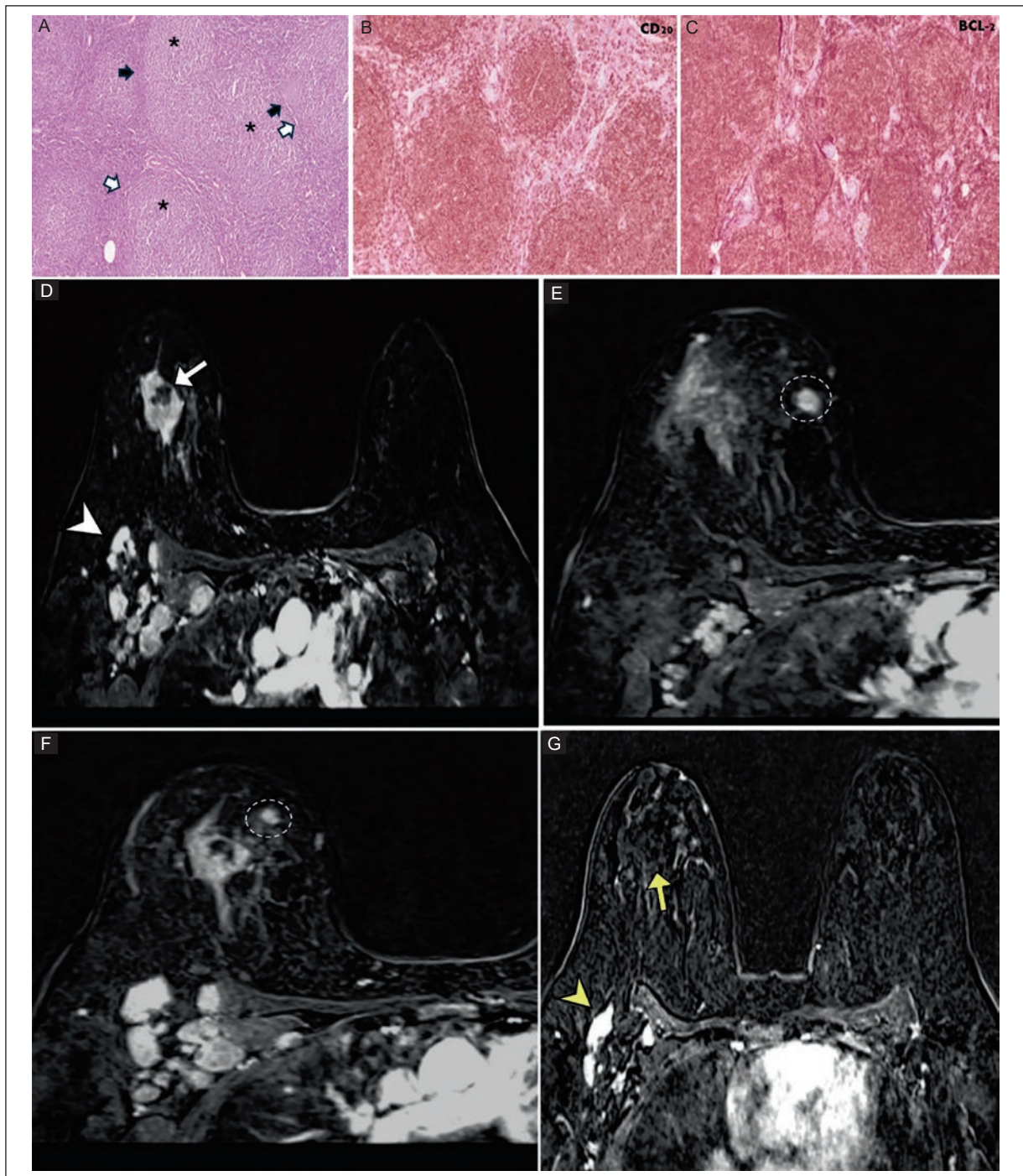


**Figure 4.** Case 2. A 39-year-old woman with non-Hodgkin lymphoma diagnosed 2 years before in the right axilla presented with a lump in the right breast. Core biopsies of the right breast and right axillary lymph node were performed. **A:** H&E 10 $\times$ . Neoplastic follicles similar in size (white arrows) form germinal centers composed of small cells and attenuate the mantle and adjacent marginal areas (black arrows). Follicles do not polarize (asterisks) and have lack tingible bodies. **B-C:** H&E 40 $\times$ . IHC stains were strongly and diffusely positive for CD20, confirming B-lineage lymphoma. BCL2 was positive in the neoplastic germinal centers. The axillary lymph node showed partial fading of the histologic architecture due to low-grade hematolymphoid proliferation in a follicular pattern. The histopathologic diagnosis was non-Hodgkin's Lymphoma, grade I follicular lymphoma. **D, E,** and **F:** T1-weighted dynamic contrast-enhanced MRI axial view showing a mass with an irregular margin measuring 3.5 cm and heterogeneous contrast uptake at 12 o'clock in the right breast (white arrow). The UIQ shows two irregular, enhanced masses with a spiculated margin, measuring 1.1 cm and 9 mm, respectively (dotted circles). The axilla has multiple abnormal, round lymph nodes with cortical thickening and loss of the fatty hilum (white arrowheads). **G:** T1-weighted dynamic contrast-enhanced MRI axial view after neoadjuvant chemotherapy and radiotherapy. Absence of the dominant mass (lymphoma) at 12 o'clock and the two spiculated masses (triple-negative NST cancer) related with complete treatment response (yellow arrow). Half of the abnormal lymph nodes described in the axilla have disappeared, indicating a partial response of the lymph nodes (yellow arrowhead). H&E: hematoxylin and eosin; IHC: immunohistochemistry; MRI: magnetic resonance imaging; NST: no special type; UIQ: upper inner quadrant.

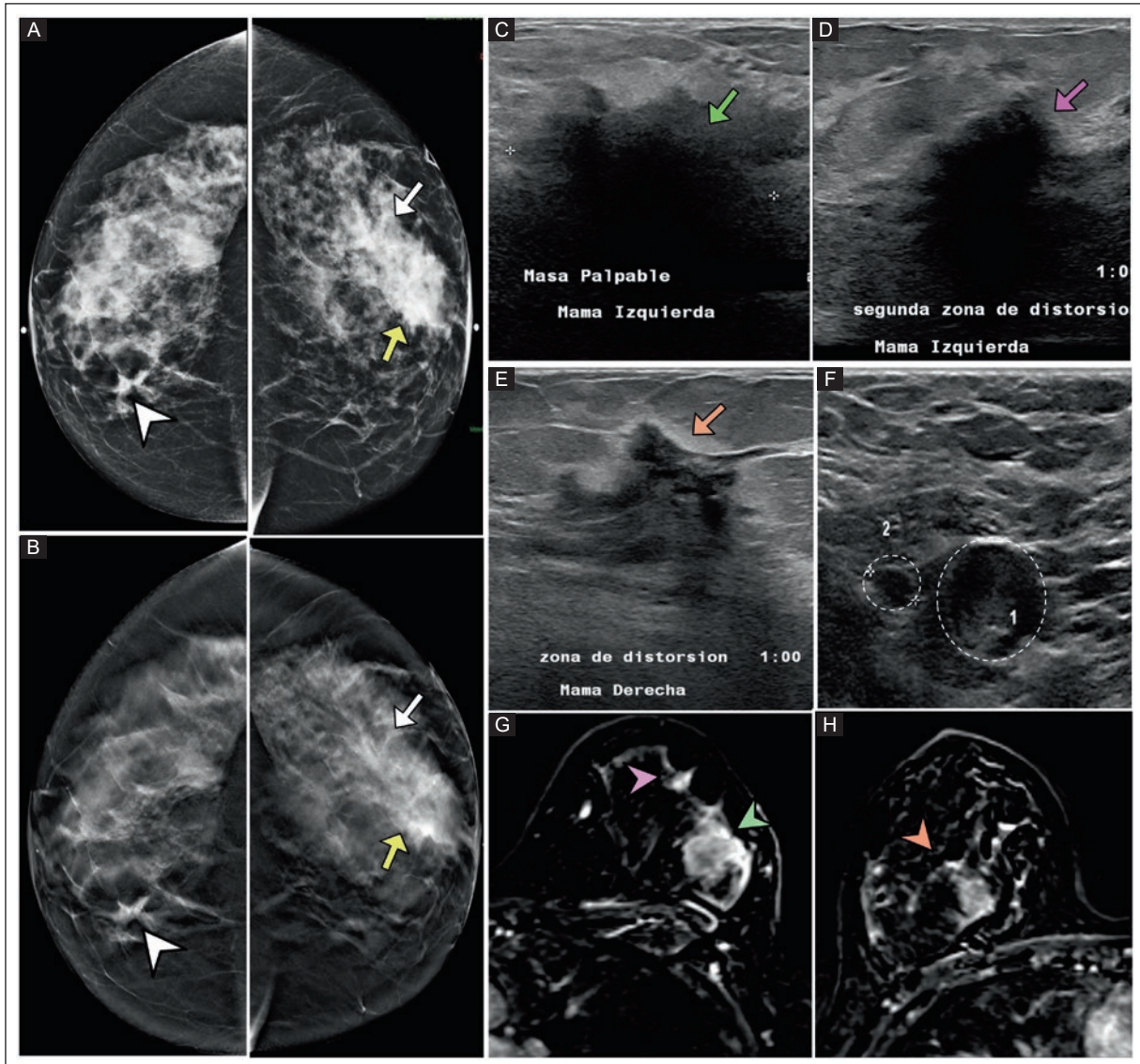


**Figure 5.** Case 3. A 39-year-old woman diagnosed with acute myeloblastic leukemia in remission who had recently received a bone marrow transplant. She presented with a palpable lump in her left breast. **A-B:** digital mammography and tomosynthesis, CC view, shows an irregular, dense mass with a spiculated margin at the junction of the outer quadrants at 3 o'clock, measuring 3.5 cm in the left breast (yellow arrows). An area of distortion was observed in the UOQ, which was confirmed by tomosynthesis (white arrows). In the right breast, a zone of distortion was identified in the UIQ that is only visible in the CC view and measures 1.7 cm (arrowheads). **C:** US grayscale, an irregular, hypoechoic, spiculated mass, is confirmed in the left breast at 3 o'clock, 7 cm from the nipple, measuring 3.1 × 2.8 cm (green arrow). **D:** an area of distortion in the UOQ measuring 2.0 cm at 1 o'clock and 5 cm from the nipple is seen (purple arrow). **E-F:** an area of distortion is identified in the UIQ of the right breast (orange arrow) at 1 o'clock. Two abnormal lymph nodes with a thick cortex, up to 5 mm, are observed in the left axilla (dotted circles). BI-RADS Category 5. **G:** dynamic MRI axial view shows two enhanced masses of irregular shape and margin in the UOQ of the left breast, measuring 3.5 cm (green arrowhead) and 2.3 cm (purple arrowhead), respectively. **H:** an enhanced mass with irregular morphology and margins is seen in the UIQ of the right breast (orange arrowhead), which is consistent with the area of distortion described on the mammogram.

BI-RADS: Breast Imaging Reporting and Data System; CC: craniocaudal; MRI: magnetic resonance imaging; UIQ: upper inner quadrant; UOQ: upper outer quadrant; US: ultrasound.

of systemic disease<sup>9,10</sup>, and the third is recurrence after completing chemotherapy and/or bone marrow transplantation<sup>11</sup>. The latter was the most common clinical presentation (42.4%) in a study by Surov et al.<sup>9</sup>.

The most common clinical manifestation is a palpable, painless, unilateral, or bilateral mass, which may or may not be associated with axillary lymphadenopathy (17%). Other less common clinical manifestations



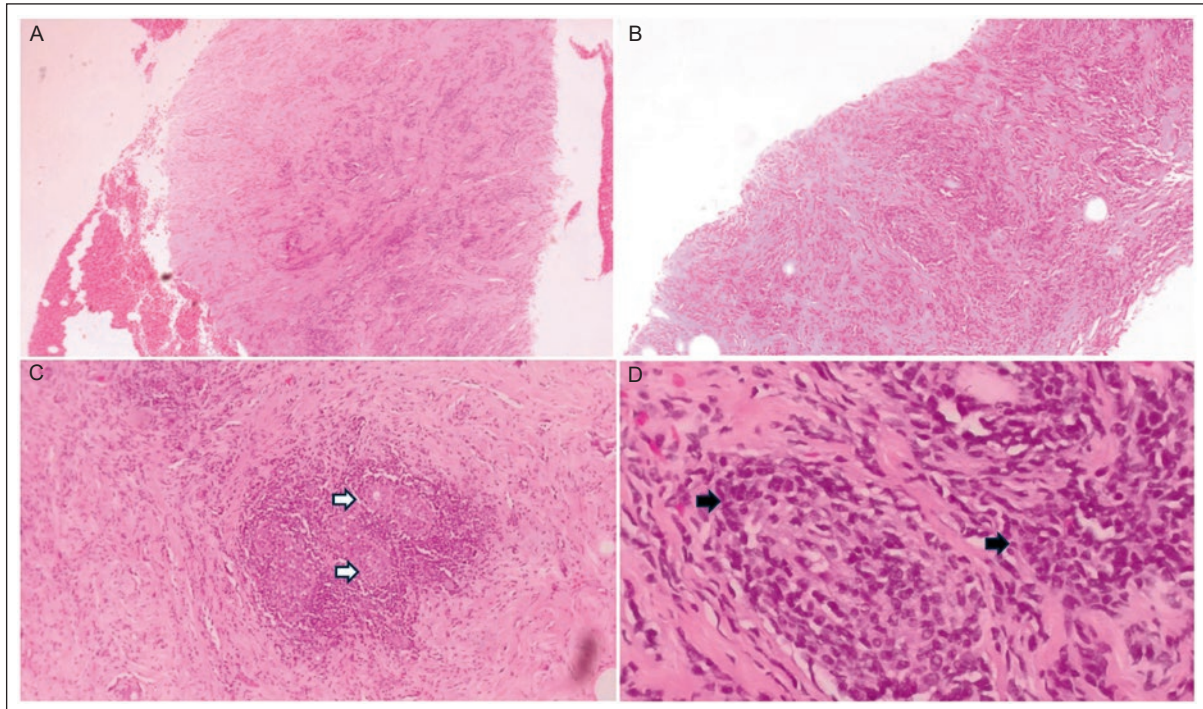


**Figure 6.** Case 3. A 39-year-old woman diagnosed with acute myeloblastic leukemia in remission and a recent bone marrow transplant presented with a lump in her left breast. Bilateral core biopsies were performed. **A:** H&E 2.5 $\times$ . Loss of normal breast architecture due to diffuse neoplastic infiltration. **B:** H&E 2.5 $\times$ . Hematolymphoid proliferation is monomorphic and occupies the entire biopsied tissue. **C:** H&E 10 $\times$ . Focally preserved glands or residual epithelial elements of the breast parenchyma (white arrows). **D:** H&E 40 $\times$ . Atypical lymphoid-like cells are infiltrating widely a sclerotic stromal background (black arrows). The histopathologic diagnosis was hematolymphoid infiltration related to acute myeloblastic leukemia.

H&E: hematoxylin and eosin.

in the breast include edema or skin erythema, nipple retraction, or an incidental finding in an asymptomatic patient during screening mammography<sup>9</sup>. Breast imaging findings are not specific for leukemia, and it is important to know the patient's medical history<sup>12</sup>.

### Mammography

The most common finding in breast infiltration secondary to leukemia is a hyperdense mass, single or multiple, with a non-circumscribed margin. There may also be breast architecture distortion and a diffuse increase in breast density; calcifications are rare. A normal mammogram may be found<sup>2,9</sup>.

### Ultrasound

The most common finding of secondary infiltration of the breast by leukemia is a single or multiple hypo-echoic mass with heterogeneous echotexture and an indistinct or microlobulated margin. There is internal vascularity on color Doppler and a hard pattern on elastography<sup>2,13</sup>.

### MRI

Few cases of secondary infiltration of the breast by leukemia have been described<sup>9,12</sup>. The lesions are hyperintense in T2 with heterogeneous enhancement after contrast administration. Non-mass enhancement, diffuse distribution, and a heterogeneous pattern have been reported<sup>9,12</sup>.

### Case 3. Acute myeloblastic leukemia

A 39-year-old woman diagnosed with acute myeloblastic leukemia in remission with a recent bone marrow transplant presented with a lump in her left breast. On mammography, an irregular, dense mass with a spiculated margin was observed in the left breast at the junction of the outer quadrants and an area of distortion in the upper outer quadrant (UOQ), confirmed by tomosynthesis (Figure 5). An area of palpable distortion was identified in the right breast in the anterior third of the UIQ.

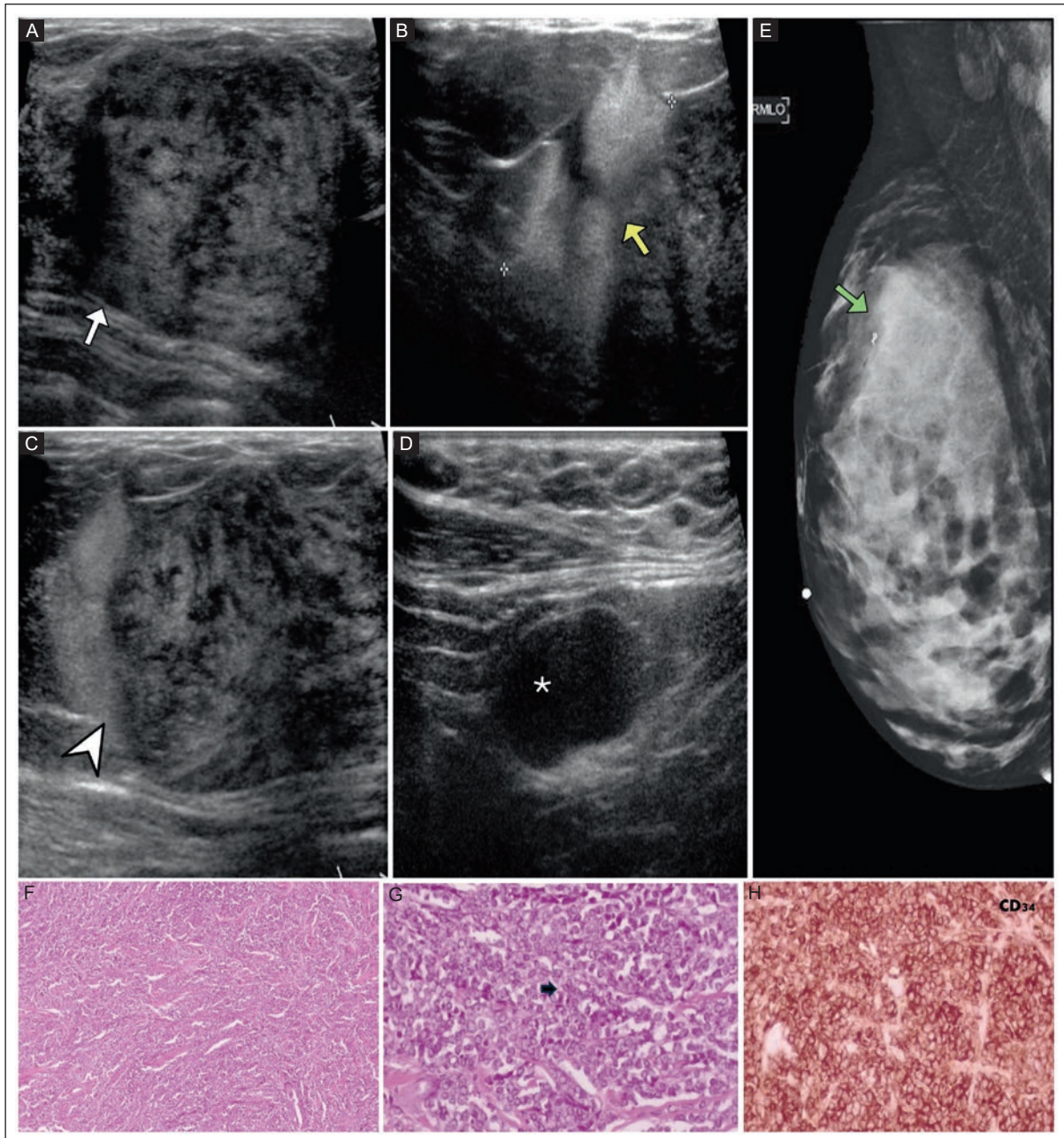


**Figure 7.** Case 4. A 27-year-old woman recently diagnosed with acute lymphoblastic B leukemia and treated with chemotherapy presented with a lump in the right breast. **A:** US grayscale shows a dominant solid, round mass with heterogeneous echogenicity on UOQ at 11 o'clock, 8 cm from the nipple, measuring 3.7 cm, and with internal vascularity on color Doppler in the right breast (white arrow). **B-C:** an echogenic, non-mass lesion (yellow arrow) measuring 2.7 cm in the anteroposterior diameter is adjacent to and outside this mass. Both findings completely occupy the UOQ (white arrowhead). **D:** three abnormal lymph nodes with thick cortex are seen in the axillary region, markedly hypoechoic with absent fatty hilum (asterisk), the largest with a cortical thickness of 9 mm. BI-RADS Category 4C. A core biopsy of the right breast was performed. **E:** mammogram, MLO view shows an isodense irregular mass after biopsy in the right breast (green arrow). The tissue marker of the biopsy is confirmed at the site. **F:** H&E 10x. Diffuse hematolymphoid neoplastic infiltration in a sheet-like pattern. No native epithelial elements are observed. **G:** H&E 40x. Monomorphic proliferation comprises immature cells of blast-like appearance, medium to large size with open chromatin, basophilic with scant cytoplasm (black arrow). **H:** H&E 40x. IHC staining was diffusely positive for CD34. The histopathologic diagnosis was infiltration of immature/blastic B lymphoid cells related to acute lymphoblastic B leukemia.

BI-RADS: Breast Imaging Reporting and Data System; H&E: hematoxylin and eosin; IHC: immunohistochemistry, MLO: mediolateral oblique; UOQ: upper outer quadrant; US: ultrasound.

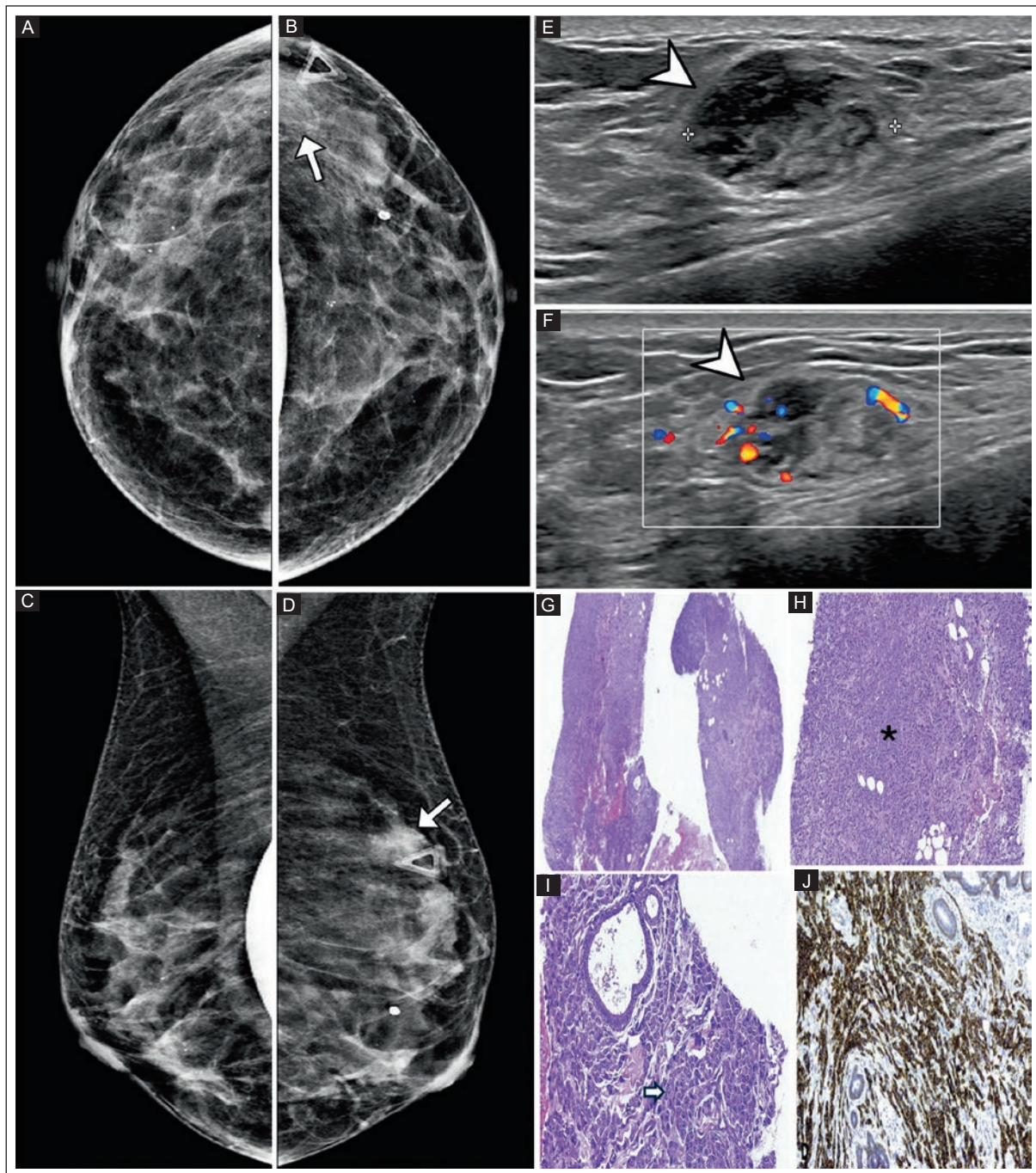


**Figure 8.** Case 5. A 66-year-old woman with a history of multiple myeloma presented with a lump in the left breast. **A, B, C, D:** mammogram, CC, and MLO views, with Eklund technique. A round isodense mass with an obscured margin was observed in the UOQ, middle third of the left breast (white arrows). **E-F:** US grayscale and color Doppler. A round mass with a heterogeneous echotexture and indistinct margin was confirmed, located in the UOQ at 2 o'clock, 8 cm from the nipple, measuring 1.5 cm with internal vascularity (arrowheads). BI-RADS 4B. A core biopsy of the left breast was performed. **G:** H&E 2.5 $\times$ . Hypercellular neoplastic proliferation replaces the entire normal breast tissue. **H:** H&E 10 $\times$ . Diffuse infiltration by plasmacytoid proliferation, discohesive, monoclonal appearance, with sheet and nest pattern (asterisk). **I:** H&E 10 $\times$ . Monotonous, predominantly plasmacytoid neoplastic cells with abundant basophilic cytoplasm, eccentric nuclei (white arrow), and occasionally with clockwork chromatin (white arrow). **J:** H&E 10 $\times$ . Strong and diffuse membrane-positive CD138-positive IHC in neoplastic proliferation. The histopathologic diagnosis was plasma cell neoplasm infiltration of the breast.

BI-RADS: Breast Imaging Reporting and Data System; CC: craniocaudal; H&E: hematoxylin and eosin; IHC: immunohistochemistry; MLO: mediolateral oblique; UOQ: upper outer quadrant; US: ultrasound.

Ultrasound of the left breast showed an irregular, hypoechoic mass with a spiculated margin and an area of distortion. An area of distortion was also found in the right breast. Two abnormal lymph nodes were found in the left axilla. BI-RADS Category 5.

On MRI, two irregular enhanced masses were confirmed in the UOQ of the left breast. In contrast, an enhanced mass with irregular morphology and margin in the right breast was confirmed in the UIQ and was consistent with the area of distortion described on the mammogram.

Ultrasound-guided percutaneous biopsies (12G core needle) were performed in both breasts. The histopathologic diagnosis was hematolymphoid infiltration related to acute myeloblastic leukemia (Figure 6).

#### **Case 4. Acute lymphoblastic B leukemia**

A 27-year-old woman recently diagnosed with acute lymphoblastic B leukemia and treated with chemotherapy presented with a lump in her right breast. US gray-scale showed a dominant solid, round mass with heterogeneous echogenicity and internal vascularity on color Doppler in the UOQ of the right breast (Figure 7). Three abnormal lymph nodes were identified in the axillary region, the largest with a cortical size of 9 mm. BI-RADS Category 4C.

An ultrasound-guided percutaneous core biopsy (12G core needle) was performed. Mammography after the percutaneous biopsy showed an isodense, irregular mass without calcifications. The tissue marker of the biopsy was also present. The histopathologic diagnosis was acute lymphoblastic B leukemia.

#### **Multiple myeloma**

Multiple myeloma is a plasma cell disease that occurs most frequently in the sixth decade of life. Its extramedullary location occurs as a solitary lesion (plasmacytoma) or recurrences in less than 5% of cases<sup>14</sup>. Plasmacytomas are rare and originate mainly in the head and neck but can occur in any organ<sup>2</sup>. One hundred fifty-three cases have been reported in the breast<sup>15</sup>.

#### **Mammography**

A plasmacytoma is a round or oval mass with a circumscribed margin. Microcalcifications are rare<sup>16</sup>.

#### **Ultrasound**

Plasmacytoma is a solid mass with variable echogenicity, a circumscribed margin, and variable vascularity<sup>16</sup>.

#### **MRI**

Hypointense masses are observed in the T1 sequence and hyperintense in T2. After administration of a contrast agent, they are hypervascularized and show ring uptake<sup>16</sup>.

#### **Case 5. Multiple myeloma**

A 66-year-old woman with a recent history of multiple myeloma presented with a palpable mass in the left breast. Mammography revealed a round isodense mass with an obscured margin in the UOQ of the left breast (Figure 8). Ultrasound confirmed the presence of a round mass with a heterogeneous echotexture and an indistinct margin with internal vascularity on color Doppler. BI-RADS 4B. An ultrasound-guided percutaneous core biopsy (12G needle) was performed, and the histopathologic diagnosis was plasmacytoma of the breast.

#### **CONCLUSION**

Hematologic malignancies affecting the breast include lymphomas, leukemias, and multiple myelomas. They most commonly occur as a secondary infiltration of the breast, although they can also be primary breast tumors. Infiltration of the breast can be bilateral, especially in lymphomas and leukemias. The most common imaging findings are mass(es), non-mass lesions, or architectural distortion, and, less commonly, diffusely increased breast density. Calcifications are rare. A complete ultrasound examination of the axilla is essential, as axillary lymphadenopathy is often present. MRI with contrast medium allows a better assessment of the extent of the disease. A biopsy is always recommended in breast imaging for accurate diagnosis of suspicious findings in patients diagnosed with a hematologic malignancy.

#### **Acknowledgments**

The authors thank Professor Ana M. Contreras-Navarro for her guidance in preparing and writing this scientific paper.

#### **Funding**

This research received no external funding.

#### **Conflicts of interest**

The authors declare that they have no conflicts of interest.

## Ethical disclosures

**Protection of individuals.** This study complied with the Declaration of Helsinki (1964) and subsequent amendments.

**Confidentiality of data.** The authors declare they followed their center's protocol for sharing patient data.






**Right to privacy and informed consent.** Informed consent was not required for this observational study of information collected during routine clinical care.

**Use of artificial intelligence.** The authors did not use generative artificial intelligence to prepare this manuscript and/or create tables, figures, or figure legends.

## REFERENCES

1. Wienbeck S, Meyer HJ, Uhlig J, Herzog A, Nemat S, Teifke A. Radiological imaging characteristics of intramammary hematological malignancies: results from a German multicenter study. *Sci Rep.* 2017;7(1):7435. doi: 10.1038/s41598-017-07409-z.
2. Glazebrook KN, Zingula S, Jones KN, Fazzio RT. Breast imaging findings in haematological malignancies. *Insights Imaging.* 2014;5(6):715-722. doi: 10.1007/s13244-014-0344-2.
3. Shim E, Song SE, Seo BK, Kim YS, Son GS. Lymphoma affecting the breast: a pictorial review of multimodal imaging findings. *J Breast Cancer.* 2013;16(3):254-265. doi: 10.4048/jbc.2013.16.3.254.
4. Raj SD, Shurafa M, Shah Z, Raj KM, Fishman MDC, Dialani VM. Primary and Secondary Breast Lymphoma: Clinical, Pathologic, and Multimodality Imaging Review. *Radiographics.* 2019;39(3):610-625. doi: 10.1148/rg.2019180097.
5. Paes FM, Kalkanis DG, Sideras PA, Serafini AN. FDG PET/CT of extranodal involvement in non-Hodgkin lymphoma and Hodgkin disease. *Radiographics.* 2010;30(1):269-291. doi: 10.1148/rg.301095088.
6. Yang WT, Lane DL, Le-Petross HT, Abruzzo LV, Macapinlac HA. Breast lymphoma: imaging findings of 32 tumors in 27 patients. *Radiology.* 2007;245(3):692-702. doi: 10.1148/radiol.2452061726.
7. Moura C, Leite MI, Parreira R, Medeiros A. Primary breast lymphoma. *J Surg Case Rep.* 2020;2020(1):1-3 rjz405. doi: 10.1093/jscr/rjz405.
8. Surov A, Holzhausen HJ, Wienke A, Schmidt J, Thomssen C, Arnold D. Primary and secondary breast lymphoma: prevalence, clinical signs and radiological features. *Br J Radiol.* 2012;85(1014):e195-205. doi: 10.1259/bjr/78413721.
9. Surov A, Wienke A, Abbas J. Breast leukemia: an update. *Acta Radiol.* 2012;53(3):261-266. doi: 10.1258/ar.2011.110470.
10. Cunningham I. A clinical review of breast involvement in acute leukemia. *Leuk Lymphoma.* 2006;47(12):2517-2526. doi: 10.1080/10428190600967022.
11. Linn YC, Goh YT, Tan HC. Relapse of leukemia and lymphoma after marrow transplantation: a review of cases with extramedullary relapse. *Leuk Lymphoma.* 2000;38(1-2):137-146. doi: 10.3109/10428190009060327.
12. Kim SJ. Magnetic resonance imaging features of breast leukemia. *Magn Reson Med Sci.* 2013;12(4):309-313. doi: 10.2463/mrms.2012-0091.
13. Bayrak IK, Yalin T, Ozmen Z, Aksoz T, Doughanji R. Acute lymphoblastic leukemia presented as multiple breast masses. *Korean J Radiol.* 2009;10(5):508-510. doi: 10.3348/kjr.2009.10.5.508.
14. Ali HOE, Nasir Z, Marzouk AM. Multiple Myeloma Breast Involvement: A Case Report. *Case Rep Radiol.* 2019; 2019:2079439. doi: 10.1155/2019/2079439.
15. Surov A, Holzhausen HJ, Ruschke K, Arnold D, Spielmann RP. Breast plasmacytoma. *Acta Radiol.* 2010;51(5):498-504. doi: 10.3109/02841851003712924.
16. Kocaoglu M, Somuncu İ, Bulakbasi N, Tayfun C, Taşar M, Günhan Ö, et al. Multiple myeloma of the breast: mammographic, ultrasonographic and magnetic resonance imaging features. *Eur J Radiol Extra.* 2003; 47: 112-116. doi:10.1016/S1571-4675(03)00064-6.

# The PROMISE-V2 PRIMARY score and SULmax [<sup>18</sup>F]PSMA-1007 PET/CT in primary staging of prostate cancer

J. Antonio Serna-Macias<sup>1,2</sup>, M. Lourdes Garcia-Colmenero<sup>3\*</sup>, Emily A. Cortes-Mancera<sup>4</sup>,  
E. David Muñoz-Carpio<sup>5</sup>, and Mixel Z. Baltierra-Hernandez<sup>5</sup>

<sup>1</sup>Postgraduate of High Specialty in Positron Emission Tomography/Computed Tomography, Universidad Nacional Autónoma de México, Mexico City; <sup>2</sup>Radiology and Imaging Service, Hospital Angeles Pedregal, Mexico City; <sup>3</sup>Departamento de Imagen Molecular – PET/CT, CID Centro de Imagen y Diagnóstico, Guadalajara, Jalisco; <sup>4</sup>Servicio de Medicina Nuclear, Hospital Central Sur de Alta Especialidad, Petróleos Mexicanos, Mexico City; <sup>5</sup>Departamento de Atención a la Salud, Unidad Xochimilco, Universidad Autónoma Metropolitana, Mexico City, Mexico

## ABSTRACT

**Introduction:** The PRIMARY score of the PROMISE-V2 criteria for primary staging of prostate cancer (PCa) and its relationship with the maximum standardized uptake value normalized to lean body mass (SULmax) have not been evaluated. This study determined the relationship between the SULmax value in [<sup>18</sup>F]PSMA-1007 PET/CT and the PROMISE-V2 PRIMARY score in patients with untreated PCa in primary staging. **Material and Methods:** This cross-sectional study included patients with PCa in primary staging. The SULmax value [<sup>18</sup>F]PSMA-1007 PET/CT of the intraprostatic lesion was recorded, and the PRIMARY score was assessed based on the pattern of affected prostate zones (peripheral, transitional, or central) and the distribution of prostate-specific membrane antigen (PSMA) uptake (focal or diffuse). Lymph node (pelvic or extrapelvic) spread and metastasis (bone, lung, and/or brain) were determined. **Results:** Fifty-five patients with PCa at primary staging were included. The SULmax value of an intraprostatic tumor in PRIMARY score 2 was  $5.15 \pm 0.54$  g/mL; in PRIMARY score 3, 7.11 g/mL; in PRIMARY score 4,  $8.31 \pm 1.92$  g/mL, and in PRIMARY score 5,  $22.64 \pm 7.77$  ( $p < 0.001$ ). The SULmax value of [<sup>18</sup>F]PSMA increased in direct association with the PRIMARY score in cases with an intraprostatic tumor ( $11.49 \pm 6.69$  g/mL ( $p < 0.001$ )) and an intraprostatic tumor + pelvic lymph nodes ( $15.17 \pm 9.72$  g/mL). In contrast, cases with extrapelvic lymph nodes or metastases (bone, brain, or lung) had lower SULmax values ( $12.43 \pm 8.73$  g/mL) ( $p < 0.001$ ). **Conclusion:** Our study showed an association between the SULmax value and the PRIMARY score according to the affected anatomical zone, the expression patterns and a SULmax > 12 g/mL. The expression of PSMA uptake in the local tumor was highest in the pattern of focal involvement in the peripheral zone (PZ) as long as the disease was confined to the pelvis.

**Keywords:** Prostate cancer. Prostate-specific membrane antigen. Positron emission tomography/computed tomography. SULmax value. PCa primary staging. Prostate cancer molecular imaging standardized evaluation.

## INTRODUCTION

Prostate cancer (PCa) is the second most common neoplasm in men<sup>1,2</sup>. At the time of diagnosis, 10 to 20% of patients have locally advanced disease and 8 to 35% distant metastatic disease<sup>3</sup>. Positron emission tomography/computed tomography (PET/CT) with prostate-specific membrane antigen (PSMA) is a hybrid imaging modality

that detects and defines local and/or distant PCa and provides information on tumor biology, disease prognosis and treatment planning<sup>4</sup>. Intraprostatic tumors can be detected qualitatively by visual assessment of lesions based on their pattern and location or quantitatively by radiopharmaceutical uptake in a target lesion using the maximum standardized uptake value (SUVmax) and a comparison with normal tissue<sup>5</sup>.

### \*Corresponding author:

M. Lourdes Garcia-Colmenero  
E-mail: lula.gacol@gmail.com

Received for publication: 10-06-2024

Accepted for publication: 12-09-2024

DOI: 10.24875/JMEXFRI.M24000091

Available online: 20-12-2024

J Mex Fed Radiol Imaging. 2024;3(4):243-255

www.JMeXFRI.com

2696-8444 / © 2024 Federación Mexicana de Radiología e Imagen, A.C. Published by Permanyer. This is an open access article under the CC BY-NC-ND (<https://creativecommons.org/licenses/by-nc-nd/4.0/>).

Several factors influence the SUVmax.<sup>6</sup> It is relatively higher in obese patients than thinner patients. One study found that SUV correction for lean body mass, known as the maximum standardized uptake value normalized to lean body mass (SULmax) radiotracer concentration, is a more appropriate quantitative method,<sup>6</sup> suggesting that SULmax is preferable to SUVmax for quantitative analysis.<sup>7</sup> Some authors<sup>8-12</sup> have analyzed the SUVmax according to the prostate zone, area, uptake pattern, and segmentation, similar to intraprostatic biopsy. It has also been described that a high SULmax value is related to the presence of metastases<sup>10,11,13,14</sup>.

The PROMISE (Prostate Cancer Molecular Imaging Standardized Evaluation) criteria define guidelines for clinical trial design and self-reporting of molecular imaging in PCa<sup>15</sup>. In 2023, the second version, PROMISE-V2, was published with two standardized hierarchy levels by whole-body molecular imaging TNM staging (miTNM) and PSMA expression for primary staging (PRIMARY score) or recurrence (PSMA expression score) in patients with PCa<sup>16</sup>. The reproducibility and clinical application of the PRIMARY score in patients with primary staging of PCa have not been sufficiently evaluated. In addition, the relationship between the SULmax and zone involvement and the pattern of PSMA expression proposed in the PRIMARY score has not been defined. This study determined the relationship between SULmax on [<sup>18</sup>F]PSMA-1007 PET/CT and the PROMISE-V2 PRIMARY score in patients with untreated PCa undergoing primary staging.

## MATERIAL AND METHODS

A cross-sectional study was conducted from June 1, 2019, to May 31, 2023, in the Radiology and Imaging Service of the Hospital Angeles Pedregal in Mexico City, Mexico. Patients with histopathologically confirmed PCa for primary staging were referred by oncology, urology, and radiation oncology specialists for PET/CT examination with [<sup>18</sup>F]PSMA-1007. Patients without information on prostate-specific antigen (PSA), a Gleason score, or previously treated PCa were excluded. Informed consent was not requested due to the observational and retrospective design of the study. The Institutional Research Ethics and the Research Committees approved the protocol.

### Study development and variables

The information was obtained from the clinical records. The variables included were age, the [<sup>18</sup>F]PSMA-1007

dose administered to perform PET/CT, the PSA value, and the Gleason score. The SULmax value of the intraprostatic lesion from the [<sup>18</sup>F]PSMA PET/CT examination and the presence or absence of lymph node spread (pelvic or extrapelvic) and metastases (bone, lung, brain) were recorded.

## Definitions

*Primary staging:* patients with a recent and confirmed diagnosis of PCa without treatment before the [<sup>18</sup>F]PSMA PET/CT.

*Tumor staging:* organ-confined tumor (unifocal or multifocal); non-organ-confined tumor (extracapsular extension and/or tumor invading the seminal vesicle[s]); tumor invading adjacent structures such as the external sphincter, rectum, bladder, levator muscles, and/or pelvic wall<sup>15,16</sup>.

*Pelvic lymph nodes:* internal iliac, external iliac, obturator, presacral, and other pelvic lymph nodes<sup>15,16</sup>.

*Metastasis:* extrapelvic lymph nodes (common iliac, retroperitoneal, supradiaphragmatic, inguinal, other extrapelvic); bone uptake patterns (unifocal, oligometastatic, disseminated, diffuse bone marrow involvement); other involved organs (lung and brain)<sup>15,16</sup>.

*PRIMARY score:* a staging system for intraprostatic lesions in men diagnosed with previously untreated PCa<sup>8,9,16</sup>:

Score 1: no dominant intraprostatic pattern; low-grade activity.

Score 2: diffuse activity in the transition zone (TZ) or symmetric activity in the central zone (CZ) that does not extend to the prostate margin on CT.

Score 3: focal TZ activity that is visually twice as high as background activity.

Score 4: focal activity in the peripheral zone (PZ) (no minimum intensity).

Score 5: PSMA SUVmax >12. In this study, SULmax was used to replace SUVmax with comparable values.

*SULmax:* maximum standardized uptake value normalized to the lean body mass concentration of the radiotracer [<sup>18</sup>F]PSMA-1007, measured in g/mL<sup>5,17</sup>.

*Gleason score:* low-risk PCa (Gleason score 6 = 3 + 3), intermediate-risk PCa (Gleason score 7 = 3 + 4/4 + 3, and 8), and high-risk PCa (Gleason score > 8)<sup>18</sup>. Intermediate and high-risk Gleason scores were considered together in the study analysis.

*miTNM system:* the staging system proposed by PROMISE-V2 allows standardized reporting of [<sup>18</sup>F]PSMA by tumor stage, nodal stage, and distant metastases<sup>16</sup>.

### Imaging protocol and analysis

PET/CT acquisition was performed with the hybrid PET/CT Philips Vereos Digital (Philips Medical Systems Technologies Ltd, Haifa, Israel) with the patient supine after intravenous administration of [<sup>18</sup>F]PSMA-1007 with a biodistribution time of 60 minutes. CT acquisition in 64-slice, multidetector, helical equipment was performed with axial slices from the convexity of the skull to the medial third of the thighs in single phase and/or after administration of oral and intravenous water-soluble contrast agent, as needed, for attenuation correction and anatomical localization. PET images were reconstructed using the iterative method and analyzed with and without CT image fusion on a medical-grade workstation (Philips, Shanghai, China).

The SULmax value was determined using software (IntelliSpace Portal IX/XL version 7.2, Philips, Amsterdam, The Netherlands) in the region of interest (ROI) with the features described below. The SULmax value was quantified in the intraprostatic lesion ( $\geq 10$  mm) to ensure adequate spatial resolution with a ROI of 1 cm diameter over the voxel with maximum uptake in the axial plane.

According to the PRIMARY score, the pattern of tumor involvement in the prostatic zones (TZ, CZ, PZ) was recorded and based on the combination of the intraprostatic pattern and the uptake intensity of the radiotracer [<sup>18</sup>F]PSMA-1007 (Figure 1). The local morphological extent of the tumor was also determined by CT: tumor confined to the prostate, involvement of the capsule/seminal vesicles, or infiltration of adjacent structures (external sphincter, rectum, urinary bladder, pelvic wall, or levator muscles). The findings were reported by an experienced nuclear medicine physician (JASM) with 20 years of experience in PET/CT.

### Statistical analysis

The mean, standard deviation, minimum, median, and maximum SULmax value of intraprostatic tumor and its relation with the PROMISE-V2 PRIMARY score and extent of PCa and the mean, standard deviation, minimum, median and maximum SULmax value of the prostate tumor and PSA levels were determined according to the location and extent of PCa. The p-value for normality was calculated using the Kolmogorov-Smirnov or the Shapiro-Wilk test. The OR was calculated for the expression patterns [<sup>18</sup>F]PSMA (PRIMARY score) and

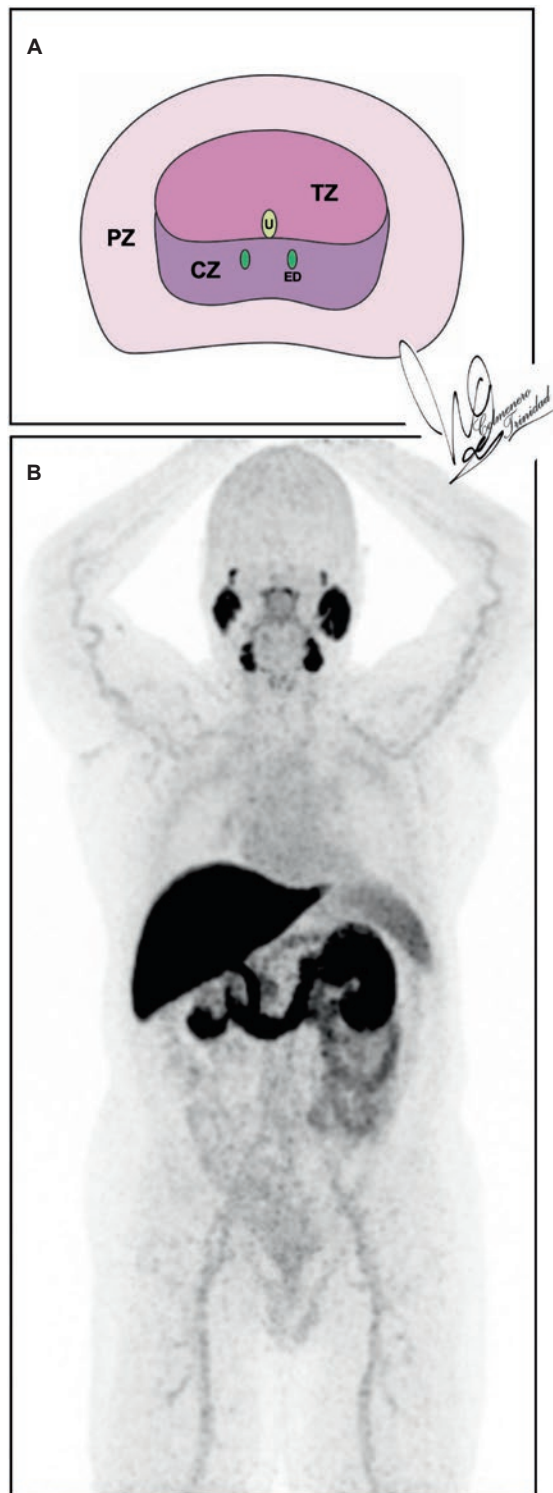


**Figure 1. A:** diagram of the anatomical zones of the prostate defined in the PSMA PET/CT expression patterns in the PRIMARY score. **B:** normal biodistribution of PSMA-PET on a maximum intensity projection (MIP) in lacrimal glands, parotid glands, liver, spleen, stellate ganglia, renal parenchyma, and bladder, mainly biliary excretion.

CZ: central zone; ED: ejaculatory ducts; PET/CT: positron emission tomography/computed tomography; PSMA: prostate-specific membrane antigen; PZ: peripheral zone; TZ: transition zone; U: urethra.



**Table 1.** Relationship between the intraprostatic tumor SULmax value and the PRIMARY score and the extent of PCa in primary staging

Description <sup>a</sup>	Total (n = 55)	Intraprostatic tumor SULmax, g/mL	p
PRIMARY score 2, n (%)	3 (5.0)	5.15 ± 0.54 (4.7, 4.9, 5.7)	ns
PRIMARY score 3, n (%)	1 (2.0)	7.11	-
PRIMARY score 4, n (%)	35 (64.0)	8.31 ± 1.92 (5.3, 8.5, 11.6)	ns
PRIMARY score 5, n (%)	16 (29.0)	22.64 ± 7.77 (13.3, 19.1, 35.9)	< 0.001
PCa local tumor and extent	Total (n = 55)	Intraprostatic tumor SULmax, g/mL	p
Intraprostatic tumor only, n (%)	24 (43.6)	11.49 ± 6.69 (4.7, 9.6, 31.2)	< 0.001
Intraprostatic tumor and pelvic lymph nodes, n (%)	9 (16.4)	15.17 ± 9.72 (5.9, 11.6, 32.4)	ns
Intraprostatic tumor and metastases (extrapelvic lymph nodes, bone, brain, and/or lung), n (%)	22 (40.0)	12.43 ± 8.73 (5.3, 9.0, 35.9)	< 0.001

All values are means ± SD (minimum, median, maximum). <sup>a</sup>Primary score 1 no patients.

[<sup>18</sup>F]: radionuclide fluor-18; PSMA: prostate-specific membrane antigen; 1007: ligand; ns: not significant; PCa: prostate cancer; PET/CT: positron emission tomography/computed tomography; SULmax: standardized uptake value maximum normalized to the lean body mass of PSMA.

disease spread with the Gleason score risk. Significance was defined as a p-value < 0.05. The analysis was performed with SPSS version 27.0 (IBM Corp., Armonk, NY, USA).

## RESULTS

Sixty-three PCa patients were eligible to participate. Eight men were excluded because a radiopharmaceutical other than [<sup>18</sup>F]PSMA-1007 was used. Fifty-five patients were included in the primary staging of PCa. The mean age was 65.1 ± 10.0 years. A mean of 9.50 millicuries (mCi) of [<sup>18</sup>F]PSMA was administered.

### *Relationship between the SULmax value and the PRIMARY score and the extent of PCa in primary staging*

The mean intraprostatic tumor SULmax value for score 2 was 5.15 ± 0.54 g/mL; for score 3, it was 7.11 g/mL; for score 4, the value was 8.31 ± 1.92 g/mL; and for score 5, it was 22.64 ± 7.77 g/mL (p < 0.001) (Table 1). The SULmax value of [<sup>18</sup>F]PSMA increased in direct association with the increase in the PRIMARY score (Figure 2). The SULmax value was 11.49 ± 6.69 g/mL in 24 (43.6%) patients with intraprostatic tumor (p < 0.001), while it was 15.17 ± 9.72 g/ml in 9 (16.4%) patients with intraprostatic tumor + pelvic lymph nodes. In contrast, in 23 (40.0%) patients with intraprostatic tumor + metastases

(extrapelvic lymph nodes, bone, brain, and/or lung), the SULmax value decreased to 12.43 ± 8.73 g/mL (p < 0.001).

Regarding the morphological local extension of the tumor, the distribution was 30 patients had miT2, tumor confined to the intraprostatic gland (focal or multifocal pattern); 20 patients had miT3, tumor involving the prostatic capsule and/or seminal vesicles. Only 5 patients had infiltration of adjacent structures such as the external anal sphincter, rectum, bladder, pelvic wall, or levator muscles (miT4) (Figure 3).

### *PSA value and its relationship with the PRIMARY score and extent of PCa in primary staging*

The PSA, in relation to the PRIMARY score, showed increased values for scores 2, 4, and 5 (Table 2). The PSA value for score 2 was 7.82 ± 0.87 ng/mL; scores 4 and 5 were 20.11 ± 27.22 ng/mL and 42.15 ± 48.15 ng/mL, respectively (p < 0.001). In one case with score 3, the PSA was 131.9 ng/mL. PSA values gradually increased depending on the extent of PCa and were 15.75 ± 26.35 ng/mL in patients with intraprostatic tumors (p < 0.001). The PSA increased to 20.93 ± 20.15 ng/mL in patients with pelvic lymph nodes. In the presence of metastases (extrapelvic lymph nodes, bone, brain, and/or lung), the PSA value was higher, with a mean of 43.97 ± 48.05 ng/mL (Figures 4, 5, and 6).

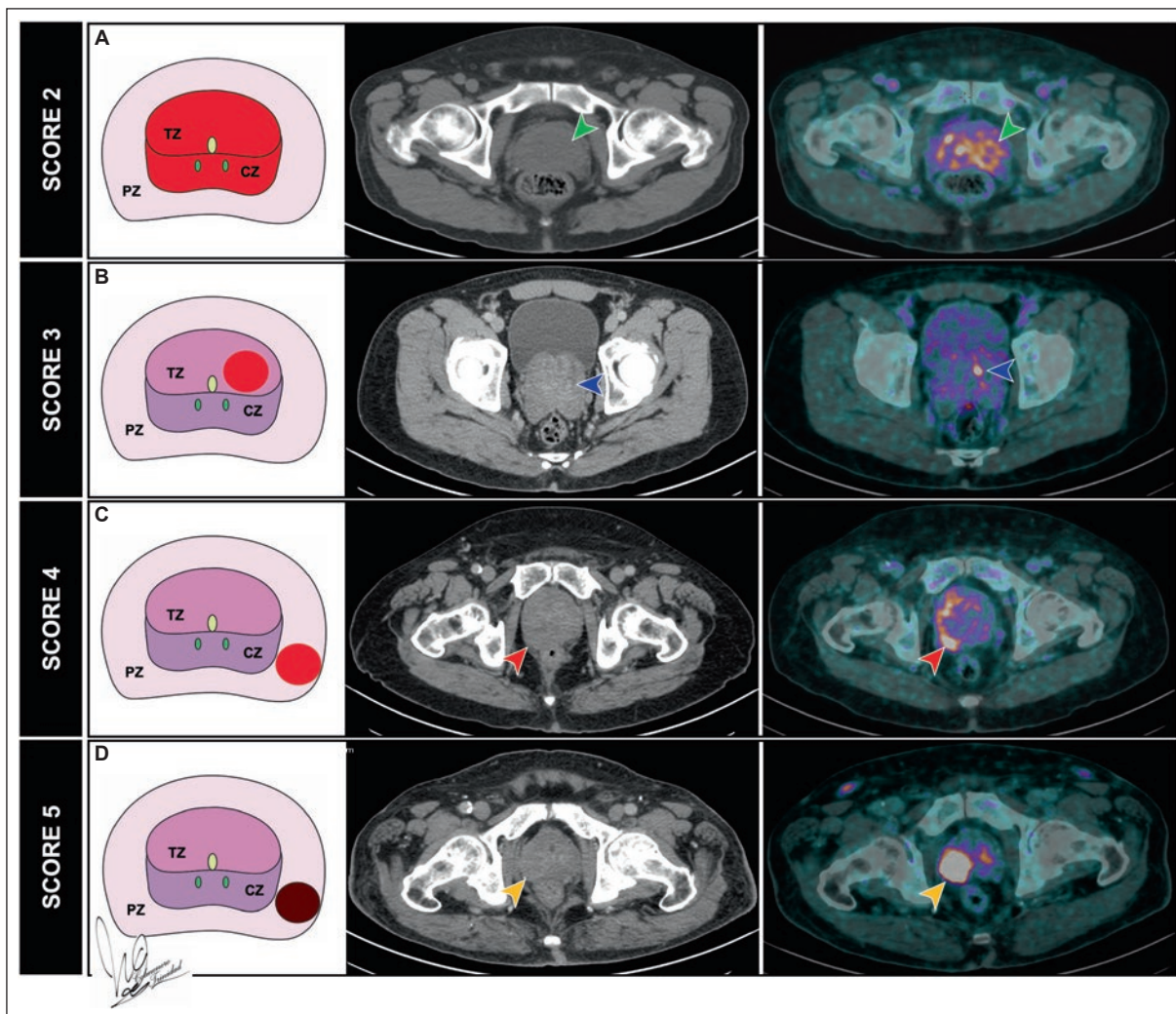


**Figure 2.** PSMA expression patterns of the PRIMARY score are shown in the diagram, CT, and PET/CT, axial projection. **A:** score 2, diffuse TZ activity or symmetric CZ activity that does not extend to the prostate margin on CT (green arrowheads). **B:** score 3, focal TZ activity that is visually twice as high as the background TZ activity (blue arrowheads). **C:** score 4, focal PZ activity, no minimum intensity (red arrowheads). **D:** score 5, PSMA SUVmax >12 (yellow arrowheads). In this study, SULmax was used to replace SUVmax with comparable values.

CT: computed tomography; CZ: central zone; PET/CT: positron emission tomography/computed tomography; PSMA: prostate-specific membrane antigen; PZ: peripheral zone; SULmax: standardized uptake value maximum normalized to the lean body mass concentration of the radiotracer [<sup>18</sup>F]PSMA-1007; SUVmax value: standardized uptake value maximum; TZ: transition zone.

Figure 7 shows the boxplot of PSA values in relation to the PRIMARY score and extent of PCa. PSA values were higher for PZ (score 4), and PZ /SULmax was > 12 (score 5) ( $p = 0.019$ ), and according to disease progression, the more advanced the disease, the higher the PSA values ( $p < 0.001$ ). PSA outlier values (127 ng/mL, 128 ng/mL, 131.9 ng/mL, and 174 ng/mL) are not shown in the figure.

A high number of scores of 4 and 5 was found in the PZ location of intraprostatic tumor with a focal pattern and/or SULmax > 12 g/mL, followed by intraprostatic tumor + extrapelvic lymph nodes and metastases (bone,

brain, and/or lung). Scores 2 and 3, located in CZ and TZ, had a symmetric and/or focal diffuse pattern with disease often confined to the prostate (Figure 8).

### Association of PRIMARY score with Gleason score risk in patients with PCa in primary staging

An [<sup>18</sup>F]PSMA expression pattern in PZ and/or SULmax > 12 g/mL and a low-risk Gleason score was found in 5 (71.4%) of 7 patients, while 46 (96.0%) of 48 patients had an intermediate- or high-risk Gleason

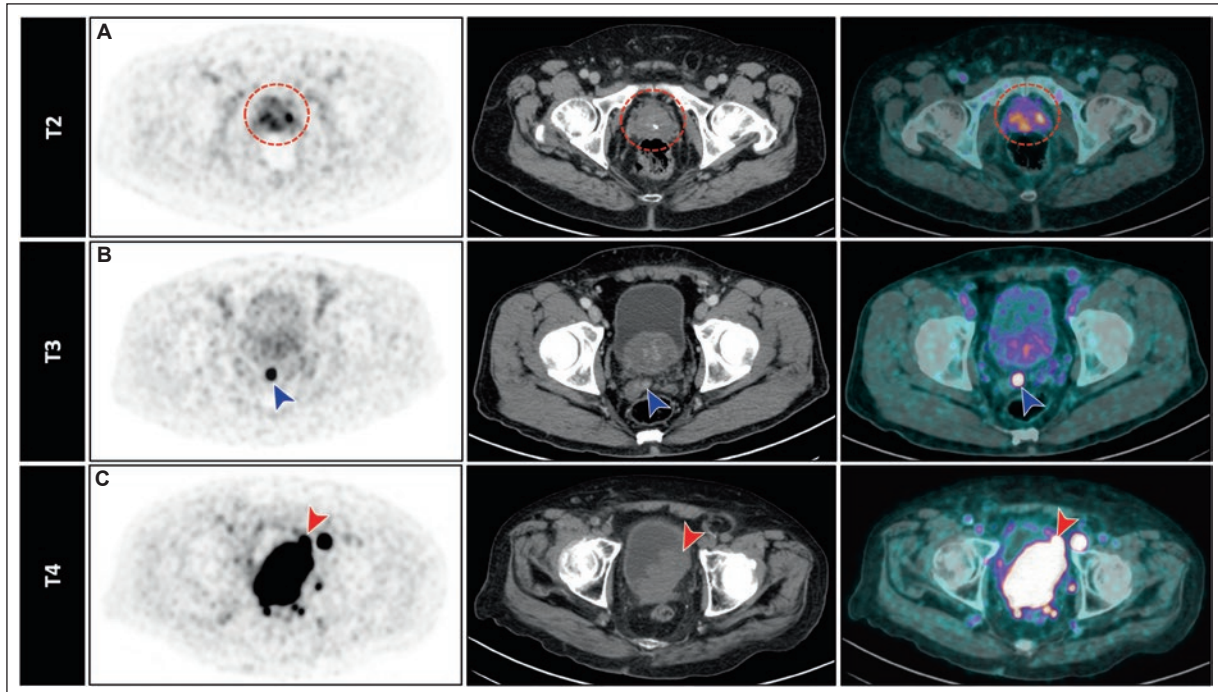


**Figure 3.** Intraprostatic tumor (miT) characteristics: maximum intensity images, CT and PET/ CT, axial projection. **A:** miT2, the tumor is confined to the prostate (dotted red circle). **B:** miT3, the tumor is not confined to the prostate but extends to the seminal vesicles (blue arrowheads). **C:** miT4, the tumor invades adjacent structures beyond the seminal vesicles (red arrowheads).  
 CT: computed tomography; miT: molecular tumor imaging; PET/CT: positron emission tomography/computed tomography.

**Table 2.** PSA value and its relationship with the PRIMARY score and extent of PCa in primary staging

Description <sup>a</sup>	Total (n = 55)	PSA, ng/mL	p
PRIMARY score 2, n (%)	3 (5.4)	7.82 ± 0.87 (6.9, 7.8, 8.6)	ns
PRIMARY score 3, n (%)	1 (1.8)	131.9	-
PRIMARY score 4, n (%)	35 (63.7)	20.11 ± 27.22 (3.9, 12.0, 128.0)	< 0.001
PRIMARY score 5, n (%)	16 (29.1)	42.15 ± 48.15 (3.3, 22.8, 174.0)	< 0.001
PCa local tumor and extent	Total (n = 55)	PSA, ng/mL	p
Intraprostatic tumor only, n (%)	24 (43.6)	15.75 ± 26.35 (3.3, 7.8, 131.9)	< 0.001
Intraprostatic tumor and pelvic lymph nodes, n (%)	9 (16.4)	20.93 ± 20.15 (4.9, 15.1, 69.0)	ns
Intraprostatic tumor and metastases (extrapelvic lymph nodes, bone, brain, and/or lung), n (%)	22 (40.0)	43.97 ± 48.05 (6.9, 20.2, 174.0)	ns

<sup>a</sup>Primary score 1 no patient. All values are means ± SD (minimum, median, maximum).

ns: not significant; PCa: prostate cancer; PSA: prostate-specific antigen.

score (Table 3). There were 2 (28.6%) of 7 patients with a [<sup>18</sup>F]PSMA expression pattern in CZ or TZ (score 2 and 3) with a low Gleason risk, while an intermediate or high Gleason score risk was found in two (4.0%) of

48 patients. A significant risk association of focal [<sup>18</sup>F] PSMA expression in the ZP or SULmax >12 g/mL had an intermediate or high-risk Gleason score (OR: 9.20, 95% CI 1.05 - 80.28).

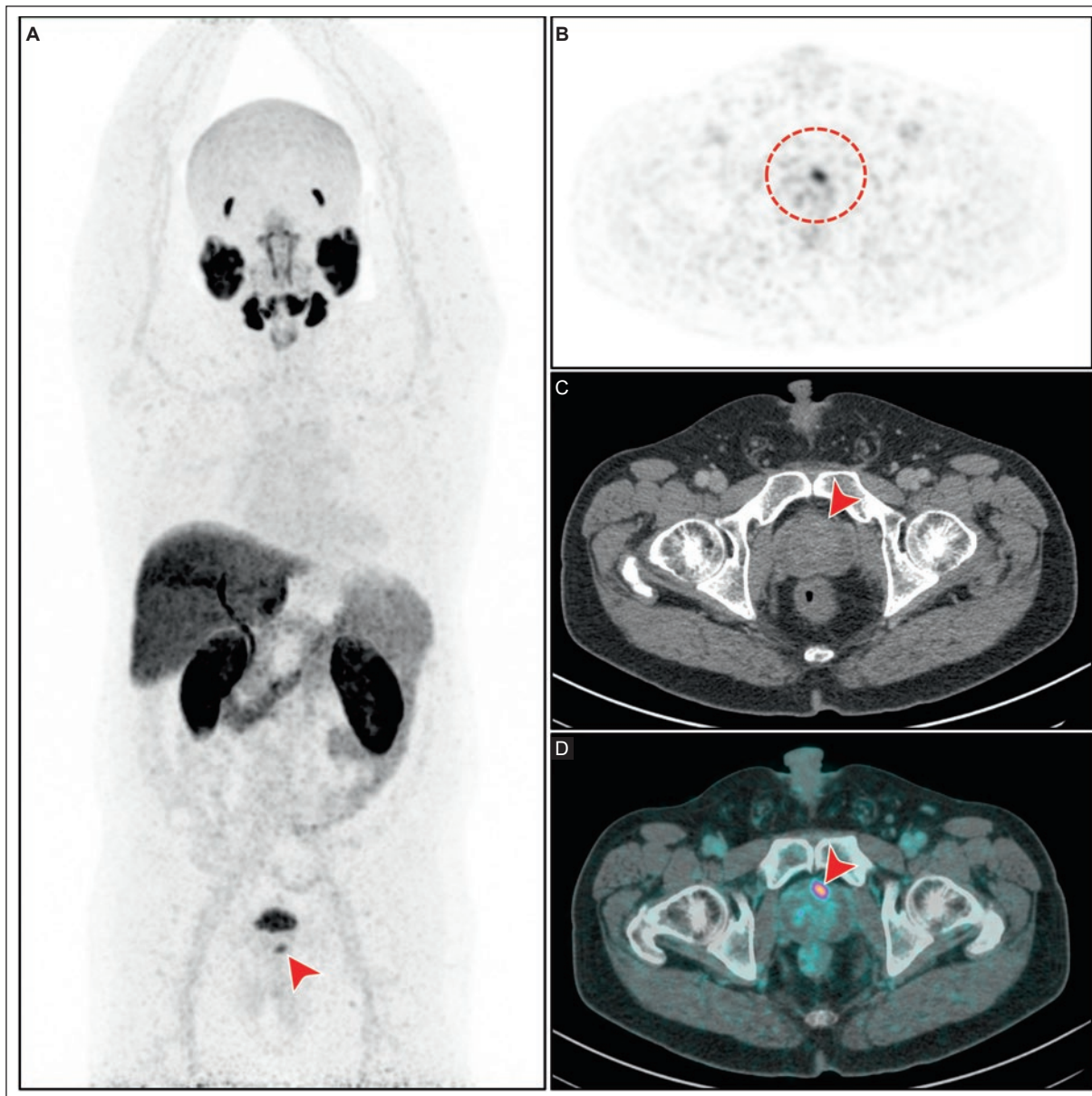


**Figure 4.** A 60-year-old man in primary staging of PCa. PSA 12.15 ng/mL. Gleason score 7 (3 + 4). **A:** a maximum intensity projection shows the physiologic distribution of the radiotracer with abnormal uptake of PSMA in the prostate (red arrowhead). No spread to pelvic lymph nodes or metastases was detected. **B:** PET, abnormal uptake of the intraprostatic PSMA tumor (dotted red circle). **C:** CT scan; PZ of the prostate shows a lobulated lesion with a partially defined border, homogeneous with enhancement, 15 x 9 mm (red arrowhead). **D:** [<sup>18</sup>F]PSMA PET/CT fusion, intraprostatic lesion in the PZ with focal PSMA uptake, SULmax value 8.68 g/mL (red arrowhead).

[<sup>18</sup>F]: radionuclide fluor-18; CT: computed tomography; PCa: prostate cancer; PET/CT: positron emission tomography/computed tomography; PSA: prostate-specific antigen (ng/mL); PSMA: prostate-specific membrane antigen; PZ: peripheral zone; SULmax: standardized uptake value maximum normalized to the lean body mass concentration of the radiotracer [<sup>18</sup>F]PSMA-1007.

### ***Risk association of local intraprostatic tumor and extent with the Gleason score in primary staging of PCa***

We found 6 (86.0%) of 7 patients with an intraprostatic tumor, with or without pelvic lymph nodes and a low-risk Gleason score, and 27 (57.2%) of 48 patients with

an intermediate- or high-risk Gleason score (Table 4). There was only one (14.0%) patient with an intraprostatic tumor and metastases (extrapelvic lymph nodes, bone, brain, and/or lung) and a low-risk Gleason score; in contrast, there were 21 (43.4%) patients with an intermediate- or high-risk Gleason score (OR 4.66, 95% CI, 0.52-41.80).

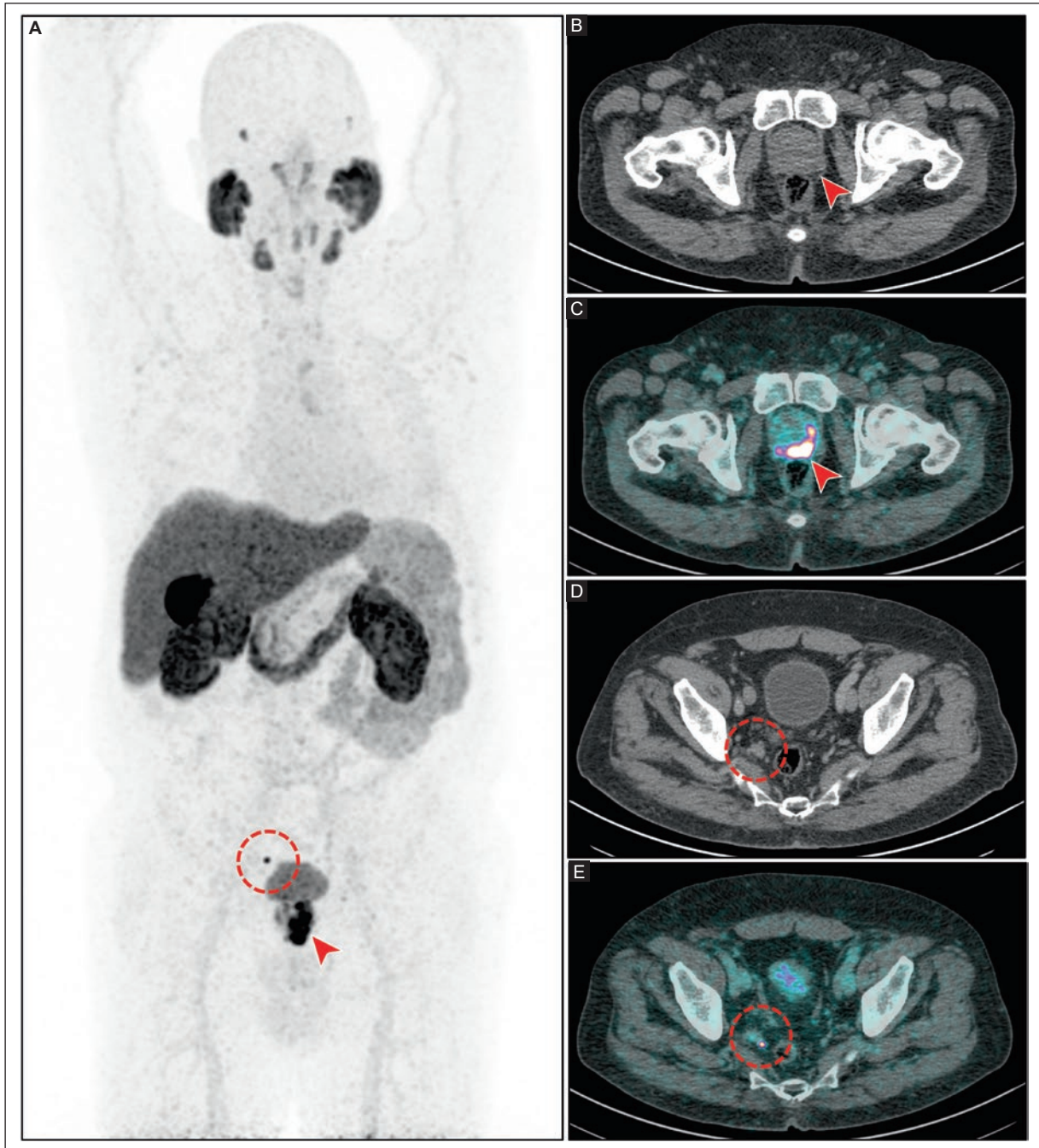


**Figure 5.** An 80-year-old man in primary staging of PCa. PSA 31 ng/mL. Gleason score of 7 (4 + 3). **A:** maximum intensity projection showing a physiologic distribution of the radiotracer with abnormal PSMA uptake in the prostate (red arrowhead) and pelvic lymph nodes (dotted red circle). No spread to extrapelvic lymph nodes or metastases (bone, brain, or lung) was detected. **B:** CT scan; a multilobular lesion in the PZ of the prostate with a poorly defined margin, homogeneous with enhancement, 12 x 8 mm (red arrowhead). **C:** [<sup>18</sup>F]PSMA PET/CT fusion, intraprostatic tumor in the PZ with abnormal focal uptake and a SULmax value of 28.76 g/mL (red arrowhead). **D:** CT, oval, 7 mm pelvic lymph node of the right internal iliac chain (dotted red circle). **E)** [<sup>18</sup>F]PSMA PET/CT fusion; abnormal PSMA uptake in the right inner iliac chain (dotted red circle).

[<sup>18</sup>F]: radionuclide fluor-18; CT: computed tomography; PCa: prostate cancer; PET/CT: positron emission tomography/computed tomography; PSA: prostate-specific antigen (ng/mL); PSMA: prostate-specific membrane antigen; PZ: peripheral zone; SULmax: standardized uptake value maximum normalized to lean body mass of PSMA.

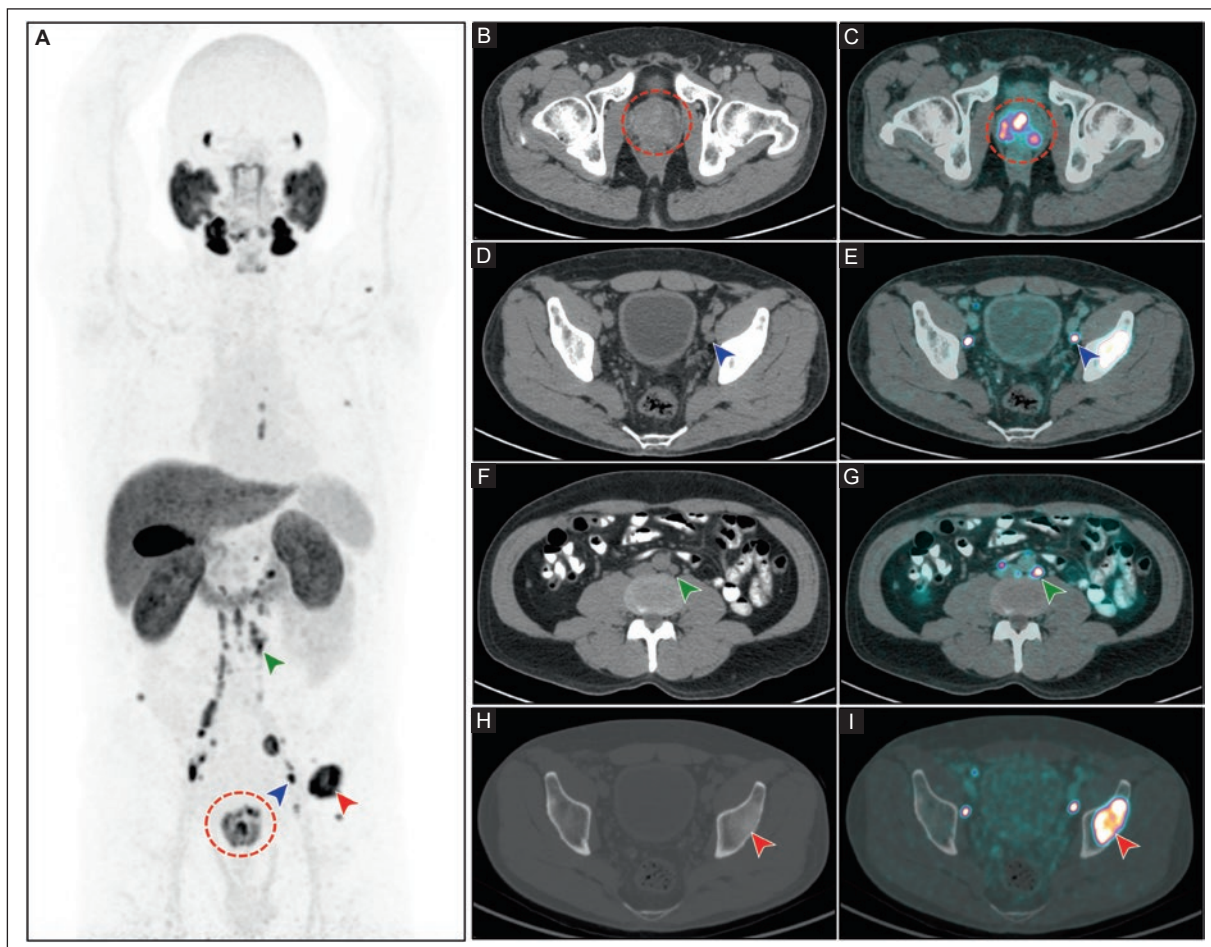


**Figure 6.** A 61-year-old man with PCa in primary staging. PSA 74 ng/mL with a Gleason score of 9 (5 + 4). **A:** maximum intensity projection with physiologic distribution of radiotracer showing abnormal PSMA uptake in the prostate (dotted red circle), multiple pelvic lymph nodes (blue arrowhead), multiple extrapelvic lymph nodes (green arrowhead), and bone metastases with disseminated pattern (red arrowhead). **B:** CT: multiple hyperdense lesions are observed in the prostate apex (PZ) with a defined border and homogeneous content, with the largest measuring 16 mm (dotted red circle). **C:** [<sup>18</sup>F]PSMA PET/CT fusion, intraprostatic tumor in the apex (PZ) with abnormal multifocal uptake, SULmax 18.91 g/mL (dotted red circle). **D:** CT, multiple (> 2) pelvic lymph nodes of the inner and outer iliac chains, round margin, 9 mm in size (blue arrowhead). **E:** [<sup>18</sup>F]PSMA PET/CT fusion, abnormal PSMA uptake in multiple (> 2) pelvic lymph nodes at the inner and outer iliac chains (blue arrowhead). **F:** CT, lymph nodes in the retroperitoneum (paraortic and paracaval), measuring 7 mm (green arrowhead). **G:** [<sup>18</sup>F]PSMA PET/CT fusion, abnormal focal uptake in the retroperitoneum, paraortic and paracaval (green arrowhead). **H:** CT, left acetabulum with osteoblastic lesion, cortical bone preserved (red arrowhead). **I:** [<sup>18</sup>F]PSMA PET/CT fusion, abnormal focal uptake of an osteoblastic lesion in the left acetabulum (red arrowhead). [<sup>18</sup>F]: radionuclide fluor-18; CT: computed tomography; PCa: prostate cancer; PET/CT: positron emission tomography/computed tomography; PSA: prostate-specific antigen (ng/mL); PSMA: prostate-specific membrane antigen; PZ: peripheral zone; SULmax: standardized uptake value maximum normalized to the lean body mass of PSMA (g/mL).

## DISCUSSION

In this study, the SULmax was associated with the expression patterns of [<sup>18</sup>F]PSMA-1007 PET/CT according to the PROMISE-V2 PRIMARY score in PCa patients in primary staging. The highest SULmax was associated with PRIMARY scores 4 and 5, increased intensity of [<sup>18</sup>F]PSM-1007 PET/CT expression, and involvement of the PZ. This study is the first that demonstrates the association between the highest SULmax of [<sup>18</sup>F]PSMA

PET/CT and PCa confined to the pelvic cavity; however, the SULmax decreased in patients with distant lymph nodes and metastases at other sites.

A post-hoc analysis showed that the increase in SUVmax was associated with an increased probability of malignancy only in focal patterns of the PRIMARY score predicting clinically significant (cs) PCa<sup>9</sup>. Our SULmax values were comparable to the SUVmax previously reported by other authors identifying intraprostatic neoplastic processes. However, the value obtained

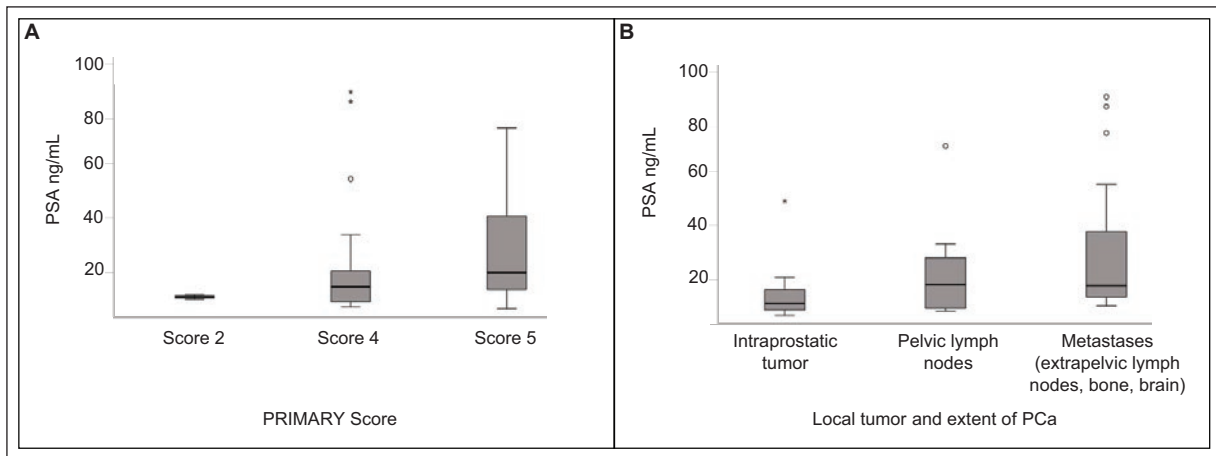


**Figure 7.** Boxplot of PSA values in relation to PRIMARY score and local tumor and extent of PCa. **A:** scores 4 and 5 were associated with a high PSA value ( $p < 0.001$ ). **B:** the greater the local tumor involvement and extent of PCa, the higher the PSA values. Intraprostatic tumor showed statistical significance ( $p \leq 0.001$ ).

PCa: prostate cancer; PSA: prostate-specific antigen (ng/mL).

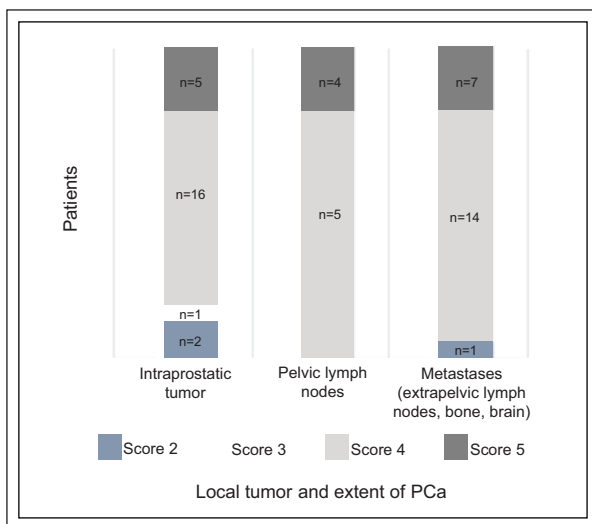


**Figure 8.** The overall distribution between PRIMARY score and local tumor involvement and extent of PCa. Numbers within bars are the patients per PRIMARY score category. PRIMARY scores 2 and 3 mostly showed disease confined to the prostate with a low frequency of CZ and TZ involvement. The highest prevalence was found for PRIMARY scores 4 and 5 with intraprostatic tumor, followed by metastases (extrapelvic lymph nodes, bone, brain and/or lung).

CZ: central zone; PCa: prostate cancer; TZ: transition zone.

of the SULmax suggests a better approximation of the cutoff parameter according to the prostatic involvement zone, which is the first reference site where PCa appears; the CZ and TZ showed lower SULmax values. In addition, the PRIMARY score integrates qualitative and quantitative assessment based on the anatomic zone (PZ, CZ, or TZ), pattern (diffuse or focal), and the

SUVmax. Emmett et al.<sup>8</sup> compared MRI and [<sup>18</sup>F]PSMA PET/CT, individually and in combination, for the detection of csPCa with histologic confirmation in a prospective, multicenter study. The combination of MRI + PSMA uptake increased sensitivity and positive predictive value compared to MRI alone. An SUVmax of 12 g/mL showed 100% specificity and negative predictive value NPV for csPCa, independent of MRI findings. Guo et al.<sup>19</sup> validated the diagnostic performance of the PRIMARY score in combination with MRI in detecting csPCa in a retrospective cohort study of 431 men who underwent [<sup>68</sup>Ga]PSMA PET/CT and MRI. PRIMARY score + MRI increased sensitivity (96.0% vs. 87.9%,  $p < 0.001$ ) and NPV (91.5% vs. 79.1%,  $p < 0.001$ ). The performance of the PRIMARY score was superior to MRI in detecting csPCa. In our study, The PRIMARY score showed that the expression of PSMA uptake in the local tumor was highest in the pattern of focal involvement in the peripheral zone (PZ) as long as the disease was confined to the pelvis.

PSMA is a transmembrane glycoprotein on the cell surface expressed in >90% of PCa cases. Higher-grade PCa variants, metastatic disease, and castration-resistant PCa are associated with increased expression of the PSMA receptor, leading to an increase in SULmax value<sup>8,20</sup>. Our study found a higher SULmax value was found in PCa confined to the pelvic cavity (intraprostatic tumor with or without local lymph node spread). Once extrapelvic spread (metastasis) occurred, the SULmax value at the intraprostatic level showed decreasing values. In a retrospective study, Koerber et al.<sup>13</sup> examined

**Table 3.** Risk association of PRIMARY score with Gleason score risk in patients with PCa in primary staging

Pattern	Low-risk Gleason score (≤ 6) Total (n = 7)	Intermediate/high-risk Gleason score (≥ 7) Total (n = 48)	OR (95% CI)
PZ/SULmax >12 g/mL (PRIMARY score 4 and 5) <sup>a</sup> , n (%)	5 (71.4)	46 (96.0)	9.20 (1.05-80.28)
CZ/TZ (PRIMARY score 2 and 3) <sup>b</sup> , n (%)	2 (28.6)	2 (4.0)	

<sup>a</sup>High-risk group with PZ and/or intense maximal PSMA uptake (SULmax > 12) (Score 4 and 5); <sup>b</sup>Low-risk group, with uptake in the CZ and/or TZ with diffuse or focal distribution (score 2 and 3); p = 0.04.

CI: confidence interval; CZ: central zone; OR: odds ratio; PCa: prostate cancer; PZ: peripheral zone; SULmax: standardized uptake value maximum normalized to lean body mass of PSMA; TZ: transition zone.

**Table 4.** Risk association of local intraprostatic tumor and extent with Gleason score in primary staging of PCa

PCa local tumor and extent	Low-risk Gleason score (≤ 6) Total (n = 7)	Intermediate/high-risk Gleason score (≥ 7) Total (n = 48)	OR (95% CI)
Intraprostatic tumor with or without pelvic lymph nodes, n (%)	6 (86.0)	27 (56.2)	4.66 (0.52-41.80)
Intraprostatic tumor and metastases (extrapelvic lymph nodes, bone, brain, and/or lung), n (%)	1 (14.0)	21 (43.8)	

p = 0.16. PCa: prostate cancer; OR: odds ratio; CI: confidence interval.

335 men with biopsy-proven PCa and PSMA-PET/CT for primary staging. They analyzed and correlated the SUVmax value of the intraprostatic malignant lesion with the number and location of metastases. They found a statistically significantly higher SUVmax value in men with metastatic disease than in the cohort without distant metastases (mean 16.1 g/mL vs. 11.2 g/mL, p < 0.001) with a cutoff value of 11.9 g/mL for SUVmax and a sensitivity and specificity of 76.0% and 58.4%, respectively. These findings may be related to the increased tumor volume of the disease, with the tumor burden being expressed to a greater extent in some of the metastatic lesions and acting as a sequestering lesion for [<sup>18</sup>F]PSMA uptake. The SULmax is probably higher and progressive according to the uptake measured at the metastatic lesion (extrapelvic lymph nodes, bone, brain, lung), as expression may act through the sequestration phenomenon of the radiopharmaceutical (PSMA) so that the SULmax value of the intraprostatic tumor is non-specific once extrapelvic dissemination is detected. The results reported by other authors are comparable to ours. Our study determined a mean SULmax value of 12.43 g/ml in patients with intraprostatic tumors and metastases. The intraprostatic SULmax value seems to be a promising parameter for predicting distant metastatic disease.

Several parameters can predict the severity of PCa, such as the PSA value and the Gleason score. In intraprostatic lesions, the intensity of PSMA ligand uptake in PET has been shown to correlate with tumor aggressiveness.

Bostwick et al.<sup>21</sup> showed that the greater the extent and intensity of PSMA expression, the higher the Gleason score. Topuz et al.<sup>11</sup>, in a retrospective study of 139 patients between different PCa risk groups concerning metastases and [<sup>68</sup>Ga]PSMA uptake patterns in primary staging of PCa, reported that SUVmax values correlated significantly with the Gleason score risk group and pre-treatment PSA values. Bilobar involvement of PSMA in the prostate, a Gleason score of 8 or more, and a PSA value of 20 ng/mL or more were independent predictors of metastasis. In a retrospective study of 147 patients, the ability of [<sup>68</sup>Ga]PSMA PET/CT to differentiate between intermediate- and high-risk PCa was assessed. The authors reported that PSMA uptake measured by SUVmax was closely related to the Gleason score<sup>20</sup>. Our mean value of SULmax was directly related to the PSA value and the Gleason score risk group. PCa with an intermediate and high Gleason score had a higher risk of intraprostatic tumor affecting PZ and a higher risk of extrapelvic spread of disease. The PRIMARY score showed a significant association with the PSA level and an association with the Gleason score. The relationship between the highest SULmax values and intermediate- and high-risk Gleason score was comparable to previous SUVmax reports<sup>8,12,14,20-26</sup>.

The strengths of our study relate to the fact that all included patients had a histopathologically confirmed diagnosis of PCa with a low, intermediate, or high-risk Gleason score. We calculated the SULmax using a workstation and automated software. On the other hand,



the radionuclide in our study is based on [<sup>18</sup>F]PSMA with a longer half-life (~2 hours) and high-quality images. The limitations of our study were related to the retrospective design, small sample size, and single institution. In the present study, the analysis to characterize the affected anatomical areas was based on the expression pattern of PSMA and CT images. However, the gold standard for identifying prostate areas is MRI, which could be in line with the preamble of PET/MRI and a useful reference for patients who cannot undergo MRI and/or in locations that cannot compare the diagnostic approach with MRI. On the other hand, the SULmax of the metastases was not calculated for comparison with the SULmax of the intraprostatic tumor.

## CONCLUSION

In our study, the SULmax value was associated with the PROMISE-V2 PRIMARY score in patients with PCa in primary staging according to the affected anatomic zone (PZ, CZ, or TZ), expression patterns, and SULmax > 12 g/mL. Expression of PSMA uptake in the local tumor was highest for the pattern of focal involvement in the ZP as long as the disease was confined to the pelvic cavity (intraprostatic tumor with or without pelvic lymph nodes). We also showed the risk association according to PSA levels and the Gleason score for the PRIMARY score and PCa extent, respectively.

## Acknowledgments

The authors thank Professor Ana M. Contreras-Navarro for her guidance in preparing and writing this scientific paper. This original research in the Radiology Specialty field was an awarded thesis at the Segunda Convocatoria Nacional 2023-2024, “Las Mejores Tesis para Publicar en el JMEXFRI.”

## Funding

This research received no external funding.

## Conflicts of interest

The authors declare that they have no conflicts of interest.

## Ethical disclosures

**Protection of individuals.** This study complied with the Declaration of Helsinki (1964) and subsequent amendments.

**Confidentiality of data.** The authors declare they followed their center’s protocol for sharing patient data.

**Right to privacy and informed consent.** Informed consent was not required for this observational study of information collected during routine clinical care.

**Use of artificial intelligence.** The authors did not use generative artificial intelligence to prepare this manuscript and/or create tables, figures, or figure legends.

## REFERENCES

1. Farolfi A, Calderoni L, Mattana F, Mei R, Telo S, Fanti S, et al. Current and Emerging Clinical Applications of PSMA PET Diagnostic Imaging for Prostate Cancer. *J Nucl Med.* 2021;10;62(5):596-604. doi: 10.2967/jnumed.120.257238.
2. Jochumsen MR, Bouchelouche K. PSMA PET/CT for Primary Staging of Prostate Cancer - An Updated Overview. *Semin Nucl Med.* 2024;54(1):39-45. doi: 10.1053/j.semnucmed.2023.07.001.
3. Wallitt KL, Khan SR, Dubash S, Tam HH, Khan S, Barwick TD. Clinical PET Imaging in Prostate Cancer. *Radiographics.* 2017;37(5):1512-1536. doi: 10.1148/rg.2017170035.
4. García FO; Medina SS. Radiotracers Used in Nuclear Medicine for Prostate Cancer Diagnosis and Follow-Up. *Gaceta Mex Oncol.* 2017;16(1):41-48. doi: 10.24875/j.gamo.17000007.
5. Azmi NHM, Suppiah S, Liong CW, Noor NM, Said SM, Hanafi MH, et al. Reliability of standardized uptake value normalized to lean body mass using the liver as a reference organ, in contrast-enhanced 18F-FDG PET/CT imaging. *Radiat Phys Chem.* 2018;147:35-39.
6. Aksu A, Çapa Kaya G. Is SUV Corrected for Lean Body Mass Superior to SUV of Body Weight in <sup>68</sup>Ga-PSMA PET/CT? *Mol Imaging Radionucl Ther.* 2021;15;30(3):144-149. doi: 10.4274/mirt.galenos.2021.59254.
7. Gafita A, Calais J, Franz C, Rauscher I, Wang H, Roberstson A, et al. Evaluation of SUV normalized by lean body mass (SUL) in <sup>68</sup>Ga-PSMA11 PET/CT: a bicentric analysis. *EJNMMI Res.* 2019;9(1):103. doi:10.1186/s13550-019-0572-z.
8. Emmett L, Buteau J, Papa N, Moon D, Thompson J, Roberts MJ, et al. The Additive Diagnostic Value of Prostate-specific Membrane Antigen Positron Emission Tomography Computed Tomography to Multiparametric Magnetic Resonance Imaging Triage in the Diagnosis of Prostate Cancer (PRIMARY): A Prospective Multicentre Study. *Eur Urol.* 2021;80(6):682-689. doi: 10.1016/j.eururo.2021.08.002.
9. Emmett L, Papa N, Buteau J, Ho B, Liu V, Roberts M, et al. The PRIMARY Score: Using Intraprostatic <sup>68</sup>Ga-PSMA PET/CT Patterns to Optimize Prostate Cancer Diagnosis. *J Nucl Med.* 2022;63(11):1644-1650. doi: 10.2967/jnumed.121.263448.
10. Jiao J, Kang F, Zhang J, Quan Z, Wen W, Zhao X, et al. Establishment and prospective validation of an SUV<sub>max</sub> cutoff value to discriminate clinically significant prostate cancer from benign prostate diseases in patients with suspected prostate cancer by <sup>68</sup>Ga-PSMA PET/CT: a real-world study. *Theranostics.* 2021;25;11(17):8396-8411. doi: 10.7150/thno.58140.
11. Topuz ÖV, Aksu A, Erinc SR, Tamam MÖ. Correlations of <sup>68</sup>Ga-PSMA PET/CT in the initial staging of prostate cancer patients. *Hell J Nucl Med.* 2021;24(1):60-65. doi: 10.1967/s002449912307.
12. Fendler WP, Schmidt DF, Wenter V, Thierfelder KM, Zach C, Stief C, et al. <sup>68</sup>Ga-PSMA PET/CT Detects the Location and Extent of Primary Prostate Cancer. *J Nucl Med.* 2016;57(11):1720-1725. doi: 10.2967/jnumed.116.172627.
13. Koerber SA, Boesch J, Kratochwil C, Schlamp I, Ristau J, Winter E, et al. Predicting the Risk of Metastases by PSMA-PET/CT-Evaluation of 335 Men with Treatment-Naïve Prostate Carcinoma. *Cancers (Basel).* 2021;13(7):1508. doi: 10.3390/cancers13071508.
14. Manafi-Farid R, Ranjbar S, Jamshidi Araghi Z, Pilz J, Schweighofer-Zwink G, Pirich C, et al. Molecular Imaging in Primary Staging of Prostate Cancer Patients: Current Aspects and Future Trends. *Cancers (Basel).* 2021;13(21):5360. doi: 10.3390/cancers13215360.
15. Eiber M, Herrmann K, Calais J, Hadaschik B, Giesel FL, Hartenbach M, et al. Prostate Cancer Molecular Imaging Standardized Evaluation (PROMISE): Proposed miTNM Classification for the Interpretation of PSMA-Ligand PET/CT. *J Nucl Med.* 2018;59(3):469-478. doi: 10.2967/jnumed.117.198119.
16. Seifert R, Emmett L, Rowe SP, Herrmann K, Hadaschik B, Calais J, et al. Second Version of the Prostate Cancer Molecular Imaging Standardized Evaluation Framework Including Response Evaluation for Clinical Trials (PROMISE V2). *Eur Urol.* 2023;83(5):405-412. doi: 10.1016/j.eururo.2023.02.002.

17. Ali H, Rashid-UI-Amin S, Hai A. Standardised Uptake Value in Organ Confined Prostate Cancer in 68-Ga- Prostate-Specific Membrane Antigen Positron Emission Tomography-Computed Tomography Scan and its Correlation with Prostate Specific Antigen Level and Gleason Score. *J Cancer Allied Spec.* 2023;13;9(2):529. doi: 10.37029/jcas.v9i2.519.
18. Epstein JI, Egevad L, Amin MB, Delahunt B, Srigley JR, Humphrey PA; Grading Committee. The 2014 International Society of Urological Pathology (ISUP) Consensus Conference on Gleason Grading of Prostatic Carcinoma: Definition of Grading Patterns and Proposal for a New Grading System. *Am J Surg Pathol.* 2016;40(2):244-252. doi: 10.1097/PAS.0000000000000530.
19. Guo S, Kang F, Ma S, Jiao J, Ren J, Wang J, et al. The PRIMARY Score: Diagnostic Performance and Added Value Compared With MRI in Detecting Clinically Significant Prostate Cancer. *Clin Nucl Med.* 2024;1;49(1):37-44. doi: 10.1097/RLU.0000000000004951.
20. Yi N, Wang Y, Zang S, Yang L, Liu H, Sun H, et al. Ability of <sup>68</sup>Ga-PSMA PET/CT SUVmax to differentiate ISUP GG2 from GG3 in intermediate-risk prostate cancer: A single-center retrospective study of 147 patients. *Cancer Med.* 2023;12(6):7140-7148. doi: 10.1002/cam4.5516.
21. Bostwick DG, Pacelli A, Blute M, Roche P, Murphy GP. Prostate specific membrane antigen expression in prostatic intraepithelial neoplasia and adenocarcinoma: a study of 184 cases. *Cancer.* 1998;82(11):2256-2261. doi: 10.1002/(sici)1097-0142(19980601)82:11<2256::aid-cnrcr22>3.0.co; 2-s.
22. Demirci E, Kabasakal L, Şahin OE, Akgün E, Gültekin MH, Doğanca T, et al. Can SUVmax values of Ga-68-PSMA PET/CT scan predict the clinically significant prostate cancer? *Nucl Med Commun.* 2019;40(1):86-91. doi: 10.1097/MNM.0000000000000942.
23. Bagheri H, Mahdavi SR, Geramifar P, Neshasteh-Riz A, Sajadi Rad M, Dadgar H, et al. An Update on the Role of mpMRI and <sup>68</sup>Ga-PSMA PET Imaging in Primary and Recurrent Prostate Cancer. *Clin Genitourin Cancer.* 2024;22(3):102076. doi: 10.1016/j.clgc.2024.102076.
24. Emmett L, Papa N, Counter W, Calais J, Barbato F, Burger I, et al. Reproducibility and Accuracy of the PRIMARY Score on PSMA PET and of PI-RADS on Multiparametric MRI for Prostate Cancer Diagnosis With a Real-World Database. *J Nucl Med.* 2024;2;65(1):94-99. doi: 10.2967/jnumed.123.266164.
25. Heetman JG, Paulino Pereira LJ, Kelder JC, Soeterik TFW, Wever L, Lavalaye J, et al. The additional value of 68Ga-PSMA PET/CT SUVmax in predicting ISUP GG $\geq$ 2 and ISUP GG $\geq$ 3 prostate cancer in biopsy. *Prostate.* 2024;84(11):1025-1032. doi: 10.1002/pros.24716.
26. Rahbar K, Weckesser M, Huss S, Semjonow A, Breyholz HJ, Schrader AJ, et al. Correlation of Intraprostatic Tumor Extent with [<sup>68</sup>Ga]-PSMA Distribution in Patients with Prostate Cancer. *J Nucl Med.* 2016;57(4):563-567. doi: 10.2967/jnumed.115.169243.

# US duplex findings of deep chronic venous insufficiency of the lower limbs in 700 Mexican patients

Mauricio Figueroa-Sanchez<sup>1,2,3,\*</sup>  and Roberto Hernandez-Juarez<sup>4,5</sup> 

<sup>1</sup>Radiology and Imaging Department, Antiguo Hospital Civil of Guadalajara “Fray Antonio Alcalde”, Guadalajara, Jalisco; <sup>2</sup>University Center of Health Sciences, Universidad of Guadalajara, Guadalajara, Jalisco; <sup>3</sup>Laboratorio Vascular S.C., Guadalajara, Jalisco; <sup>4</sup>Department of Radiology and Imaging, Angeles Leon Hospital, Leon, Guanajuato; <sup>5</sup>Mexican Faculty of Medicine, La Salle University, Mexico City, Mexico

## ABSTRACT

**Introduction:** The ultrasound (US) findings of deep chronic venous insufficiency (CVI) have been insufficiently addressed. This study evaluated the US duplex findings of the deep venous system in Mexican patients with clinically suspected CVI referred by angiologists. **Materials and Methods:** This cross-sectional study was conducted in patients over 18 years of age with suspected CVI referred by angiologists. The complete protocol included the following US modalities: grayscale, duplex Doppler, color Doppler, power Doppler, and B-flow. The US examination focused on the deep venous system, evaluating parameters such as diameter, compressibility, patency, flow direction, and the presence of venous reflux. **Results:** We examined 956 limbs from 700 patients with suspected CVI; 485 (69.3%) were women, and 215 (30.7%) were men. Right unilateral US duplex was performed 178 (25.4%), left unilateral in 265 (37.9%), and bilateral in 257 (36.7%). Deep CVI was found in 146 (30.2%) of 485 women and 75 (34.9%) of 215 men, mainly affecting the femoral vein, with a higher prevalence in the left limb in both sexes. No significant differences in the vein diameter were found in patients with or without CVI. Secondary CVI was more common and mainly affected the left limb. **Conclusion:** In this study, deep CVI was found in about 1 in 3 patients with clinically suspected CVI, with a higher prevalence in men than in women. Secondary CVI was more prevalent. This study of Mexican patients is the first to describe US duplex findings in deep CVI.

**Keywords:** Deep chronic venous insufficiency. Ultrasound. Lower limbs.

## INTRODUCTION

Chronic venous insufficiency (CVI) of the lower limbs includes a wide range of morphological and functional abnormalities. Venous hypertension due to deficient venous return caused by valve damage or obstruction generates venous reflux<sup>1</sup> in CVI, manifested clinically with symptoms such as pain, limb edema, and recurrent ulcers<sup>2</sup>. Ultrasound (US) duplex is the main imaging modality that assesses lower limb veins, providing essential anatomical and hemodynamic information<sup>3-5</sup>. For accurate results, the vascular radiologist must thoroughly understand normal venous anatomy, including

its multiple variations and hemodynamic aspects, and a structured US duplex protocol<sup>1,6</sup>. The vascular radiologist must provide a complete venous map of the lower limbs, including a structured report of patency, the presence or absence of thrombosis, and the sites and degrees of venous reflux<sup>1,7</sup>.

Venous reflux is the most common abnormal finding on US duplex examination of the lower limbs. It is a dominant feature in the progression of venous insufficiency and ulceration in patients with CVI<sup>5,8</sup>. A previous report of Mexican patients showed a complete description of US duplex findings of the perforating, superficial,

### \*Corresponding author:

Mauricio Figueroa-Sanchez  
E-mail: [figueroa\\_sanchez@hotmail.com](mailto:figueroa_sanchez@hotmail.com)  
2696-8444 / © 2024 Federación Mexicana de Radiología e Imagen, A.C. Published by Permanyer. This is an open access article under the CC BY-NC-ND (<https://creativecommons.org/licenses/by-nc-nd/4.0/>).

Received for publication: 10-04-2024  
Accepted for publication: 12-08-2024  
DOI: 10.24875/JMEXFRI.M24000090

Available online: 20-12-2024  
J Mex Fed Radiol Imaging. 2024;3(4):256-267  
[www.JMeXFRI.com](http://www.JMeXFRI.com)

deep, and reticular venous system in patients with CVI, highlighting their complexity<sup>5</sup>. The importance and frequency of deep venous reflux in CVI have been recognized in the last 20 years thanks to the development of duplex examination. However, US findings have been insufficiently addressed, and US duplex of the deep venous system in patients with deep CVI has received limited attention in the literature. This study assessed the US duplex findings of the deep venous system in Mexican patients with clinical suspicion of CVI referred by angiologists.

## MATERIAL AND METHODS

This cross-sectional study was conducted between March 2004 and July 2023 at the Vascular Laboratory in Guadalajara, Jalisco, Mexico. Patients of both sexes over 18 years of age, referred by angiologists with clinical suspicion of CVI and/or venous thrombosis of the lower limbs, were included. Pediatric patients and individuals with deep vein thrombosis secondary to neoplasms were excluded. Data were collected during routine medical care; therefore, informed consent was not required for data analysis and publication.

### *Study development and variables*

The patient's sex was recorded, and the following parameters of the deep venous system were examined: diameter, compressibility, patency, flow direction and velocity (cm/s), the presence of reflux in the common femoral vein, the femoral vein (proximal, middle, and distal segments), the deep femoral vein, the popliteal vein, and the anterior and posterior tibial veins. The complete study protocol was conducted according to a previously published technical note<sup>1</sup>.

### *Definitions*

*Chronic venous insufficiency (CVI)*: morphologic and functional abnormalities of the venous system, primarily affecting the lower limbs<sup>9</sup>.

*Primary CVI*: progressive degenerative condition leading to weakness of the lower limb vein walls, with no history or ultrasonographic evidence of previous vein thrombosis. This definition includes congenital CVI caused by the absence or inadequate development of venous leaflets<sup>10</sup>.

*Secondary CVI*: valvular insufficiency of the lower limbs associated with valvular damage due to a thrombotic, trauma, mechanical, thermal, or chemical etiology<sup>3,11</sup>.

*Deep vein thrombosis*: formation of a blood clot or thrombus in one or more veins of the deep venous system. It is part of the spectrum of venous thromboembolic diseases<sup>12</sup>.

*Acute deep vein thrombosis*: US Duplex shows endoluminal material anechoic in the first hours of the thrombotic event that evolves to hypoechoic and non-compressible with increasing vein diameter and absence of flow in color US Doppler and pulsed duplex Doppler<sup>5</sup>. The time of evolution is  $\leq 7$  days<sup>13</sup>.

*Subacute deep vein thrombosis*: US shows endoluminal material with a heterogeneous echotexture, predominantly hypoechoic, minimal compressibility with evidence of incipient recanalization and minimal flow on color Doppler, power Doppler, and B-flow<sup>5</sup>. The time of evolution is 1 to 6 weeks<sup>14</sup>.

*Chronic deep vein thrombosis*: endoluminal echogenic material with a heterogeneous echotexture, hyperechoic predominance, and variable flow on color Doppler, power Doppler, and B-flow. The morphology of the thrombus is highly variable. In late phases, it may show calcifications. The time of evolution is  $> 6$  weeks<sup>13</sup>.

*Recanalization*: color duplex US Doppler shows variable percent flow (10 to 90%) in the longitudinal and transverse views, and pulsed US duplex shows variable flow velocity<sup>5</sup>.

*Venous reflux*: retrograde flow associated with dilation during the Valsalva maneuver. A spectral inversion of  $> 1$ -second duration and a change from blue to red on color US Doppler<sup>15</sup>.

*Post-thrombotic syndrome*: US examination shows deep venous system reflux associated with echogenic endothelial thickening and echogenic thickening ( $> 1$  mm) of the leaflets, the presence of septa, echogenic bands, and/or echogenic endoluminal material with venous reflux<sup>5</sup>.

*Venous permeability*: capacity of the vein to allow free flow within it. Color and duplex Doppler show the endoluminal flow and direction (antegrade or retrograde)<sup>5</sup>.

*CVI Grades*: valve insufficiency severity was assessed according to reflux velocity as Grade 1: up to 10 cm/s; Grade 2: From 11 to 20 cm/s; and Grade 3: more than 20 cm/s<sup>5</sup>.

### *Image acquisition protocol*

The equipment used were an Aloka SSD4000S with 10- and 13-MHz linear transducers and 2-6-MHz convex transducers (Aloka Co., Tokyo, Japan) and a LOGIG E9 (GE Co., Wisconsin, USA) with 10-16-MHz

**Table 1.** Insufficient veins by US duplex in patients with deep CVI by sex and laterality of the limbs<sup>a</sup>

Description	Unilateral US duplex				Bilateral US duplex			
	Women		Men		Women		Men	
	Right (n = 23)	Left (n = 48)	Right (n = 21)	Left (n = 24)	Right (n = 59)	Left (n = 83)	Right (n = 22)	Left (n = 37)
Common femoral vein insufficiency, yes	9 (7.6)	26 (13.9)	13 (21.6)	12 (15.1)	15 (9.3)	29 (14.4)	12 (19.0)	18 (20.0)
Proximal third femoral vein insufficiency, yes	10 (8.4)	27 (14.5)	14 (23.3)	16 (20.2)	18 (11.2)	26 (12.9)	12 (19.0)	17 (18.8)
Middle femoral vein insufficiency, yes	11 (9.3)	27 (14.5)	14 (23.3)	14 (17.7)	14 (8.7)	19 (9.4)	7 (11.1)	10 (11.1)
Distal third femoral vein, insufficiency, yes	10 (8.4)	28 (15.0)	13 (21.6)	15 (18.9)	14 (8.7)	20 (9.9)	7 (11.1)	13 (14.4)
Deep femoral vein insufficiency, yes	6 (5.0)	15 (8.0)	11 (18.3)	11 (13.9)	9 (5.6)	16 (7.9)	4 (6.3)	11 (12.2)
Popliteal vein insufficiency, yes	11 (9.3)	24 (12.9)	10 (16.6)	14 (17.7)	11 (6.6)	16 (7.9)	7 (11.1)	11 (12.2)
Posterior tibialis vein insufficiency, yes	-	1 (0.5)	-	-	-	-	-	-
Peroneal vein insufficiency, yes	2 (1.6)	5 (2.69)	2 (3.3)	6 (7.5)	1 (0.6)	3 (1.4)	2 (3.1)	4 (4.4)

<sup>a</sup>Some patients had insufficiency in two or more veins or segments. The anterior tibial vein was not affected in any patient. Values are absolute frequencies and percentages.

CVI: chronic venous insufficiency; US: ultrasound.

and 3-6-MHz convex transducers. A comprehensive assessment of the deep venous system of the lower limbs was performed by US duplex using different modalities: grayscale, duplex Doppler, color Doppler, power Doppler, and B-flow examinations, following a previously described protocol<sup>1</sup>. All US duplex examinations were performed by a radiologist (MFS) with 30 years of experience in vascular US.

### Statistical analysis

Numerical variables were described with central tendency and dispersion (standard deviation [SD]) measures and categorical variables with absolute numbers and percentages. The association between categorical variables was assessed with the chi-square test. The difference in the means of numerical variables between two or more than two groups was analyzed using Student's t-test for unrelated samples or the ANOVA test. Bivariate analysis after ANOVA was performed using Tukey post-hoc analysis. A p-value <0.05 was considered statistically significant. The analysis was performed in SPSS version 28 (IBM Corp., Armonk, NY, USA).

## RESULTS

A total of 700 patients with clinically suspected CVI, referred by angiology specialists, were included;

485 (69.3%) were women and 215 (30.7%) were men. US duplex examination was performed unilaterally on the right limb in 178 (25.4%) patients, unilaterally on the left limb in 265 (37.9%) patients, and bilaterally in 257 (36.7%) patients, resulting in a total of 956 limbs examined. Deep CVI was detected in 221 (31.6%) of 699 patients. One patient was missed. One hundred and forty-six (30.2%) of 484 women and 75 (34.9%) of 215 men had deep CVI in one or more segments of the deep venous system. Femoral vein insufficiency was the most common finding in both sexes. Deep CVI was more common in the left limbs (n = 131, 61.5%) than in the right limbs (n = 82, 38.5%) in women. Deep CVI was also predominant in the left limbs (n = 61, 58.7%) than in the right limbs (n = 43, 41.3%) in men. Deep CVI was more commonly associated with left limbs in both sexes.

### Insufficient veins by US duplex in patients with deep CVI by sex and laterality of the limbs

The most common finding in the unilateral US duplex examination of women was insufficiency of the distal part of the femoral vein in the left limbs (n = 28, 15.0%) (Table 1). In the bilateral examination, insufficiency was most frequent in the common femoral vein of the left limbs (n = 29, 14.4%). In men, insufficiency was most frequent in the proximal part of the femoral vein of the

**Table 2.** Comparison of vein diameters by US duplex in 956 limbs with and without deep CVI by sex and laterality of the limbs<sup>a</sup>

Description	Women				Men			
	Right		Left		Right		Left	
	without CVI	with CVI	without CVI	with CVI	without CVI	with CVI	without CVI	with CVI
Common femoral vein, mm	17.5 ± 2.4	17.2 ± 3.3	17.0 ± 2.2	16.6 ± 2.7	19.7 ± 2.8	20.4 ± 4.3	19.7 ± 3.5	19.4 ± 4.1
Proximal third femoral vein, mm	13.4 ± 2.1	12.8 ± 2.3	13.1 ± 2.0	12.6 ± 2.4	14.4 ± 2.1	15.6 ± 3.8	14.1 ± 2.1	14.6 ± 2.8
Middle femoral vein, mm	12.5 ± 2.5	10.6 ± 2.1	11.6 ± 2.1	10.6 ± 2.7	12.9 ± 2.8	12.1 ± 3.0	11.8 ± 2.0	11.7 ± 3.1
Distal third femoral vein, mm	12.3 ± 2.2	10.8 ± 2.4	11.6 ± 2.1	10.4 ± 2.2	12.7 ± 2.4	12.0 ± 3.0	11.8 ± 2.2	12.0 ± 3.5
Deep femoral vein, mm	11.3 ± 2.4	10.8 ± 2.5	11.2 ± 2.0	10.5 ± 2.1	12.3 ± 2.1	12.4 ± 2.3	12.1 ± 2.1	12.3 ± 2.5
Popliteal vein, mm	11.4 ± 2.4	11.5 ± 2.3	11.3 ± 2.1	10.7 ± 2.2	12.3 ± 2.7	13.3 ± 3.7	12.2 ± 2.2	12.2 ± 3.3

<sup>a</sup>Includes unilateral and bilateral US duplex. All values are means and standard deviations. CVI: chronic venous insufficiency; US: ultrasound.

left limb on unilateral US duplex examination (n = 16, 20.2%). In the bilateral examination, the common femoral vein of the left limb was most frequently affected (n = 18, 20.0%). No deep CVI was detected in the anterior tibial veins in either sex.

Table 2 shows a comparison of vein diameters by US duplex in 956 limbs with and without deep CVI by sex and laterality. In the 956 limbs examined, in both women and men, no significant dilation of the diameter of veins and vein segments with deep CVI was observed compared to veins and segments without deep CVI.

### ***Relationship between US duplex vein diameter and degree of insufficiency in deep CVI by sex***

In women with right deep CVI, a slight but non-significant increase in the diameter of the common femoral vein, deep femoral vein, and popliteal vein was found. This finding correlated directly with an increase in insufficiency (Table 3). In men, a slight but non-significant increase in the diameter of the common femoral vein, the deep femoral vein, and the popliteal vein was found in grade 3 cases of deep CVI on the right, while in grade 2, the diameter was variable.

In women with deep CVI in the left limbs and grade 2 and 3 insufficiency, a slight but non-significant increase in the diameter of all veins within the deep venous system was found, except for the popliteal vein, which showed a decrease in diameter in grade 2 (Table 4). In men with deep CVI in the left limbs and grade 2 and 3 insufficiency, a similar slight but non-significant increase

in the diameter of all veins in the deep venous system was observed, except for the common femoral vein, which showed a decrease in diameter in grade 2.

### ***Primary cause of venous insufficiency by US duplex in deep CVI by sex and laterality of the limbs***

The primary cause was identified in 65 (44.5%) of 146 women and in 36 (48.0%) of 75 men with deep CVI (Table 5). Of these cases, 64 (44.4%) involved the right limb and 80 (55.6%) involved the left limb. In women, unilateral studies showed that the left femoral vein, with its three segments, was most commonly affected, followed by the left common femoral vein. In bilateral studies, the right common femoral vein and the proximal third of the right femoral vein were most frequently affected. Unilateral studies also showed that the left femoral vein was most frequently affected in its three segments in men. In bilateral studies, the most commonly affected were the right common femoral vein and the proximal third of the right femoral vein. Figure 1 shows three cases of primary deep CVI.

### ***Secondary cause of venous insufficiency by US duplex in deep CVI by sex and laterality of the limbs***

Secondary causes were identified in 81 (55.5%) of 146 women and 39 (52.0%) of 75 men with deep CVI (Table 6). Of these, 60 (37.7%) cases affected the right limb and 99 (62.3%) the left limb. The left femoral

**Table 3.** Relationship between US duplex vein diameter and grade of insufficiency in deep CVI of the right limbs by sex<sup>a</sup>

Description	Women						Men					
	n	Grade 1	n	Grade 2	n	Grade 3	n	Grade 1	n	Grade 2	n	Grade 3
Common femoral vein, mm	57	17.3 ± 3.1	48	17.6 ± 2.5	100	17.8 ± 2.7	19	20.8 ± 2.8	24	19.5 ± 4.3	40	21.1 ± 3.6
Proximal third femoral vein, mm	57	12.9 ± 2.0	48	13.3 ± 1.8	100	14.1 ± 2.5	19	16.1 ± 2.9	24	13.9 ± 3.0	40	15.9 ± 2.9
Middle femoral vein, mm	35	11.0 ± 2.2	29	11.7 ± 2.9	50	12.4 ± 2.7	7	12.7 ± 4.2	17	11.9 ± 1.8	19	13.9 ± 2.9
Distal third femoral vein, mm	35	11.5 ± 2.7	29	11.8 ± 2.6	50	12.2 ± 2.4	7	14.0 ± 2.0	17	11.0 ± 2.1	19	13.6 ± 2.6
Deep femoral vein, mm	56	10.6 ± 2.1	48	11.2 ± 2.0	99	11.7 ± 2.3	19	12.9 ± 1.9	22	11.4 ± 2.1	39	13.1 ± 2.3
Popliteal vein, mm	50	11.3 ± 2.2	43	11.3 ± 2.1	97	12.3 ± 2.4	17	13.9 ± 4.6	21	11.7 ± 2.4	39	14.1 ± 2.7

<sup>a</sup>Includes unilateral and bilateral US duplex. All values are means and standard deviations.

CVI: chronic venous insufficiency; US: ultrasound.

**Table 4.** Relationship between the US duplex vein diameter and grade of insufficiency in deep CVI of the left limbs by sex<sup>a</sup>

Description	Women						Men					
	n	Grade 1	n	Grade 2	n	Grade 3	n	Grade 1	n	Grade 2	n	Grade 3
Common femoral vein, mm	89	16.6 ± 2.6	69	16.9 ± 2.4	123	17.3 ± 2.4	36	19.4 ± 2.6	25	18.8 ± 5.0	55	20.9 ± 3.9
Proximal third femoral vein, mm	89	12.5 ± 2.1	69	13.1 ± 2.1	123	12.3 ± 2.1	36	13.8 ± 2.3	25	14.5 ± 3.2	55	15.1 ± 2.3
Middle femoral vein, mm	55	10.5 ± 2.3	43	11.4 ± 2.8	68	11.9 ± 2.1	21	11.1 ± 2.4	16	12.0 ± 3.3	20	12.6 ± 2.3
Distal third femoral vein, mm	55	10.7 ± 2.3	43	11.2 ± 2.2	68	11.9 ± 2.1	21	11.4 ± 2.8	16	12.3 ± 3.2	20	12.6 ± 2.6
Deep femoral vein, mm	89	10.8 ± 2.3	69	1.0 ± 2.0	122	11.7 ± 1.8	34	11.8 ± 1.7	24	12.1 ± 3.3	55	12.9 ± 2.2
Popliteal vein, mm	74	11.0 ± 2.1	65	10.7 ± 1.7	116	12.2 ± 2.3	33	11.4 ± 2.0	25	11.7 ± 2.4	55	13.7 ± 3.0

<sup>a</sup>Includes unilateral and bilateral US duplex. All values are means and standard deviations.

CVI: chronic venous insufficiency; US: ultrasound.

**Table 5.** Primary cause of venous insufficiency by US duplex in deep CVI by sex and laterality of the limbs<sup>a</sup>

Description	Unilateral US duplex				Bilateral US duplex			
	Women		Men		Women		Men	
	Right (n = 9)	Left (n = 17)	Right (n = 12)	Left (n = 9)	Right (n = 32)	Left (n = 38)	Right (n = 11)	Left (n = 17)
Common femoral vein insufficiency, yes	3 (33.3)	6 (35.2)	6 (50.0)	4 (44.4)	9 (28.1)	8 (21.0)	7 (63.6)	9 (52.9)
Proximal third femoral vein insufficiency, yes	3 (33.3)	7 (41.1)	6 (50.0)	5 (55.5)	10 (31.2)	9 (23.6)	7 (63.6)	9 (52.9)
Middle femoral vein insufficiency, yes	3 (33.3)	7 (41.1)	7 (58.3)	5 (55.5)	7 (21.8)	5 (13.1)	4 (36.3)	6 (35.2)
Distal third femoral vein, insufficiency, yes	2 (22.2)	7 (41.1)	6 (50)	5 (55.5)	7 (21.8)	7 (18.4)	4 (36.3)	6 (35.2)
Deep femoral vein insufficiency, yes	1 (11.1)	4 (23.5)	6 (50)	4 (44.4)	4 (12.5)	5 (13.1)	2 (18.1)	4 (23.5)
Popliteal vein insufficiency, yes	2 (22.2)	6 (34.2)	5 (41.6)	4 (44.4)	7 (21.8)	6 (15.7)	4 (36.3)	4 (23.5)

<sup>a</sup>Some patients had insufficiency in two or more veins or segments. The tibial and peroneal veins were not primarily affected. Values are absolute frequencies and percentages.

CVI: chronic venous insufficiency; US: ultrasound.

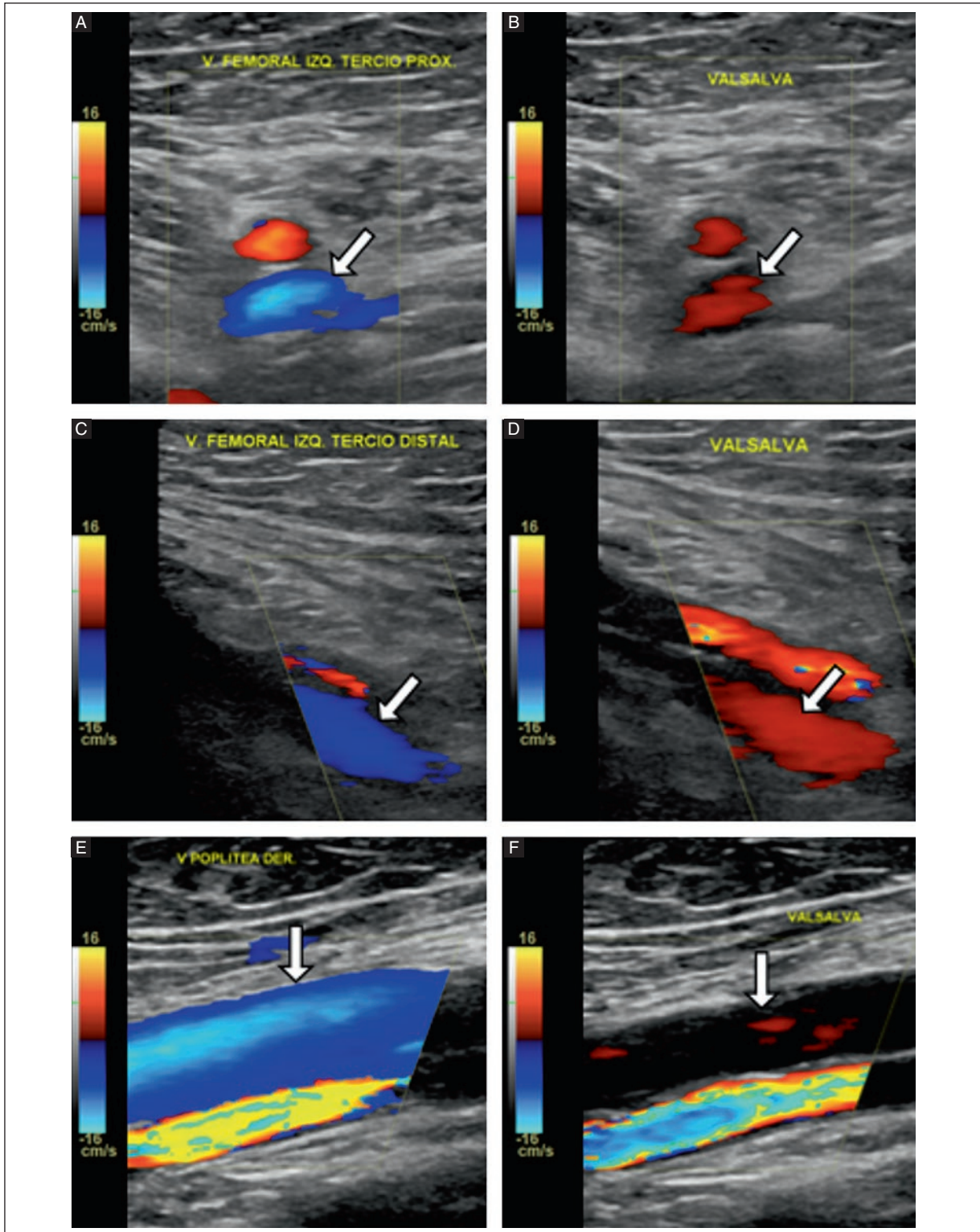


**Figure 1.** US duplex and color Doppler of a 49-year-old woman with clinically suspected CVI. **A:** transverse view of the proximal third of the left femoral vein with normal patency (arrow). **B:** Valsalva maneuver with inversion from blue to red (arrow) in the femoral vein due to reflux-diagnosis of primary deep CVI. US duplex and color Doppler of a 47-year-old woman with clinically suspected CVI. **C:** sagittal view of the distal third femoral vein with normal patency (arrow). **D:** Valsalva maneuver with inversion from blue to red in the femoral vein in relation to the reflux (arrow)-diagnosis of primary deep CVI. Color Doppler US of a 53-year-old woman with clinically suspected CVI. **E:** sagittal view of the popliteal vein with normal patency (arrow). **F:** Valsalva maneuver with minimal reflux seen by the change in hue from blue to red (arrow)-diagnosis of primary deep CVI.

CVI: chronic venous insufficiency; US: ultrasound.



**Table 6.** Secondary cause of venous insufficiency by US duplex in deep CVI by sex and laterality of the limbs<sup>a</sup>

Description	Unilateral US duplex				Bilateral US duplex			
	Women		Men		Women		Men	
	Right (n = 14)	Left (n = 29)	Right (n = 9)	Left (n = 13)	Right (n = 26)	Left (n = 38)	Right (n = 11)	Left (n = 19)
Common femoral vein insufficiency, yes	6 (31.5)	18 (48.6)	7 (46.6)	6 (23.0)	6 (15.3)	14 (27.4)	5 (35.7)	8 (30.7)
Proximal third femoral vein insufficiency, yes	7 (36.8)	20 (54.5)	8 (53.3)	11 (42.3)	8 (20.5)	17 (33.3)	5 (35.7)	8 (30.7)
Middle femoral vein insufficiency, yes	8 (42.1)	20 (54.5)	7 (46.6)	9 (34.6)	7 (17.9)	14 (27.4)	3 (21.4)	4 (15.3)
Distal third femoral vein, insufficiency, yes	8 (42.1)	21 (56.7)	7 (46.6)	10 (38.4)	7 (17.9)	13 (25.4)	3 (21.4)	7 (26.9)
Deep femoral vein insufficiency, yes	5 (26.3)	11 (29.7)	5 (33.3)	7 (26.9)	5 (12.8)	11 (21.5)	2 (14.2)	7 (26.9)
Popliteal vein insufficiency, yes	9 (47.3)	18 (48.6)	5 (33.3)	10 (38.4)	4 (10.2)	10 (19.6)	3 (21.4)	7 (26.9)
Posterior tibialis vein insufficiency, yes	-	1 (2.7)	-	-	-	-	-	-
Peroneal vein, insufficient, yes	2 (10.5)	5 (13.5)	2 (13.3)	6 (23.0)	1 (2.5)	3 (5.8)	2 (14.2)	4 (15.3)

<sup>a</sup>Some patients had insufficiency in 2 or more veins or segments. The anterior tibial veins had no secondary cause. Values are absolute frequencies and percentages. CVI: chronic venous insufficiency; US: ultrasound.

vein was most frequently affected in its three segments in both unilateral and bilateral examinations in women, followed by the common femoral vein. The proximal third of the right femoral vein was most affected in the unilateral US duplex examination in men, followed by the common femoral vein and the middle and distal third of the femoral vein. On bilateral examination, involvement decreased, as the common femoral vein and the proximal third of the femoral vein were the most frequently affected. Figure 2 shows three cases of secondary deep CVI. Figure 3 shows popliteal venous insufficiency in two patients with primary and secondary deep CVI. Figure 4 shows US grayscale images of nine patients with different morphologies of chronic thrombus in deep CVI.

## DISCUSSION

Our study found deep CVI in about 1 in 3 patients with a clinical suspicion of CVI, with a higher frequency in men than women. A secondary etiology of CVI was more common. This study is the first to provide a detailed description of US duplex findings in deep CVI of the lower limbs in Mexican patients. This study provides detailed information about the affected vein segments and the variations in diameter, aspects that are not comprehensively addressed in the existing literature.

The reported prevalence of deep CVI varies<sup>16,17</sup>. In our study of 700 patients with suspected venous

insufficiency, both men and women had deep CVI in one or more segments of the deep venous system. Femoral vein insufficiency was the most common finding in both sexes, with the left common femoral vein being the most affected segment in both sexes in bilateral US duplex only. This finding is consistent with Labropoulos et al.<sup>16</sup> in 152 limbs of 120 patients. Deep CVI was present in 31 (22.0%) limbs, and the most commonly affected segment was the common femoral vein (n = 22, 71.0%). Similarly, Panpinkoon et al.<sup>17</sup> evaluated a larger sample of 1,010 limbs from 585 patients with CVI assessed by US duplex; 425 (72.6%) were examined bilaterally and 160 (27.4%) unilaterally, totaling 1,010 limbs. Deep CVI was found in 280 (27.7%) patients. The most frequently affected segments were the common femoral vein (n = 127, 12.6%), followed by a combination of the common femoral vein and the femoral vein (n = 42, 4.2%) and a combination of the common femoral vein and the deep femoral vein (n = 37, 3.7%). These findings reinforce the idea that these veins play a central role in deep CVI pathogenesis. Gudmundur et al.<sup>18</sup> found femoral vein insufficiency in 244 (61.0) limbs in the US examination of 401 limbs in patients with deep CVI. In our study of 700 patients with CVI, 221 (31.6%) had deep CVI. The most frequently affected veins in women were the common femoral vein (n = 79, 35.7%) and the proximal third of the femoral vein (n = 81, 36.7%), while in men, the common femoral

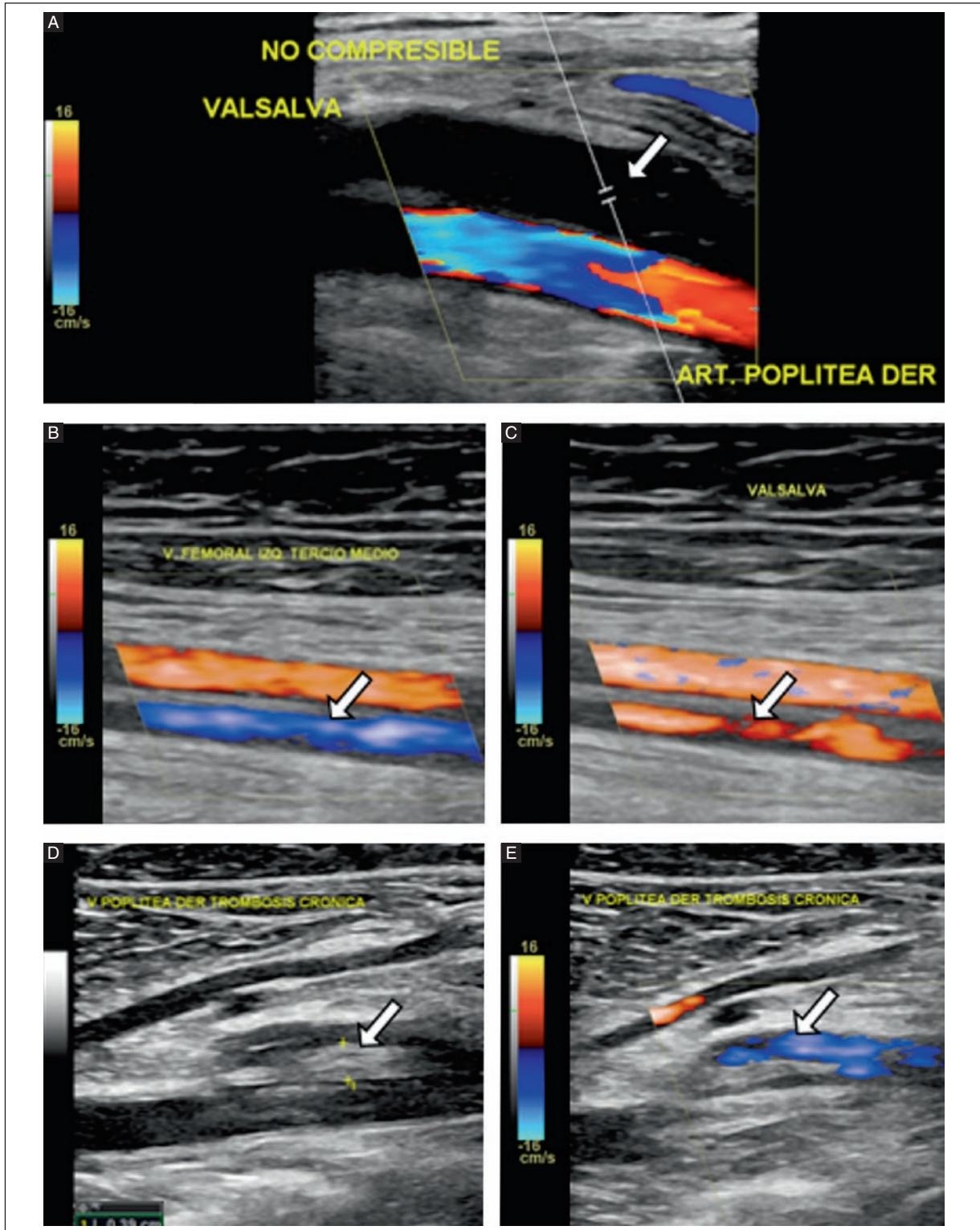


**Figure 2.** Color Doppler US of a 49-year-old man with clinically suspected CVI. **A:** US duplex, sagittal view showing an anechoic image in the right popliteal vein with absent flow and spectral absence (arrow). Diagnosis of acute thrombosis causing secondary deep CVI. Color Doppler US in a 47-year-old woman with clinical suspicion of CVI. **B:** proximal third of the left common femoral vein with endoluminal echogenic material, heterogeneous texture with lack of flow in its entirety (arrow). **C:** middle third of the left common femoral vein with absent of flow in relation to the subacute thrombus (arrow). Diagnosis of subacute thrombosis causing secondary deep CVI. 42-year-old woman with clinical suspicion of CVI. **D:** US grayscale, sagittal view of the right popliteal vein with a 3.9-mm central, predominantly homogeneous (arrow) echogenic band. **E:** color Doppler US, sagittal view, of the right popliteal vein with flow in relation to 50% recanalization (arrow). Diagnosis of chronic thrombosis causing secondary deep CVI.

CVI: chronic venous insufficiency; US: ultrasound.

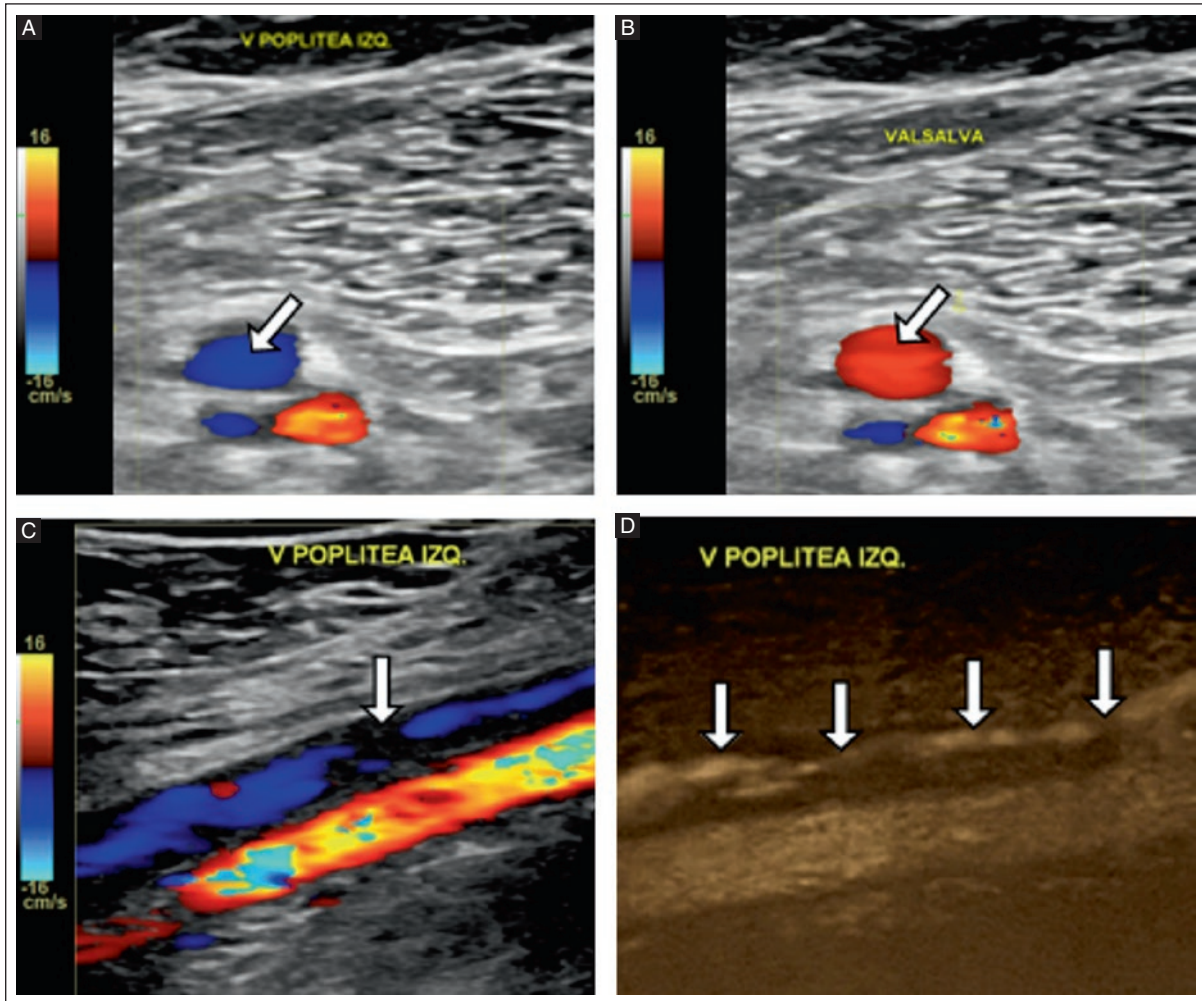


**Figure 3.** Popliteal venous insufficiency in two patients with primary and secondary deep CVI. **A:** 49-year-old man with clinical suspicion of CVI. **A:** color Doppler US, transverse view, normal patency of the popliteal vein (arrow). **B:** color Doppler US, transverse view, Valsalva maneuver with inversion from blue to red (arrow) in relation to reflux-diagnosis of primary deep CVI. A 26-year-old woman with secondary etiology of deep CVI. **C:** color Doppler US, **D:** B-flow, sagittal views, showing recanalization of the popliteal vein (< 50%) (arrows)-diagnosis of secondary deep CVI.

CVI: chronic venous insufficiency; US: ultrasound.

vein was the most frequently affected (n = 55, 73.3%). The frequency of affected veins or segments in the deep venous system in patients with deep CVI in our study was described in detail using US duplex and a significant percentage of patients had abnormalities in multiple venous segments of the deep venous system.

Literature regarding the grades of venous insufficiency in the deep venous system in patients with deep CVI is limited. Gudmundur et al.<sup>18</sup> examined 401 legs of 272 patients with deep CVI using US duplex. They assessed the clinical value of quantifying the reflux time (RT) in seconds and the peak reverse flow velocity (PRFV) of segments of the deep venous system (common femoral vein, femoral vein, deep femoral vein, and popliteal

vein). These findings were graded on a scale of 0 to 4: Grade 0 = RT < 0.5s, Grade 1 = RT > 0.5s and <1.0s with PRFV < 10 cm/s, Grade 2 = RT > 1.0 and < 2.0s with PRFV 10-20 cm/s, Grade 3 = RT > 2.0 and <3.0s with PRFV 20-30 cm/s, and Grade 4 = RT >3.0s with PRFV > 30 cm/s. Their study showed that deep venous reflux reflects venous dysfunction and significantly contributes to the prevalence of skin changes and ulcers. In our previous report of 500 patients, we found that 98 (19.6%) had deep CVI, with a higher prevalence in men (n = 58, 26.1%) than in women (n = 40, 16.7%)<sup>5</sup>. Men were more likely to have a more advanced stage of venous reflux, grade 3. This pattern of higher severity in men is consistent with our findings, where most men exhibited grade 3 venous

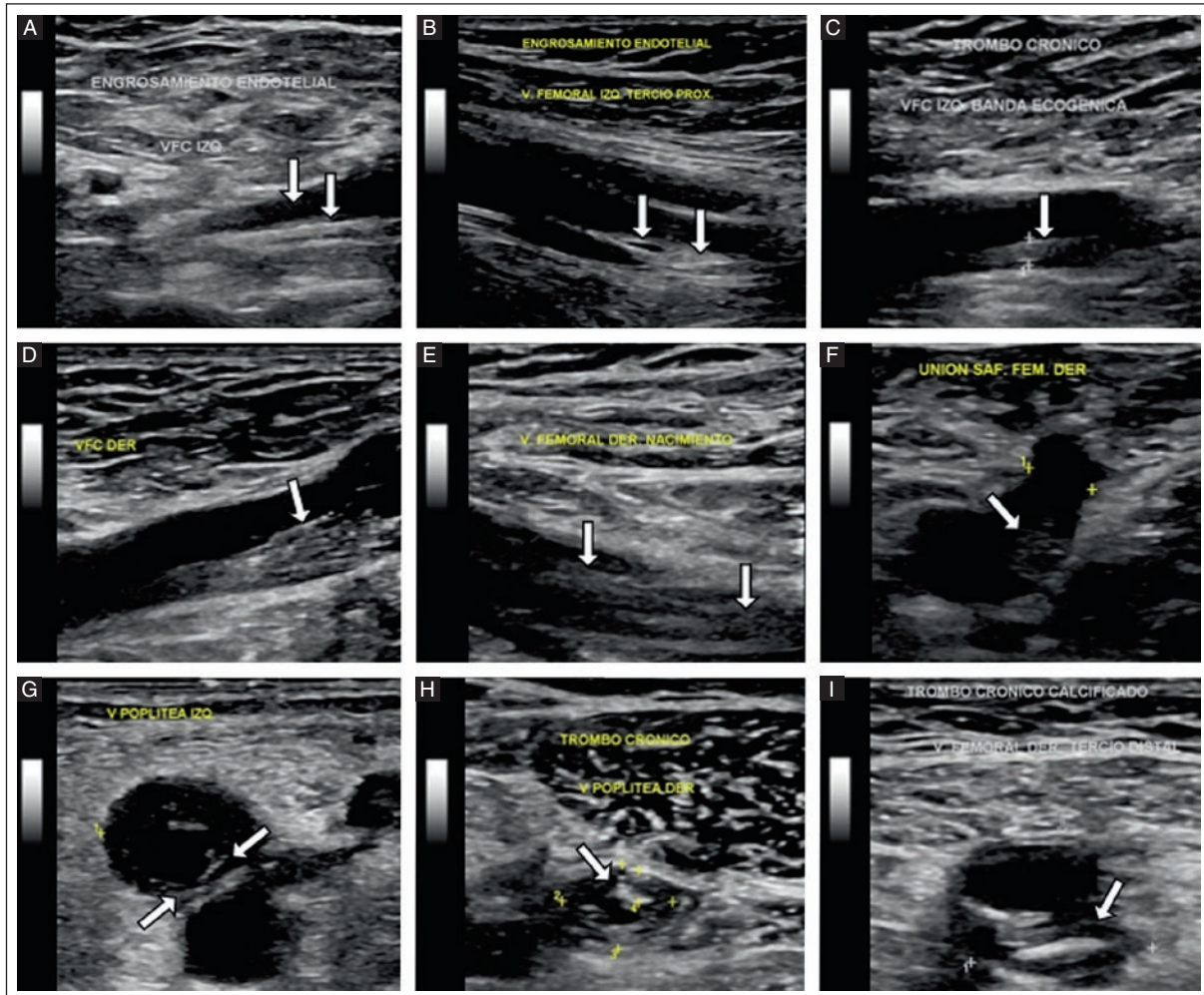


**Figure 4.** US grayscale showing different morphology of the chronic thrombus in deep CVI. Images of 9 patients are shown. **A:** sagittal view, left common femoral vein with fine endothelial thickening (arrows). **B:** sagittal view, showing an echogenic band in the proximal third of the femoral vein (arrows). **C:** sagittal view, showing an echogenic band in the common femoral vein with a thickness of 3.3 mm (arrow). **D:** sagittal view shows 7 mm thick echogenic material (not shown) in the right common femoral vein, with a heterogeneous texture adherent to the posterior wall (arrow). **E:** the sagittal view shows a central echogenic band adhered to the anterior wall of the right femoral vein (arrows). **F:** transverse view with rounded echogenic material adhered to the inferomedial wall of the femoral vein at the level of the right saphenous-femoral junction (arrow). **G:** transverse view of concentric echogenic material adhered to the walls of the right popliteal vein (arrows). **H:** transverse view of thick, concentric, hyperechogenic material in the right popliteal vein (arrow). **I:** transverse view of hyperechogenic material with thick bands in relation to a chronic calcified thrombus in the distal third of the right femoral vein (arrow).  
CVI: chronic venous insufficiency; US: ultrasound.

insufficiency, with the common femoral vein being the most affected segment<sup>5</sup>. In both limbs and sexes, the majority of patients with CVI had grade 3 venous insufficiency, while vein dilation of the deep venous system showed a non-significant increase in grades 1, 2, and 3 in both men and women. Labropoulos et al.<sup>16</sup> and Panpinkoon et al.<sup>17</sup> reported that men and women had similar grades of reflux, although there were differences in prevalence and affected segments<sup>17,18</sup>. Gudmundur et al.<sup>18</sup> deepened the assessment of venous reflux by measuring quantitative parameters such as RT and PRFV,

which were associated with grades of insufficiency. Their approach emphasizes the importance of hemodynamic assessment in understanding the clinical impact of deep CVI, particularly in terms of its contribution to the development of skin changes and ulcers. The quantification of reflux time and flow velocity may allow a more accurate determination of venous dysfunction in deep CVI by correlating the severity of reflux with clinical manifestations such as skin changes and the occurrence of ulcers. The trend toward higher severity in men also emphasizes the need for gender-specific studies of deep CVI.

The prevalence of deep CVI in men and women is a topic that has been of interest in recent studies, with various authors offering perspectives that show clear patterns and notable differences between sexes. We previously reported that of 500 patients studied ( $n = 98$ , 19.6%), deep CVI occurred with a higher prevalence in men ( $n = 40$ , 26.1%) than in women ( $n = 58$ , 16.7%)<sup>5</sup>. This study of 700 patients also showed a higher prevalence of deep CVI in men (34.9%) than women (30.2%). Although women formed the majority of the sample, a higher prevalence of advanced venous insufficiency was observed in men, findings consistent with our previous report<sup>5</sup>. In the studies reviewed, there was generally a higher prevalence of deep CVI in men, especially in more advanced degrees of insufficiency. There is no clear rationale for this difference. The prevalence of severe reflux in men, which was reported as predominant, suggests that previous thrombotic processes may influence this higher severity in men.

The cause of deep CVI can vary between loss of valve function, which can occur due to deep vein thrombosis (secondary cause), and increased venous pressure, which can occur in congestive heart failure (primary cause)<sup>19</sup>. According to various studies, secondary deep CVI is more common than primary. Goel et al.<sup>2</sup> reported that 80% to 95% of cases of valvular insufficiency are secondary to post-thrombotic phenomena in deep CVI. Morishita et al.<sup>20</sup> in the Japanese population, identified ( $n = 100$ , 10.3%) patients with deep venous thrombosis, all associated with secondary causes, reinforcing the idea that thrombosis is a key factor in deep CVI development in Asian populations. This study did not evaluate primary etiology. Perrin et al.<sup>21</sup> showed that the most common deep venous reflux etiology is post-thrombotic syndrome (secondary cause), representing approximately 60–85% of patients with CVI, while isolated abnormalities (primary cause) account for less than 10%<sup>21</sup>. In our study of 700 patients, most deep CVI cases appear to be associated with secondary factors. Labropoulos et al.<sup>16</sup>, in their analysis of 152 limbs, also found a high prevalence of involvement of the common femoral vein, which is frequently affected after thrombosis. Although this study does not explicitly differentiate primary and secondary causes, the results suggest that secondary involvement is more common, given that reflux in these segments is often related to previous thrombotic events. Panpinkoon et al.<sup>17</sup> evaluated 585 patients, and although they did not detail the specific proportion of primary and secondary causes, the affected segments, such as the common and deep femoral veins, were commonly involved in cases of

previous venous thrombosis, suggesting a higher incidence of secondary etiology. In contrast, Gudmundur et al.<sup>18</sup> examined 401 limbs with deep CVI and reported that 302 (75.0%) limbs had a primary etiology and 99 (25.0%) a secondary etiology. This difference could be due to different demographic and clinical characteristics in the study population. Our study shows that secondary causes predominate, which is consistent with previous studies. Accuracy in distinguishing between primary and secondary etiologies of CVI is important, especially in populations with risk factors for venous thrombosis, as early prevention of thrombotic events may reduce the development of chronic venous complications.

One of the main strengths of our study lies in the large sample size. This significant size allows for better generalization of the results. Our approach includes a detailed assessment of each vein segment of the deep system, which contributes to a higher precision in identifying the affected segments. Our cross-sectional study limits the ability to monitor the progression of deep CVI over time. Long-term follow-up could provide more detailed information about the evolution of the disease and associated risk factors, such as lifestyle habits or comorbidities, which were not included. Our study population consisted primarily of patients referred with suspected CVI, which could bias the results towards advanced cases of the disease and limit the applicability of the data to the general population.

## CONCLUSION

Our study showed that 1 in 3 patients with suspected venous insufficiency assessed by US duplex US had deep CVI, with a higher prevalence in men than women. A secondary etiology associated with venous thrombosis and its post-thrombotic sequelae was more prevalent than a primary cause. US duplex is the most important method for diagnosing CVI. Our study provided valuable information on the most affected venous segments and gender differences in prevalence and severity allowing a better understanding of deep CVI.

## Acknowledgments

The authors thank Professor Ana M. Contreras-Navarro for her guidance in preparing and writing this scientific paper.

## Funding

This research received no external funding.

## Conflicts of Interest

The authors declare that they have no conflicts of interest.

## Ethical disclosures

**Protection of individuals.** This study complied with the Declaration of Helsinki (1964) and subsequent amendments.

**Confidentiality of data.** The authors declare they followed their center's protocol for sharing patient data.

**Right to privacy and informed consent.** Informed consent was not required for this observational study of information collected during routine clinical care.

**Use of artificial intelligence.** The authors did not use generative artificial intelligence to prepare this manuscript and/or create tables, figures, or figure legends.

## REFERENCES

1. Figueroa-Sanchez M, Gough SD, López-Mendoza M, Montero-Cedeño A. Standardized structured report for Doppler duplex ultrasound of lower extremity venous insufficiency and thrombosis: a technical note. *J Mex Fed Radiol Imaging*. 2023;2(2):133-141. doi:10.24875/JMEXFRI.M23000045.
2. Goel RR, Hardy SC, Brown T. Surgery for deep venous insufficiency. *Cochrane Database Syst Rev*. 2021;9(9):CD001097. doi: 10.1002/14651858.CD001097.pub4.
3. Blanco P. Volumetric blood flow measurement using Doppler ultrasound: concerns about the technique. *J Ultrasound*. 2015;18(2):201-204. doi: 10.1007/s40477-015-0164-3.
4. Lee DK, Ahn KS, Kang CH, Cho SB. Ultrasonography of the lower extremity veins: anatomy and basic approach. *Ultrasonography*. 2017; 36(2):120-130. doi:10.14366/usg.17001.
5. Figueroa-Sanchez M, Lopez-Mendoza MF, Gough SD, Lopez-Mendez J I. US duplex findings in chronic venous insufficiency of the lower limbs in 500 Mexican patients. *J Mex Fed Radiol Imaging*. 2024;3(1):45-55. doi: 10.24875/jmexfri.m24000069.
6. Coleridge-Smith P, Labropoulos N, Partsch H, Myers K, Nicolaidis A, Cavezzi A. Duplex ultrasound investigation of the veins in chronic venous disease of the lower limbs--UIP consensus document. Part I. Basic principles. *Eur J Vasc Endovasc Surg*. 2006;31(1):83-92. doi: 10.1016/j.ejvs.2005.07.019.
7. Necas M. Duplex ultrasound in the assessment of lower extremity venous insufficiency. *Australas J Ultrasound Med*. 2010;13(4):37-45. doi:10.1002/j.2205-0140.2010.tb00178.x.
8. Mejía-González M, López-Villa-Entebi E, Chávez-Valencia V, Chávez-Saavedra VJ. Prevalencia de enfermedad venosa crónica en personal de salud y su impacto en calidad de vida a 6 meses. *Cirugía y Cirujanos*. 2022;90(3):332-337. doi: 10.24875/ciru.20001245.
9. Singh A, Zahra F. Chronic Venous Insufficiency. StatPearls Publishing; 2024. <https://www.ncbi.nlm.nih.gov/books/NBK587341/>.
10. Torres JR, Rodilla JC, Vargas MF, Vallejo OG, Gil IG. Enfermedad venosa crónica en los nuevos tiempos. Propuesta Venoscheck. *Medicina de Familia SEMERGEN*. 2022;48(5):344-355. doi: 10.1016/j.semerg.2022.03.008.
11. Eklof B, Perrin M, Delis KT, Rutherford RB, Gloviczki P; American Venous Forum; European Venous Forum; International Union of Phlebology; American College of Phlebology; International Union of Angiology. Terminology of chronic venous disorders: the VEIN-TERM transatlantic interdisciplinary consensus document. *J Vasc Surg*. 2009;49(2):498-501. doi: 10.1016/j.jvs.2008.09.014.
12. Bergan JJ, Schmid-Schönbein GW, Smith PD, Nicolaidis AN, Boisseau MR, Eklof B. Chronic venous disease. *N Engl J Med*. 2006;355(5):488-498. doi: 10.1056/NEJMra055289.
13. Needleman L, Cronan JJ, Lilly MP, Merli GJ, Adhikari S, Hertzberg BS, et al. Ultrasound for Lower Extremity Deep Venous Thrombosis: Multidisciplinary Recommendations From the Society of Radiologists in Ultrasound Consensus Conference. 2018; 137(14):1505-1515. doi:10.1161/circulationaha.117.
14. Gornik HL, Sharma AM. Duplex ultrasound in the diagnosis of lower-extremity deep venous thrombosis. *Circulation*. 2014;129(8):917-921. doi:10.1161/CIRCULATIONAHA.113.002966.
15. Evans CJ, Allan PL, Lee AJ, Bradbury AW, Ruckley CV, Fowkes FG. Prevalence of venous reflux in the general population on duplex scanning: the Edinburgh vein study. *J Vasc Surg*. 1998;28(5):767-776. doi: 10.1016/s0741-5214(98)70051-5.
16. Labropoulos N, Tassiopoulos AK, Kang SS, Mansour MA, Littooy FN, Baker WH. Prevalence of deep venous reflux in patients with primary superficial vein incompetence. *J Vasc Surg*. 2000;32(4):663-668. doi: 10.1067/mva.2000.110050.
17. Panpikoon T, Wedsart B, Treesit T, Chansanti O, Bua-Ngam C. Duplex ultrasound findings and clinical classification of lower extremity chronic venous insufficiency in a Thai population. *J Vasc Surg Venous Lymphat Disord*. 2019;7(3):349-355. doi: 10.1016/j.jvsv.2018.08.012.
18. Gudmundur D, Bo E, Grandinetti A, Lurie F, Kistner R. Deep axial reflux, an important contributor to skin changes or ulcer in chronic venous disease. *J Vasc Surg*. 2003;38(6):1336-1341. doi: 10.1016/s0741-5214(03)00907-8.
19. Zollmann P, Zollmann C, Zollmann P, Veltman J, Kerzig D, Doerler M. Determining the origin of superficial venous reflux in the groin with duplex ultrasound and implications for varicose vein surgery. *J Vasc Surg Venous Lymphat Disord*. 2017;5(1):82-86. doi:10.1016/j.jvsv.2016.10.001.
20. Morishita Y, Fujihara M. Incidence of deep vein thrombosis from screening by venous ultrasonography in Japanese patients. *Heart Vessels*. 2020;35(3):340-345. doi: 10.1007/s00380-019-01488-w.
21. Perrin, M. La chirurgie des reflux veineux profonds des membres inférieurs. *J Med Vasc*. 2004;29(2):73-87. doi:10.1016/s0398-0499(04)96718-2.

# Abnormal Achilles tendon US findings in Mexican patients with type 2 diabetes

Ivan Martinez-Flores\*<sup>ID</sup> and David Aguilar-Obeso<sup>ID</sup>

Radiology and Imaging Department, Hospital General Regional No. 1, Instituto Mexicano del Seguro Social. Tijuana, Baja California, Mexico

## ABSTRACT

**Introduction.** Achilles tendon abnormalities on ultrasound (US) have been associated with type 2 diabetes. This study aimed to identify the Achilles tendon US findings in Mexican patients with type 2 diabetes. **Material and methods:** This was a cross-sectional study of adult patients with type 2 diabetes. The variables recorded were age, sex, time since diagnosis of type 2 diabetes, body mass index (BMI), glycosylated hemoglobin, and treatment. Both Achilles tendons were examined with US and the abnormal findings were fibrillar disorganization, intrasubstance calcifications, hypoechoic foci, and increased Achilles tendon thickness. **Results:** Seventy Achilles tendons were examined in 35 type 2 diabetes patients. The mean age was  $55.7 \pm 12.02$  years. Twenty-nine (82.8%) were women, and 6 (17.2%) were men. US abnormalities were found in 60 Achilles tendons in 33 (94.3%) of 35 patients. Intrasubstance calcifications were the most common finding in both tendons ( $n = 29$ , 50.8% right and  $n = 24$ , 47.1% left), followed by fibrillar disorganization ( $n = 14$ , 24.6% right and  $n = 17$ , 33.3% left). Thickening was found in only two (3.5%) right tendons. Overweight or obese patients had more abnormal US findings in the Achilles tendon. **Conclusion:** Abnormal US findings of the Achilles tendon were prevalent in patients with type 2 diabetes. The most common were intrasubstance calcifications, followed by fibrillar disorganization.

**Keywords:** Achilles tendon. Type 2 diabetes. Tendinopathy. Ultrasound.

## INTRODUCTION

The Achilles tendon is the strongest and longest tendon in the human body, and it can be affected by degenerative or traumatic processes<sup>1,2</sup>. Tendinopathy is one of the most common orthopedic pathologies. The Achilles tendon is most commonly affected, accounting for 20% of all tendon injuries<sup>1</sup>. Type 2 diabetes increases the risk of musculoskeletal involvement, particularly tendinopathy,<sup>3</sup> due to cell metabolism alterations, increased intracellular water content leading to edema, decreased tolerance to ischemic stress, and increased fibrillar cross-linking of collagen due to the accumulation of glycosylated end products with changes in tendon structure<sup>1,4</sup>.

Type 2 diabetes is one of the most prevalent chronic diseases in the Mexican population. The 2023 National Health and Aging Survey in Mexico reported a prevalence of type 2 diabetes of 25.6% in the population  $\geq 53$  years (women 28.1% and men 22.5%)<sup>5</sup>. The guideline for clinical practice in primary care in Mexico, "Prevention, diagnosis, ambulatory control goals and timely referral of type 2 diabetes", does not include screening strategies for detecting ultrasonographic abnormalities of the Achilles tendon<sup>6</sup>.

Ultrasound (US) is the initial imaging modality for diagnosing tendinopathy. The most common findings are fibrillar disorganization, intrasubstance calcifications, hypoechoic foci, and increased tendon thickness<sup>1,4,7-10</sup>.

### \*Corresponding author:

Ivan Martinez-Flores  
E-mail: dr.ivanmf23@gmail.com

Received for publication: 15-04-2024

Accepted for publication: 05-09-2024

DOI: 10.24875/JMEXFRI.M24000086

Available online: 20-12-2024

J Mex Fed Radiol Imaging. 2024;3(4):268-274

www.JMEXFRI.com

2696-8444 / © 2024 Federación Mexicana de Radiología e Imagen, A.C. Published by Permanyer. This is an open access article under the CC BY-NC-ND (<https://creativecommons.org/licenses/by-nc-nd/4.0/>).

Magnetic resonance imaging (MRI) is recommended when there is a discrepancy between the clinical and US findings or in patients who are candidates for surgical treatment of tendinopathy<sup>10</sup>. This study aimed to identify the Achilles tendon ultrasonographic findings of Mexican patients with type 2 diabetes.

## MATERIAL AND METHODS

This cross-sectional study was conducted between February and June 2023 in the Diagnostic and Therapeutic Imaging Department of Regional General Hospital No. 1 of the Mexican Social Security Institute in Tijuana, Baja California, Mexico. We included adult patients of both sexes diagnosed with type 2 diabetes from the Diabetes Care Center of the Mexican Social Security Institute (CADIMSS), where comprehensive care is provided. Patients with type 1 diabetes, Charcot neuropathy, or a history of ankle surgery were excluded. Written informed consent was obtained for study participation. The institutional ethics and research committees approved the study.

### Study development and variables

Age, sex, time since diagnosis of type 2 diabetes, body mass index (BMI), glycosylated hemoglobin, and treatment were recorded. CADIMSS patients were invited to participate by the treating physician and referred to the radiology department for an US examination of both Achilles tendons.

### Imaging and analysis protocol

The US examination of the Achilles tendons was performed using the MyLab™ Seven System (Esaote, Genoa, Italy) with a linear 9 MHz transducer and real-time grayscale tracking. The protocol was performed with the patient in a prone position, with both Achilles tendons parallel to the examination table in the longitudinal and transverse planes from the myotendinous junction to their insertion on the calcaneus on both sides<sup>11</sup>. Achilles tendon thickness was measured in millimeters (mm) in the transverse plane at the level of the medial malleolus. Normal thickness is approximately 5 to 6 mm (Figure 1). The US examination was performed by a fourth-year radiology resident (IMF) under the supervision of a radiologist (DAO) with 22 years of experience.

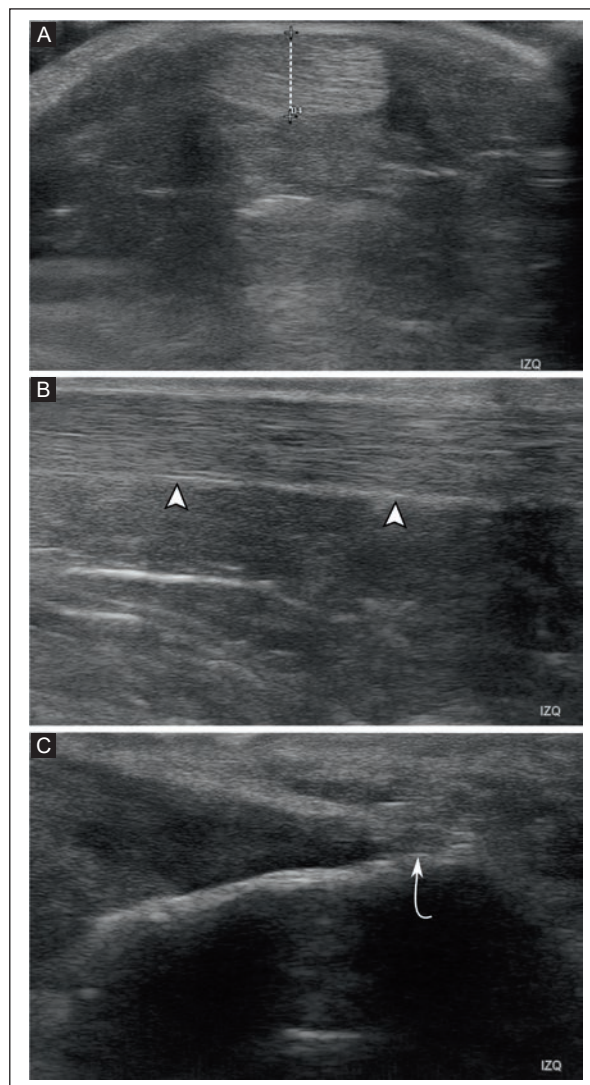


**Figure 1.** US grayscale of a 49-year-old woman with an 8-year history of type 2 diabetes. **A:** transverse view of the Achilles tendon at the level of the medial malleolus, showing normal thickness (5.7 mm) (dotted line). **B:** longitudinal view of the Achilles tendon in the middle third, showing a normal fibrillar pattern and normal echogenicity (arrowheads). **C:** longitudinal view of the Achilles tendon at its distal insertion showing normal echogenicity and smooth bony edges (curved arrow).

US: ultrasound.

### Abnormal US findings

**Fibrillar disorganization:** the loss of a normal fibrillar pattern, with twisted, curved, overlapping, and disorganized fibers<sup>11</sup>.

**Intrasubstance calcifications:** circumscribed hyperechoic images, with associated acoustic shadowing within the Achilles tendon<sup>11</sup>.

**Hypoechoic foci:** circumscribed hypoechoic areas with different morphology within the Achilles tendon<sup>11</sup>.

**Increased Achilles tendon thickness:** an anteroposterior diameter of more than 6 mm<sup>11</sup>.



### Statistical analysis

Qualitative variables are presented with frequencies and percentages. Quantitative variables are presented with measures of central tendency and dispersion. The relationship between categorical variables was analyzed using the chi-square test. The difference in means between numerical variables was analyzed using Student's t-test for two groups and ANOVA for three or more groups. The analysis was performed in SPSS version 28 (IBM Corp., Armonk, NY, USA).

### RESULTS

Thirty-five patients with type 2 diabetes were assessed (Table 1). The mean age was 55.7 ± 12.02 years. There were 29 (82.8%) women and 6 (17.2%) men. The time since diagnosis was ≥5 years in 26 (74.2) of the 35 patients. Regarding BMI, overweight was found in 19 (54.2%) and obesity in 13 (37.1%). Most patients had poor glycemic control (HbA1c > 7%) (n = 24, 68.5%). Combined oral therapy and insulin were the most common (n = 21, 60.0%). Two (5.7%) of 35 patients had normal US findings on examination of both tendons (Table 2). Figure 1 shows the US findings with normal fibrillar pattern and Achilles tendon thickness. Thirty-three (94.3%) of 35 patients had ultrasonographic abnormalities in one or both tendons; 5 (15.1%) in the right Achilles tendon, 1 (3.0%) in the left tendon, and 27 (81.9%) with abnormalities in both tendons.

#### Abnormal Achilles tendon US findings in patients with type 2 diabetes

Abnormal US findings in 60 tendons are shown in Table 3. Intrasubstance calcifications were the most common finding in both tendons (n = 29, 50.8% right and n = 24, 47.1% left), followed by fibrillar disorganization (n = 14, 24.6% right and n = 17, 33.3% left). Thickening was found in only two (3.5%) right tendons. Figure 2 shows an Achilles tendon US examination with fibrillar disorganization, intrasubstance calcification towards the distal insertion, hypoechoic foci, and increased tendon thickness (10.4 mm). Figure 3 shows Achilles tendon US abnormalities with fibrillar disorganization, intrasubstance calcification towards the distal insertion, hypoechoic foci, and increased tendon thickness (7.1 mm). Figure 4 shows Achilles tendon US examination with an intrasubstance calcification towards the distal insertion and hypoechoic foci.

**Table 1.** Characteristics of 35 Mexican patients with type 2 diabetes

Description	Parameters
Age, years, mean ± SD	55.7 ± 12.02
Women, n (%)	29 (82.8)
Men, n (%)	6 (17.2)
Time since type 2 diabetes diagnosis	
< 5 years, n (%)	9 (25.8)
5-10 years, n (%)	13 (37.1)
> 10 years, n (%)	13 (37.1)
BMI	
Normal, n (%)	3 (8.7)
Overweight, n (%)	19 (54.2)
Obese, n (%)	13 (37.1)
Glycosylated hemoglobin	
Good glycemic control, n (%)	11 (31.5)
Poor glycemic control, n (%)	24 (68.5)
Treatment	
Oral medication, n (%)	13 (37.2)
Insulin, n (%)	1 (2.8)
Combined therapy, n (%)	21 (60.0)

BMI: body mass index.

**Table 2.** Normal and abnormal US findings of the Achilles tendon in 35 Mexican patients with type 2 diabetes

Description	n (%)
Normal US findings	2 (5.7)
Abnormal US findings	33 (94.3)
Right Achilles tendon	5 (15.1)
Left Achilles tendon	1 (3.0)
Bilateral Achilles tendon	27 (81.9)

US: ultrasound.

#### Relationship between abnormal US findings and time since type 2 diabetes diagnosis

In patients with < 5 years since the diagnosis of type 2 diabetes, fibrillary disorganization was most frequent, followed by intrasubstance calcifications (Table 4).

**Table 3.** Abnormal US findings of 60 Achilles tendons in Mexican patients with type 2 diabetes

Description <sup>a</sup>	Right Achilles tendon (n = 32)		Left Achilles tendon (n = 28)	
	Present	Absent	Present	Absent
Fibrillar disorganization, n (%)	14 (24.6)	18 (25.4)	17 (33.3)	11 (18.0)
Intrasubstance calcifications, n (%)	29 (50.8)	3 (4.2)	24 (47.1)	4 (6.6)
Hypoechoic foci, n (%)	12 (21.1)	20 (28.2)	10 (19.6)	18 (29.5)
Increased Achilles tendon thickness, n (%)	2 (3.5)	30 (42.2)	-	28 (45.9)
Total, n	57	71	51	61

<sup>a</sup>Some patients had two or more US abnormalities; US: ultrasound.

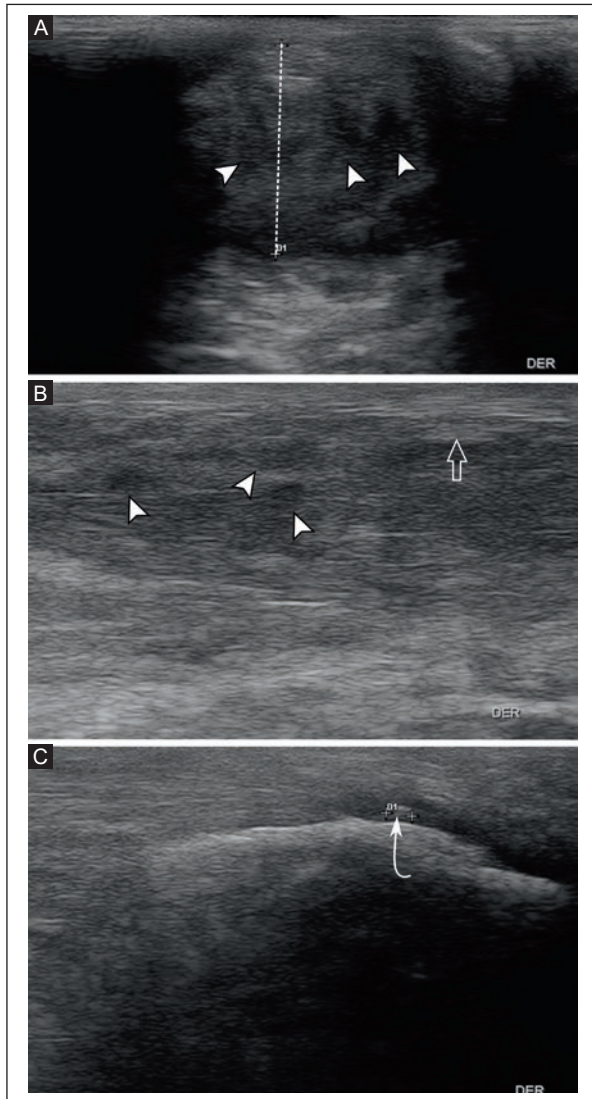


**Figure 2.** US grayscale of a 61-year-old man with a 2-year history of type 2 diabetes. **A:** transverse view of the Achilles tendon at the level of the medial malleolus level shows increased thickness of the tendon thickness (10.4 mm) (dotted line) and the presence of hypoechoic foci (arrowheads). **B:** longitudinal view of the Achilles tendon in the middle third shows a heterogeneous appearance due to hypoechoic foci (arrowheads) and fibrillar disorganization (void arrow). **C:** longitudinal view of the Achilles tendon at the distal insertion shows an intrasubstance calcification of 1.3 mm in diameter (curved arrow).  
US: ultrasound.

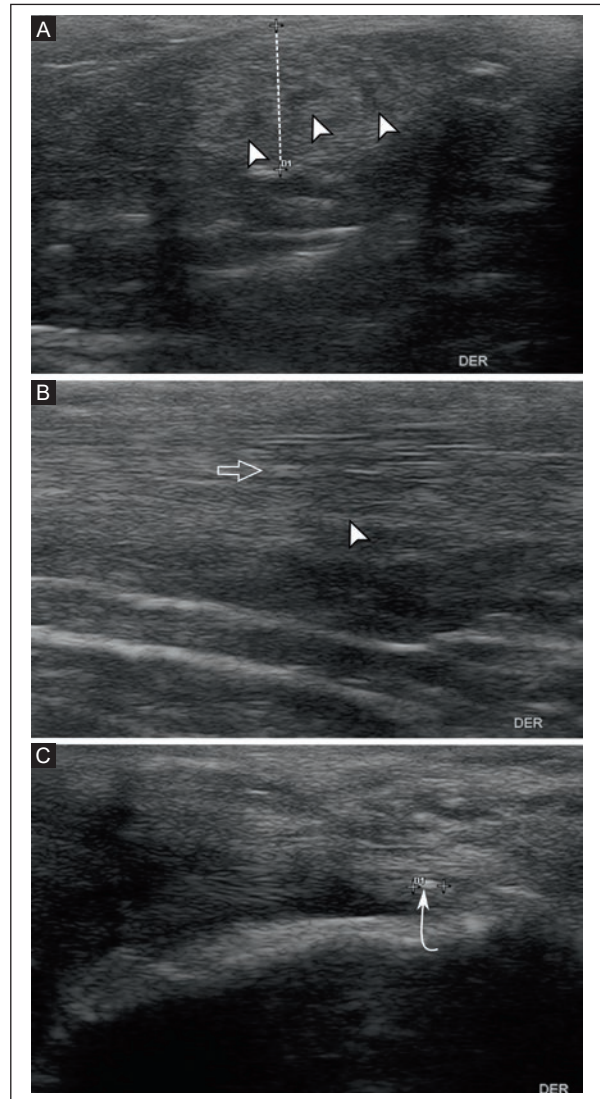


**Figure 3.** US grayscale of a 57-year-old woman with a 7-year history of type 2 diabetes. **A:** transverse view of the Achilles tendon at the medial malleolus level shows increased tendon thickness (7.1 mm) (dotted line) and the presence of hypoechoic foci (arrowheads). **B:** longitudinal view of the Achilles tendon in the middle third shows a heterogeneous appearance due to hypoechoic foci (arrowhead) and fibrillar disorganization (void arrow). **C:** longitudinal view of the Achilles tendon at its distal insertion shows an intrasubstance calcification of 1.5 mm in diameter (curved arrow).  
US: ultrasound.

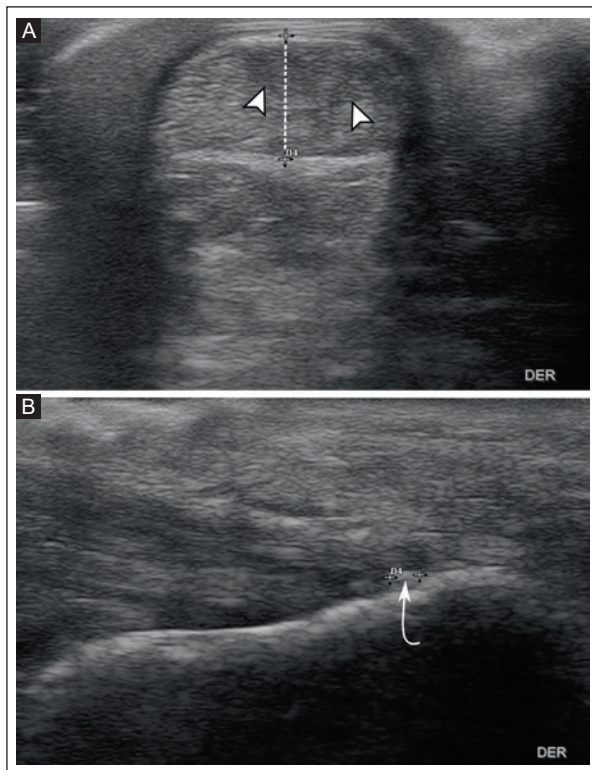


**Figure 4.** US grayscale US of a 54-year-old woman with a 2-year history of type 2 diabetes mellitus. **A:** transverse view of the Achilles tendon at the level of the medial malleolus shows a normal tendon thickness (5.8 mm) (dotted line) and hypoechoic foci (arrowheads). **B:** longitudinal view of the Achilles tendon at its distal insertion shows an intrasubstance calcification of 1.4 mm in diameter (curved arrow). US: ultrasound.

Patients with 5 to 10 years since the diagnosis of type 2 diabetes more frequently had hypoechoic foci, followed by intrasubstance calcifications, whereas patients with > 10 years had comparable frequencies of fibrillar disorganization, intrasubstance calcifications, and hypoechoic foci. Only 2 patients with < 5 years since the diagnosis of type 2 diabetes showed increased Achilles tendon thickness.

### ***Relationship between abnormal Achilles tendon US findings and BMI***

In patients with a normal BMI, intrasubstance calcifications were more frequent (Table 5). Fibrillar disorganization was comparable in overweight and obese patients, while intrasubstance calcifications and hypoechoic foci were more common in overweight patients, although the differences were not statistically significant.

## **DISCUSSION**

In this study, ultrasonographic abnormalities in one or both Achilles tendons were prevalent ( $n = 33$ , 94.3%). The most common US findings were the presence of intrasubstance calcifications, followed by fibrillar disorganization. This study is the first in Mexico to present the ultrasonographic abnormalities of the Achilles tendon in type 2 diabetes patients.

Type 2 diabetes has been associated with a higher frequency of Achilles tendon US abnormalities compared to persons without diabetes. Afolabi et al.<sup>8</sup> compared the ultrasonographic findings of the Achilles tendon of 80 patients with type 2 diabetes and 80 controls without diabetes in a cross-sectional study. In the type 2 diabetes group, fibrillar disorganization changes were found in 84 tendons (52.5%), intrasubstance calcifications in 9 tendons (5.6%), and hypoechoic foci in 31 tendons (19.3%). Type 2 diabetes patients had more frequent abnormal US findings than the control group without diabetes. Batista et al.<sup>9</sup> examined the correlation of US abnormalities with age, duration of diabetes, and glycemic control in 70 patients with type 2 diabetes and 10 controls without diabetes in a cross-sectional study. Sixty-two (88.6%) of the 70 patients showed fibrillar disorganization, and 17 (24.3%) had intrasubstance calcifications. Our study detected ultrasonographic abnormalities in 60 Achilles tendons of 33 patients with type 2 diabetes. Intrasubstance calcifications were the most common finding, followed by fibrillar disorganization. The variable frequency of abnormal US findings can be related to the lack of consensus on the definition of diagnostic features of Achilles tendinopathy.

Increased BMI is a known risk factor for Achilles tendon abnormalities<sup>1,3</sup>. Abate et al.<sup>7</sup> compared the morphologic features of the Achilles tendon by US between 136 patients with type 2 diabetes, without clinical symptoms of tendinopathy, and 273 healthy controls. The authors reported a higher prevalence of US abnormalities associated with obesity in patients with type 2 diabetes (25%) compared to controls (21.4%). In our study, fibrillar disorganization was comparable between overweight and obese patients. In contrast, intrasubstance calcifications and hypoechoic foci were more common in overweight patients, although the differences were not statistically significant. According to our study, US abnormalities are common in overweight or obese patients with type 2 diabetes. This is relevant given the high prevalence of overweight, obesity, and type 2 diabetes in the Mexican population<sup>5</sup>.

**Table 4.** Relationship between abnormal US findings in 60 Achilles tendons<sup>a</sup> and time since type 2 diabetes diagnosis

Description	Fibrillar disorganization (n = 31)	Intrasubstance calcifications (n = 53)	Hypoechoic foci (n = 22)	Increased Achilles tendon thickness (n = 2)
< 5 years, n (%)	11 (35.5)	11 (20.7)	3 (13.6)	2 (100)
5-10 years, n (%)	11 (35.5)	22 (41.5)	11 (50.0)	0
> 10 years, n (%)	9 (29.0)	20 (37.8)	8 (36.4)	0

<sup>a</sup>Some patients had two or more US abnormalities. US: ultrasound.

**Table 5.** Relationship between BMI and abnormal US findings in 60 Achilles tendons of patients with type 2 diabetes

Description	Fibrillar disorganization (n = 31)	Intrasubstance calcifications (n = 53)	Hypoechoic foci (n = 22)	Increased Achilles tendon thickness (n = 2)
Normal, n (%)	1 (3.4)	5 (9.5)	0	0
Overweight, n (%)	15 (48.3)	27 (50.9)	14 (63.6)	1 (50.0)
Obese, n (%)	15 (48.3)	21 (39.6)	8 (36.4)	1 (50.0)

BMI: body mass index; US: ultrasound.

An association between the duration of type 2 diabetes and abnormal Achilles tendon US findings has been reported<sup>7,8</sup>. Afolabi et al.<sup>8</sup> reported an association between fibrillar disorganization and diabetes duration (< 5 years: 46.5%, 5 -10 years: 70.8%, and >10 years: 84.6%) in a cross-sectional study of 80 patients with type 2 diabetes and 80 control subjects ( $p = 0.021$ ). In addition, hypoechoic foci and intrasubstance calcifications increased in direct correlation with diabetes duration, although without statistical significance. In our study, fibrillar disorganization, intrasubstance calcifications, and hypoechoic foci were observed in patients with > 10 years since the diagnosis of type 2 diabetes. In contrast, hypoechoic foci were more common in patients with 5 to 10 years, followed by intrasubstance calcifications. Abnormal Achilles tendon US findings occur as early as the first few years after the diagnosis of type 2 diabetes, and there appears to be an increase in ultrasound findings with the progression of diabetes.

The strength of this study is related to the imaging modality, as US examination is easily accessible and inexpensive. However, there are some limitations, such as the small sample size, the cross-sectional study design, the lack of clinical information on Achilles tendinopathy symptoms and physical examination findings, the intraobserver and interobserver variability of the imaging modality used, and the lack of a comparison with a control group. On the other hand, MRI, which

is the gold standard, was not performed, so it was not possible to determine the diagnostic performance of US. Also, other ultrasonographic abnormalities of Achilles tendinopathy, such as enthesopathy or intratendinous neovascularization, were not evaluated.

## CONCLUSION

In our study, abnormal Achilles tendon US findings were prevalent in Mexican patients with type 2 diabetes. US is useful for detecting Achilles tendon abnormalities. It can aid in the early detection and diagnosis of Achilles tendinopathy in patients with type 2 diabetes. Further prospective studies with a larger number of patients are needed.

## Acknowledgments

The authors thank Professor Ana M. Contreras-Navarro for her guidance in preparing and writing this scientific paper. This original research in the Radiology Specialty field was an awarded thesis at the Segunda Convocatoria Nacional 2023-2024, "Las Mejores Tesis para Publicar en el JMeXFRI."

## Funding

This research received no external funding.

## Conflicts of interest

The authors declare that they have no conflicts of interest.

## Ethical disclosures

**Protection of individuals.** This study complied with the Declaration of Helsinki (1964) and subsequent amendments.

**Confidentiality of data.** The authors declare they followed their center's protocol for sharing patient data.

**Right to privacy and informed consent.** Informed consent was not required for this observational study of information collected during routine clinical care.

**Use of artificial intelligence for generating text.** The authors did not use generative artificial intelligence to prepare this manuscript and/or create tables, figures, or figure legends.

## REFERENCES

1. Tarantino D, Mottola R, Resta G, Gnasso R, Palermi S, Corrado B, et al. Achilles Tendinopathy Pathogenesis and Management: A Narrative Review. *Int J Environ Res Public Health*. 2023;20(17):6681. doi: 10.3390/ijerph20176681.
2. Prajwal R, Sakalecha AK, Dudekula A, Varma N. Ultrasound Evaluation of Achilles Tendon Thickness in Diabetic Patients With and Without Foot Complications. *Cureus*. 2024;16(6):e62831. doi: 10.7759/cureus.62831.
3. Baskerville R, McCartney DE, McCartney SM, Dawes H, Tan GD. Tendinopathy in type 2 diabetes: a condition between specialties? *Br J Gen Pract*. 2018;68(677):593-594. doi: 10.3399/bjgp18X700169.
4. Vaidya R, Lake SP, Zellers JA. Effect of Diabetes on Tendon Structure and Function: Not Limited to Collagen Crosslinking. *J Diabetes Sci Technol*. 2023;17(1):89-98. doi: 10.1177/19322968221100842.
5. National Survey on Health and Aging in Mexico (ENASEM) 2021. Mexico: National Institute of Statistics and Geography; 2021. MEX-INEGI. ESD3.04-ENASEM-2021
6. Prevention, diagnosis, initial treatment, ambulatory control goals and timely referral of type 2 diabetes mellitus in the first level of care. *Guía de evidencias y Recomendaciones: Guía de Práctica Clínica*. Mexico, CENETEC; 2019.
7. Abate M, Salini V, Antinolfi P, Schiavone C. Ultrasound morphology of the Achilles in asymptomatic patients with and without diabetes. *Foot Ankle Int*. 2014;35(1):44-49. doi: 10.1177/1071100713510496.
8. Afolabi BI, Idowu BM, Onigbinde SO. Achilles tendon degeneration on ultrasound in type 2 diabetic patients. *J Ultrason*. 2021;20(83):e291-e299. doi: 10.15557/JoU.2020.0051.
9. Batista F, Nery C, Pinzur M, Monteiro AC, de Souza EF, Felipe FH, et al. Achilles tendinopathy in diabetes mellitus. *Foot Ankle Int*. 2008; 29(5):498-501. doi: 10.3113/FAI-2008-0498.
10. de Vos RJ, van der Vlist AC, Zwerver J, Meuffels DE, Smithuis F, van Ingen R, et al. Dutch multidisciplinary guideline on Achilles tendinopathy. *Br J Sports Med*. 2021;55(20):1125-1134. doi: 10.1136/bjsports-2020-103867.
11. Bianchi S, Martinoli C. *Ultrasound of the musculoskeletal system*. 1st edition. Springer. Berlin. 2011.

## Imaging characterization of pseudomyxoma peritonei: a case report

Araceli Cue-Castro<sup>1\*</sup> and Oscar Villagomez-Figueroa<sup>2</sup>

<sup>1</sup>Department of Imaging; <sup>2</sup>Department of Internal Medicine. Hospital General “Dr. Enrique Cabrera”, Instituto Mexicano del Seguro Social IMSS-Bienestar, Mexico City, Mexico

### ABSTRACT

*Pseudomyxoma peritonei (PMP) is a rare condition characterized by the accumulation of mucinous (gelatinous) fluid in the abdominal cavity. This case report describes an 86-year-old woman with nonspecific abdominal symptoms and a progressive increase in her abdominal circumference. Abdominal ultrasound (US) showed a complex soft tissue mass attached to the liver and the visceral side of the peritoneum on the anterior wall. We observed an “onion skin” sign—characterized by alternating layers of dense and less dense tissue—and a “starburst” appearance—characterized by radial echoes extending from a central point. Abdominal contrast computed tomography (CCT) showed visceral scalloping and “omental caking,” due to extensive peritoneal involvement—the omentum appeared diffusely thickened and adhered with centralized bowel loops. We identified an ill-defined mass in the cecum. Cytochemical analysis of the peritoneal fluid revealed a mucinous material with scant epithelial cellularity. PMP was diagnosed based on the classic imaging findings on abdominal US and CCT. This case report is intended for educational purposes. By documenting this case, we seek to improve the understanding of this rare neoplastic condition, emphasizing its imaging features on US and CCT.*

**Keywords:** Appendiceal neoplasm. Contrast computed tomography. Ultrasound. Pseudomyxoma peritonei. Case report.

### INTRODUCTION

Pseudomyxoma peritonei (PMP) is an odd clinical syndrome. It consists of the peritoneal spread of a mucus-producing neoplasm that causes mucinous ascites (the “jelly belly”) and mucinous peritoneal implants<sup>1-5</sup>. It has an incidence of one to two cases per million people<sup>1-3,6</sup>. The mean age of detection is 53 years<sup>7,8</sup> with a slight preference for women<sup>2,6,8</sup>. It is considered a clinical entity related to “borderline malignancy”<sup>9</sup>, and its prognosis depends on its origin<sup>6</sup>. The underlying cause is typically unknown, but in some cases, PMP has been diagnosed when a mucinous appendicular tumor ruptures<sup>1,2,10-12</sup>. It is also associated with tumors of the pancreas, stomach, biliary tract, intestine, ovary, and the urachus<sup>2,4,6-8</sup>. PMP presents nonspecific clinical manifestations such as abdominal distension, pain, and ascites<sup>2</sup>.

Diagnostic imaging techniques—ultrasound (US) and contrast computed tomography (CCT)—are crucial for identifying typical PMP imaging features. US usually shows peritoneal masses displacing the bowel loops medially, with visceral scalloping; echogenic ascites, described as a “starburst” appearance by Hanbidge et al.<sup>13</sup>, and the “onion skin” effect, which Sarpietro et al.<sup>2</sup> described as immobile echogenic septations with a laminated appearance<sup>2,5</sup>. On CCT, mucinous ascites appears as a low-attenuation mass—approximately 20 Hounsfield units (HU)—scattered throughout the peritoneum exerting a mass effect on the adjacent structures, which leads to a scalloping of solid viscera, displacement of the hollow viscera, and septation. “Omental caking” is a common CCT finding in PMP, but visceral scalloping remains a key diagnostic marker<sup>2,5,11,13</sup>. For the radiologist, knowing and identifying the appearance of this entity can have an

#### \*Corresponding author:

Araceli Cue-Castro  
E-mail: arabicho@hotmail.com

Received for publication: 01-08-2024

Accepted for publication: 07-10-2024

DOI: 10.24875/JMEXFRI.24000027

Available online: 20-12-2024

J Mex Fed Radiol Imaging. 2024;3(4):275-279

www.JMeXFRI.com

2696-8444 / © 2024 Federación Mexicana de Radiología e Imagen, A.C. Published by Permanyer. This is an open access article under the CC BY-NC-ND (<https://creativecommons.org/licenses/by-nc-nd/4.0/>).

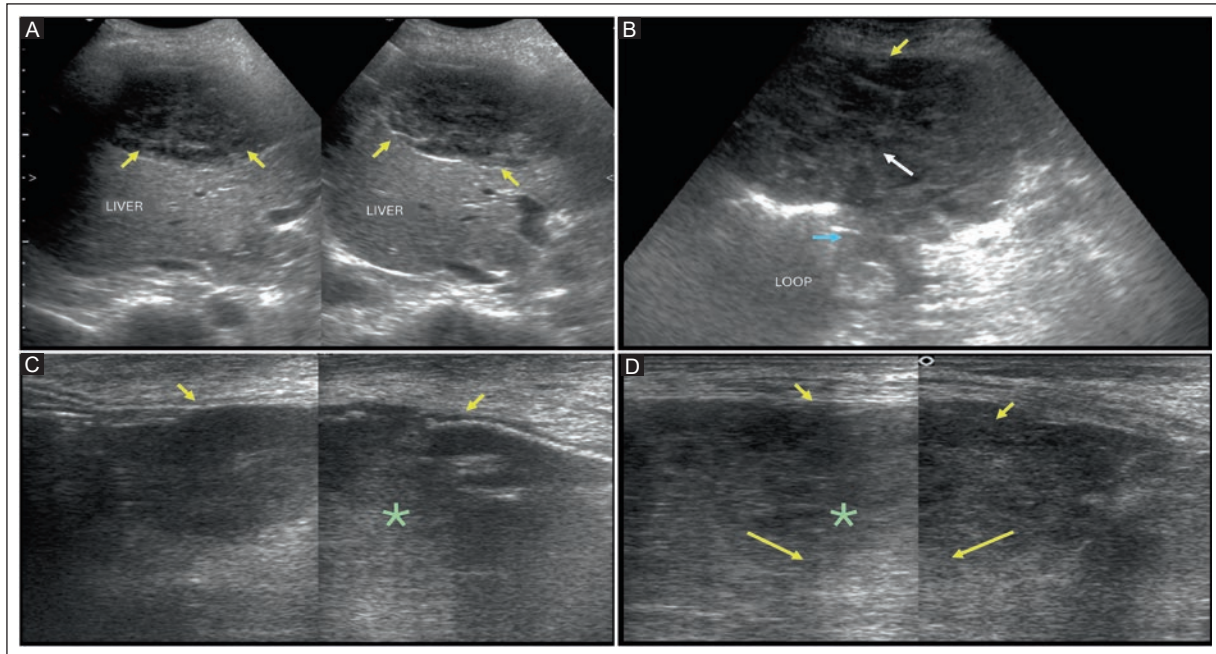


**Figure 1.** Abdominal grayscale US of an 86-year-old woman with nonspecific abdominal symptoms and increased abdominal circumference with a diagnosis of PMP. **A:** transverse view shows a complex intra-abdominal mass indenting the anterior wall of the liver (yellow arrows). **B:** transverse view shows a mass attached to the abdominal wall (yellow arrow) with the “onion skin” sign (white arrow) and a fixed bowel loop (blue arrow). **C:** transverse view of the abdominal wall and **D:** a longitudinal view shows a complex soft tissue mass attached to the visceral side of the peritoneum on the anterior wall (yellow arrows) with a “starburst” appearance (asterisk) characterized by radial echoes extending from a central point.

PMP: pseudomyxoma peritonei; US: ultrasound.

impact on the patient’s life span and quality of life<sup>8</sup>. This case report presents the classic imaging features of PMP on abdominal US and CCT.

## CASE DESCRIPTION

An 86-year-old woman with systemic arterial hypertension, type 2 diabetes, and a history of hysterectomy was admitted for weight loss, abdominal discomfort, increased abdominal circumference, and shortness of breath. On physical examination, the patient was conscious but disoriented, with respiratory distress. The abdomen was distended, with shifting dullness, diminished bowel sounds, and a positive fluid wave sign. Laboratory values showed elevated cancer antigen 19-9 (CA 19-9 = 1979 UI/mL [reference value 0-37 UI/mL]) and cancer antigen 125 (CA125 = 323 UI/mL [reference value 0-35 UI/mL]).

### Imaging findings

An abdominal US examination (Envisor™, Philips Inc. Amsterdam, The Netherlands) showed a complex

intra-abdominal soft tissue mass indenting the liver and abdominal wall with the “onion skin” sign and a “starburst” appearance (Figure 1).

A CCT scan (Incisive™, 64 slices, Philips Inc. Amsterdam, The Netherlands) showed a 0.6 cm (reference value 0.22-0.28 cm) thickened right diaphragm and subdiaphragmatic collections with hypodense nodules indenting the splenic surface. The liver appeared irregularly shaped, enlarged, medially and caudally displaced, with scalloped edges due to hypodense nodules (14-20 HU) (Figure 2A). We observed hyperdense nodules (34 HU) on the free edges of solid viscera, the abdominal wall, and the mesentery in the venous phase (Figure 2B). Centralized intestinal loops showed “omental caking.” The mesentery had increased density and decreased vascularity (Figure 3A). The cecum exhibited intense enhancement, an ill-defined mass in the arterial phase, and a large notch on the antimesenteric surface (Figure 3B). The bladder was partially distended and compressed caudally to the right, herniating towards the right inguinal canal, medial to the epigastric artery (Figure 3C). Neither the uterus nor the

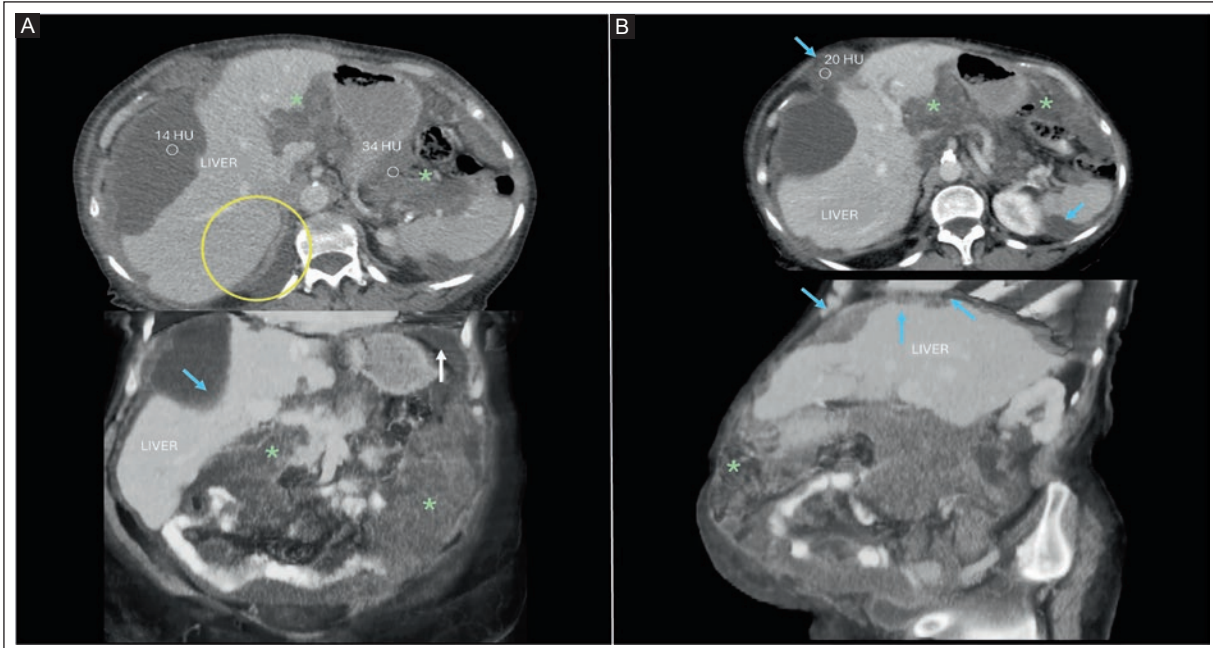


**Figure 2.** Abdominal CCT with oral mannitol contrast and intravenous iodine contrast in an 86-year-old woman with a diagnosis of PMP. **A:** axial and coronal venous phase reconstructions. **B:** axial and sagittal venous phase reconstructions. The images show a thickened (0.6 cm) right diaphragm (yellow circle) and a subdiaphragmatic collection on the left side (white arrow). The liver appeared irregularly shaped, enlarged, medially and caudally displaced, with scalloped edges due to hypodense nodules (14-20 HU) (blue arrows). Hyperdense (34 HU) nodules were observed at the free edges, abdominal wall, and mesentery in the venous phase (asterisks).

CCT: contrast computed tomography; HU: Hounsfield units; PMP: pseudomyxoma peritonei.

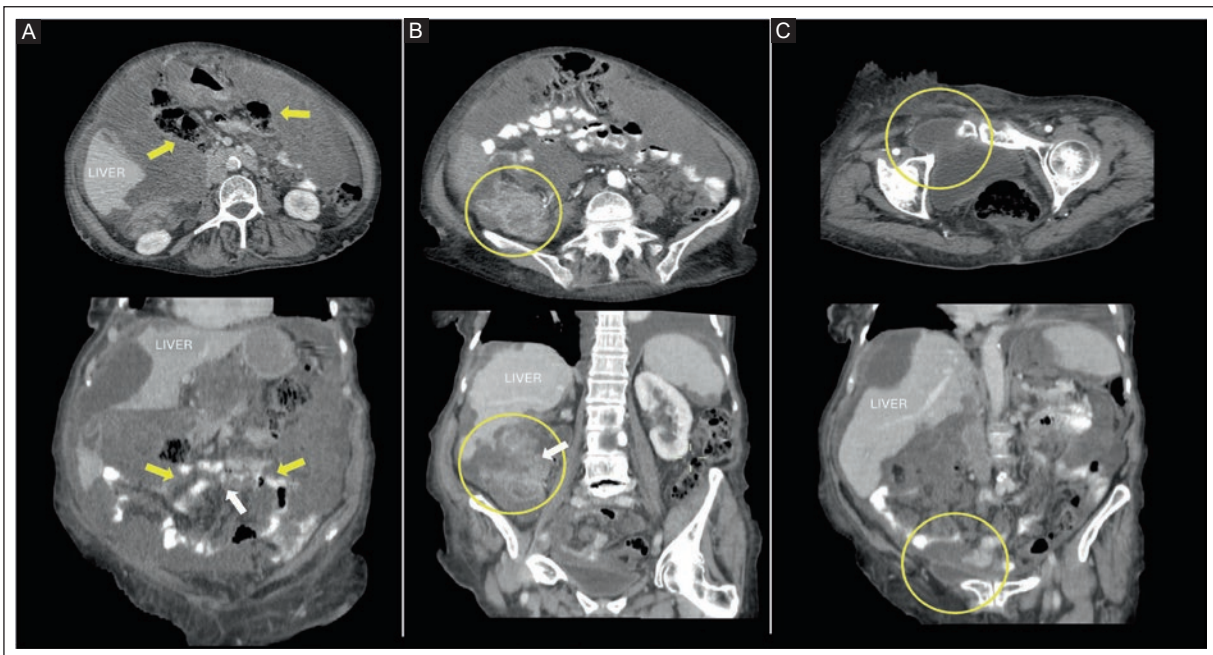


**Figure 3.** Abdominal CCT with oral mannitol contrast agent and intravenous iodine contrast in an 86-year-old woman with a diagnosis of PMP. **A:** the bowel loops were centralized and showed “omental caking” (yellow arrows). The mesentery shows increased density and decreased vascularity (white arrow). **B:** the cecum shows intense enhancement, an ill-defined mass (yellow circle), and a large notch on the antimesenteric surface (white arrow) in the arterial phase. **C:** the bladder was partially distended and compressed caudally and to the right, herniating towards the right inguinal canal, medial to the course of the epigastric artery (yellow circles).

CCT: contrast computed tomography; PMP: pseudomyxoma peritonei.



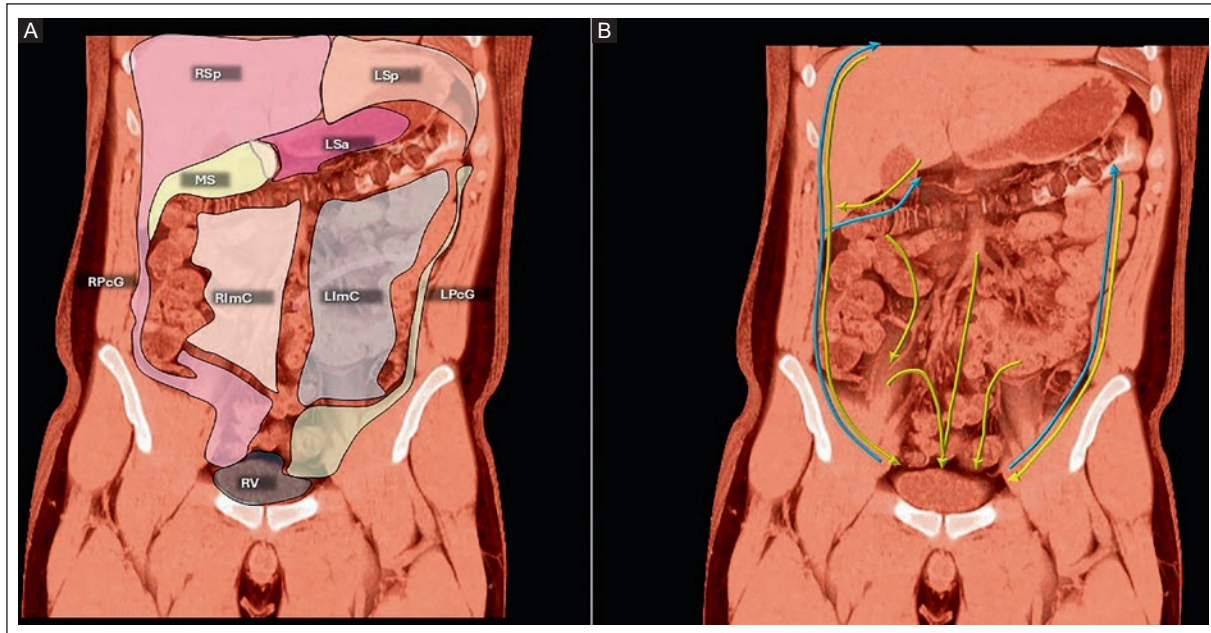


**Figure 4.** Coronal volumetric CCT reconstructions show recesses in the peritoneal cavity and fluid flow. **A:** the peritoneal cavity is a single, continuous space with interconnected recesses: right subphrenic (RSp), left subphrenic (LSp), Morrison space (MS), lesser sac (LSa), right paracolic gutter (RPcG), left paracolic gutter (LPcG), right inframesocolic (RImC), left inframesocolic (LImC), and retrovesical (RV). **B:** peritoneal spread occurs due to the circulation of peritoneal fluid, reaching various recesses in the abdomen and pelvis. Fluid is drawn into the upper abdomen due to low pressure below the diaphragm (blue arrows) and then flows into the pelvis by gravity (yellow arrows).

CCT: contrast computed tomography; PMP: pseudomyxoma peritonei.

adnexa were found. Based on the classic imaging findings on abdominal US and CCT, we diagnosed PMP.

### Clinical outcome

Cytochemical analysis of the abdominal fluid revealed mucinous material with scant epithelial cellularity. The patient's condition deteriorated rapidly, and she died three days after the abdominal CCT examination.

### DISCUSSION

This case of an 86-year-old woman with nonspecific abdominal symptoms and increased abdominal circumference displayed classic imaging findings of PMP on abdominal US and CCT scans. This report is intended for educational purposes and documents the typical imaging findings of PMP. We seek to improve our understanding of this rare neoplastic condition, emphasizing its imaging features on abdominal US and CCT.

US is typically the first imaging modality used in abdominal pathology. Our case showed indenting

masses on the anterior wall of the liver and US features for diagnosing PMP, such as the “onion skin” sign and a “starburst” appearance, together with the attachment of nodules to the abdominal wall and bowel loops. Echogenic ascites has a “starburst” appearance and immobile echogenic septations with a laminated appearance -the “onion skin” effect-. A highly echogenic ascitic fluid—characteristic of a viscous or gelatinous fluid—reflects concentric layering of mucin and suggests PMP<sup>2</sup>. Identifying these classic PMP findings on US may help the radiologist recommend further diagnostic studies.

CCT is a key imaging tool in the diagnosis of PMP. Although visceral scalloping is a characteristic feature of PMP, “omental caking” is a common finding on CCT and should not be overlooked. Our case has characteristic imaging findings of PMP: visceral scalloping, low-density nodules attached to the wall and visceral surfaces (“omental caking”), and low-density ascites collections in peritoneal recesses with a redistribution pattern. Our case was categorized as a large-volume disease based on the extent of ascites and CCT imaging findings. The

gold standard for the diagnosis of PMP is CCT<sup>2</sup>. However, in large-volume disease, CCT often becomes less specific, making primary tumor examination a challenge<sup>14</sup>. Gadolinium-enhanced magnetic resonance imaging (MRI) provides greater sensitivity for detecting primary appendiceal lesions and assessing the hepatoduodenal ligament and small bowel<sup>11</sup>. This case showed large-volume disease with extensive peritoneal involvement and characteristics of a cecal tumor that was compatible with peritoneal cytochemical fluid results for the diagnosis of PMP. Fonseca et al.<sup>12</sup> emphasize that radiologists should look for signs such as ascites and omental nodules. An accurate diagnosis of PMP is critical, so radiologists need to be familiar with CCT imaging findings and common locations.

The progression of PMP is characterized by the redistribution phenomenon, in which the mucinous tumor cells gather at specific sites and tend to accumulate under the influence of gravity and concentrate in sites where peritoneal fluid is absorbed (Figure 4). These sites include the greater and lesser omentum and the subphrenic spaces of the diaphragm, particularly on the right side<sup>9,11</sup>. The redistribution phenomenon of PMP can be recognized on a CCT scan, and the peritoneal and visceral involvement can be accurately delineated<sup>14</sup>. In our case report, we identified nodules and mucinous collections at specific sites. Knowledge of the normal peritoneal fluid flow also helped to identify the primary tumor location. Fonseca et al.<sup>12</sup> identified the subphrenic spaces and paracolic gutters as the most common sites for mucinous collections, while the liver, ovaries, and spleen were the most common sites for visceral involvement. Radiologists must be familiar with the peritoneal spaces, fluid flow, and absorption to effectively understand the redistribution phenomenon associated with PMP.

## CONCLUSION

We report an 86-year-old woman with nonspecific abdominal symptoms and an increase in abdominal circumference. Abdominal US and CCT showed typical PMP findings. Recognition of these imaging findings should guide the radiologist to diagnose PMP. Accurate diagnosis is paramount for appropriate therapeutic intervention.

## Acknowledgments

The authors thank Professor Ana M. Contreras-Navarro for her guidance in preparing and writing this scientific paper.

## Funding

This paper received no external funding.

## Conflicts of interest

The authors declare no conflicts of interest.

## Ethical disclosures

**Protection of human and animal subjects.** This paper complies with the Declaration of Helsinki (1964) and its amendments.

**Confidentiality data.** The authors declare they followed their center's protocol for sharing patient data.

**Right to privacy and informed consent.** Informed consent was not required to analyze and publish routinely acquired clinical and imaging data.

**Use of artificial intelligence.** The authors state that they did not use generative artificial intelligence to prepare this manuscript and/or create figures or figure legends.

## REFERENCES

- Han XD, Zhou N, Lu YY, Xu HB, Guo J, Liang L. Pseudomyxoma peritonei originating from intestinal duplication: A case report and review of the literature. *World J Clin Cases*. 2021;9(25):7459-7467. doi: 10.12998/wjcc.v9.i25.7459.
- Sarpietro G, Iraci Sareri M, Bonanno G, Matarazzo MG, Cianci, A. Incidental Diagnosis of Pseudomyxoma Peritonei: A Case Report. *Cureus*. 2022;14(3):e23425. doi:10.7759/cureus.23425.
- Smeenk RM, van Velthuisen ML, Verwaal VJ, Zoetmulder FA. Appendiceal neoplasms and pseudomyxoma peritonei: A population based study. *Eur J Surg Oncol*. 2008;34(2):196-201. doi: 10.1016/j.ejso.2007.04.002.
- Lin YL, Xu DZ, Li XB, Yan FC, Xu HB, Peng Z, et al. Consensus, and controversies on pseudomyxoma peritonei: a review of the published consensus statements and guidelines. *Orphanet J Rare Dis*. 2021;16(1):85. doi: 10.1186/s13023-021-01723-6.
- Kostov S, Kornovski Y, Slavchev S, Ivanova Y, Dzhankov D, Yordanov A. et al. Pseudomyxoma peritonei of appendiceal origin mimicking ovarian cancer - a case report with literature review. *Prz Menopauzalny*. 2021;20(3):148-153. doi: 10.5114/pm.2021.109120.
- Goldstein PJ, Cabanas J, da Silva RG, Sugarbaker PH. Pseudomyxoma peritonei arising from colonic polyps. *Eur J Surg Oncol*. 2006;32(7):764-766. doi: 10.1016/j.ejso.2006.04.009.
- Nayanar SK, Markose AJ, Avaronnan M, Dharmarajan A. Origin, and survival outcomes of Pseudomyxoma peritonei-A retrospective study. *J Cancer Res Ther*. 2024. doi: 10.4103/jcrt.jcrt\_191\_23.
- García KM, Flores KM, Ruiz A, González FL, Rodríguez ÁM. Pseudomyxoma Peritonei: Case Report and Literature Review. *J Gastrointest Cancer*. 2019;50(4):1037-1042. doi: 10.1007/s12029-018-00192-8.
- Sugarbaker PH. Pseudomyxoma peritonei. A cancer whose biology is characterized by a redistribution phenomenon. *Ann Surg*. 1994;219(2):109-111. doi: 10.1097/0000658-199402000-00001.
- Nguyen CGT, Hamid A, Chen A, Sood D, Jou J. Low grade appendiceal mucinous neoplasm metastatic to the ovary: A case report and intraoperative assessment guide. *Int J Surg Case Rep*. 2023;109:108563. doi: 10.1016/j.ijscr.2023.108563.
- Mittal R, Chandramohan A, Moran B. Pseudomyxoma peritonei: natural history and treatment. *Int J Hyperthermia*. 2017;33(5):511-519. doi: 10.1080/02656736.2017.1310938.
- Fonseca C, Carvalho S, Cunha TM, Gil RT, Abecasis N. The many faces of pseudomyxoma peritonei: a radiological review based on 30 cases. *Radiol Bras*. 2019;52(6):372-377. doi: 10.1590/0100-3984.2019.0044.
- Hanbidge AE, Lynch D, Wilson SR. US of the peritoneum. *Radiographics*. 2003;23(3):663-685. doi: 10.1148/rg.233025712.
- Sulkin TV, O'Neill H, Amin AI, Moran B. CT in pseudomyxoma peritonei: a review of 17 cases. *Clin Radiol*. 2002;57(7):608-613. doi: 10.1053/crad.2002.0942.

## MR imaging findings of neurosarcoidosis

Alejandro M. Bolon-Ojeda<sup>\*ID</sup>, Vania P. Balcazar-Vidal<sup>ID</sup>, and Jhonatan Gomez-Dominguez<sup>ID</sup>

Diagnostic and Therapeutic Imaging Department, Hospital Regional de Alta Especialidad "Dr. Juan Graham Casassus", Villahermosa, Tabasco, Mexico

A 28-year-old woman presented weight loss, fever, bilateral amaurosis, frontal headache, syncope lasting 2 minutes, incoherent speech, and prosopagnosia. She was a newly diagnosed HIV carrier with enlarged lymph nodes in the axillary region. Contrasted magnetic resonance imaging (MRI) showed a suprasellar lesion in the hypothalamus with irregular annular enhancement on T1 images without restricted diffusion (DWI and ADC) (Figure 1).

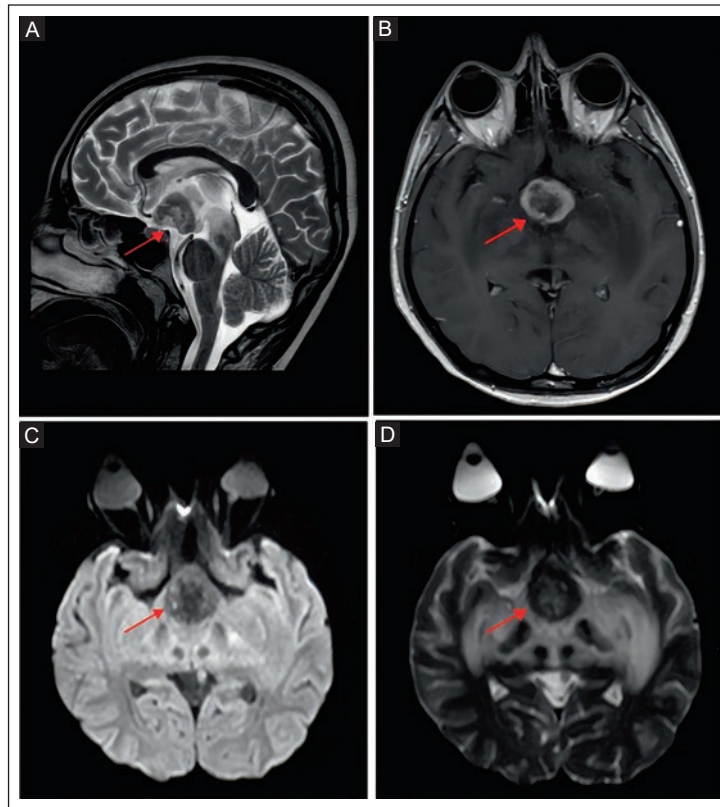


**Figure 1.** MRI of a 28-year-old woman with fever, bilateral amaurosis, and frontal headache. **A:** a sagittal T2-weighted view shows a heterogeneous and hypointense extra-axial suprasellar lesion in the hypothalamus with rounded morphology (red arrow). **B:** an axial T1-weighted post-gadolinium image with irregular annular enhancement (red arrow). **C and D:** axial DWI and ADC with no evidence of restriction (red arrows).

ADC: apparent diffusion coefficient; DWI: diffusion-weighted imaging; MRI: magnetic resonance imaging.

**\*Corresponding author:**

Alejandro M. Bolon-Ojeda  
E-mail: Alejandrobolon@hotmail.com

Received for publication: 27-03-2024  
Accepted for publication: 18-10-2024  
DOI: 10.24875/JMEXFRI.24000013

Available online: 20-12-2024  
J Mex Fed Radiol Imaging. 2024;3(4):280-281  
www.JMeXFRI.com

2696-8444 / © 2024 Federación Mexicana de Radiología e Imagen, A.C. Published by Permanyer. This is an open access article under the CC BY-NC-ND (<https://creativecommons.org/licenses/by-nc-nd/4.0/>).

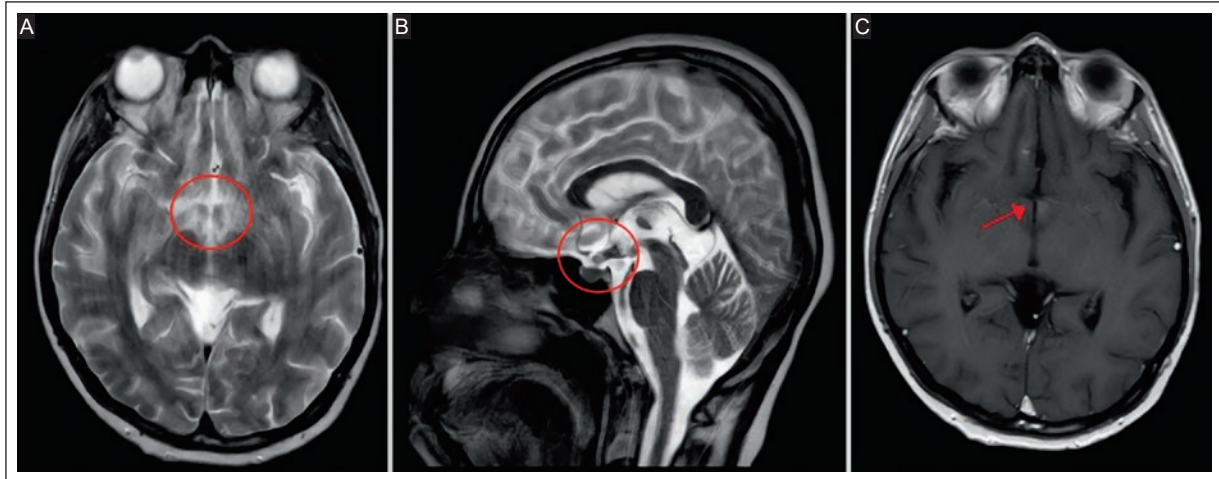


**Figure 2.** An MRI performed after steroid treatment of a 28-year-old woman with fever, bilateral amaurosis, and frontal headache showed clinical improvement. **A and B:** axial and sagittal T2-weighted images show almost complete regression of the lesion (red circles). **C:** axial T1-weighted post-gadolinium image shows discrete enhancement of the hypothalamus (red arrow).

MRI: magnetic resonance imaging.

An enlarged axillary lymph node was biopsied with a histologic diagnosis of sarcoidosis with nervous system involvement. She was treated with steroids for 18 days, and a follow-up MRI showed lesion regression but with discrete hypothalamic enhancement (Figure 2).

Sarcoidosis, an idiopathic systemic disease characterized by the formation of non-caseating granulomas, mainly affects the lungs and lymph nodes<sup>1</sup>. Nervous system involvement occurs in approximately 5%-15% of cases, and it is seen at autopsy in about 25% of cases<sup>2,3</sup>. Sarcoidosis can involve any part of the nervous system, including the cranial nerves, meninges, brain parenchyma, pituitary gland, spinal cord, and peripheral nerves<sup>1</sup>. The diagnosis of neurosarcoidosis can be delayed because of the wide spectrum of clinical findings<sup>4</sup>. Cranial neuropathy is the most common manifestation in 50%-70% of cases of neurosarcoidosis. MRI is the modality of choice for diagnosing neurosarcoidosis.

### Acknowledgments

The authors thank Professor Ana M. Contreras-Navarro for her guidance in preparing and writing this scientific paper.

### Funding

This paper received no external funding.

### Conflicts of interest

The authors declare no conflicts of interest.

### Ethical disclosures

**Protection of individuals.** This report complies with the Declaration of Helsinki (1964) and subsequent amendments.

**Data confidentiality.** The authors declare they followed their center's protocol for sharing patient data.

**Right to privacy and informed consent.** Informed consent was not required to analyze and publish routinely acquired clinical data.

**Use of artificial intelligence.** The authors did not use generative artificial intelligence in preparing this manuscript or creating figures or figure legends.

### REFERENCES

1. Smith JK, Matheus MG, Castillo M. Imaging manifestations of neurosarcoidosis. *AJR Am J Roentgenol.* 2004;182(2):289-295. doi: 10.2214/ajr.182.2.1820289.
2. Iannuzzi MC, Rybicki BA, Teirstein AS. Sarcoidosis. *N Engl J Med.* 2007;357(21):2153-2165. doi: 10.1056/NEJMra071714.
3. Terushkin V, Stern BJ, Judson MA, Hagiwara M, Pramanik B, Sanchez M, et al. Neurosarcoidosis: presentations and management. *Neurologist.* 2010;16(1):2-15. doi: 10.1097/NRL.0b013e3181c92a72. Erratum in: *Neurologist.* 2010;16(2):140.
4. Scott TF, Yandora K, Valeri A, Chieffe C, Schramke C. Aggressive therapy for neurosarcoidosis: long-term follow-up of 48 treated patients. *Arch Neurol.* 2007;64(5):691-696. doi: 10.1001/archneur.64. 5.691.